

MODEL-BASED REGISTRATION OF HISTOLOGICAL IMAGES

AS
36
2018
CMPTR
.H86

A thesis submitted to the faculty of
San Francisco State University
In partial fulfillment of
the requirements for
the Degree

Master of Science

In

Computer Science

by

Jeffrey Cy-Hao Hung

San Francisco, California

May 2018

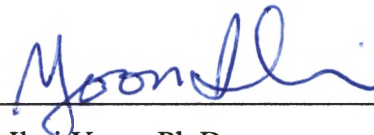
Copyright by
Jeffrey Cy-Hao Hung
2018

CERTIFICATION OF APPROVAL

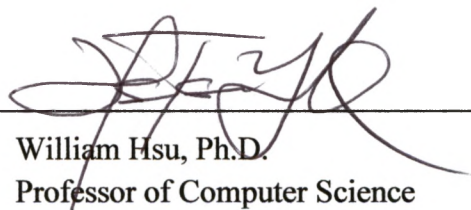
I certify that I have read Model-Based Registration of Histological Images by Jeffrey Cy-Hao Hung, and that in my opinion this work meets the criteria for approving a thesis submitted in partial fulfillment of the requirement for the degree Master of Science in Computer Science: General at San Francisco State University.



Kaz Okada, Ph.D.
Associate Professor of Computer Science



Ilmi Yoon, Ph.D.
Professor of Computer Science



William Hsu, Ph.D.
Professor of Computer Science

MODEL-BASED REGISTRATION OF HISTOLOGICAL IMAGES

Jeffrey Cy-Hao Hung
San Francisco, California
2018

Anti-cancer drug development requires an understanding of the mechanism of action (MOA). Histological analysis of images taken from xenografts enable characterization of how the tissue reacts to different compounds. Immunohistochemical (IHC) stains highlight a specific aspect of the tissue. Registering a two-dimensional (2D) IHC image with its corresponding 2D cellular morphology image facilitates the study of complex immunological behavior. This thesis describes the design and implementation of a multi-stage process to register histological images. The method utilizes a Procrustean, an affine and a least-squares support vector regression (LS-SVR) transformation to register automatically segmented regions of interest. Performance was compared to a method that replaces the LS-SVR with a second order polynomial transform.

I certify that the Abstract is a correct representation of the content of this thesis.



Chair, Thesis Committee

May 2, 2018

Date

PREFACE AND/OR ACKNOWLEDGEMENTS

Firstly, I would like to thank Professor Kaz Okada for his invaluable guidance and patience throughout this long journey. His guidance taught me how research is conducted in academia and how it is chronicled in journals.

My sincere thanks also goes to Jeff Eastham-Anderson and Genentech, Inc., who provided me an opportunity to join their team as intern and provided access to the resources that made this research possible.

Last but not least, I am grateful for the support of my wife and children, who no longer need to ask why Daddy is hiding in the office again.

TABLE OF CONTENTS

1	INTRODUCTION	1
1.1	Optical Artifacts	2
1.2	Physical Artifacts	5
1.3	Proposed Method and Its Motivation	7
1.4	Summary of Contributions.....	8
1.5	Thesis Structure.....	11
2	RELATED THEORIES & METHODS.....	12
2.1	Landmark-Based vs. Voxel Property-Based Registration	13
2.2	Global Rigid vs. Local Non-Rigid Registration.....	14
2.3	Machine Learning as an Alternative Transformation Method	15
3	DATA SET.....	21
3.1	Tissue Staining.....	21
3.2	Creating Sub-Images	23
3.3	Masking Sub-Images	24
3.4	Perimeter Control Points.....	25
3.5	Interior Control Points	26
4	PROPOSED METHOD	28
4.1	Concept.....	28
4.2	Image Registration Process Flow	28
4.3	Metrics	31
4.4	Implementation	41
5	EXPERIMENTS.....	46
5.1	Expt 1: Align Entire Image with Perimeter Control Points	46
5.2	Expt 2: Align Masked Image with Perimeter Control Points.....	52
5.3	Expt 3: Align Masked Image with Perimeter and 10 ICP's.....	59
5.4	Expt 4: Evaluate 60x60 Pixel Window Around 10 ICP's.....	64
5.5	Expt 5: Evaluate 60x60 Pixel Window Around 5/10/15 ICP's.....	69
5.6	Expt 6: Evaluate 60x60/120x120/180x180 Pixel Windows Around 5/10/15 ICP's ...	76
6	CONCLUSION	107
6.1	Summary of Results	107
6.2	Future Work.....	107

TABLE OF CONTENTS

7	REFERENCE LIST	110
8	APPENDIX	115
8.1	Process Flow to Create Image.....	115
8.2	Whole Image Identification Numbers	115
8.3	Sub-Image Identification Numbers	117
8.4	Sub-Image Masking Algorithm.....	118
8.5	Tissue Segmentation Algorithm.....	119

LIST OF TABLES

Table	Page
1. Description of the antigen targets utilized in this study.....	22
2. Expt 1 results - sum of distance for PCP's	48
3. Expt 1 results - MI over entire image.....	49
4. Expt 2 Results with outlier - sum of distances for PCP's	53
5. Expt 2 Results with outlier - MI over masked image	53
6. Expt 2 Results without outlier - sum of distances for PCP's	55
7. Expt 2 Results without outlier - MI over masked image	57
8. Expt 3 Results – sum of distances for PCP's + 10 ICP's	60
9. Expt 3 Results - MI over masked image for PCP's + 10 ICP's	62
10. Expt 4 Results - MI in 60x60 windows around 10 ICP's	65
11. Expt 5 Results - sum of distances for PCP's + varying ICP's	70
12. Expt 5 Results - MI over masked image for PCP's + varying ICP's.....	71
13. Expt 5 Results - MI in 60x60 windows around varying ICP's	73
14. Expt 6 Results - sum of distances for PCP's + 5 ICP's	78
15. Expt 6 Results - sum of distances for PCP's + 10 ICP's.....	79
16. Expt 6 Results - sum of distances for PCP's + 15 ICP's	80
17. Expt 6 Results - MI over masked image for PCP's + 5 ICP's	82
18. Expt 6 Results - MI over masked image for PCP's + 10 ICP's.....	83
19. Expt 6 Results - MI over masked image for PCP's + 15 ICP's.....	84
20. Expt 6 Results - MI in varying windows around 5 ICP's.....	85
21. Expt 6 Results - MI in varying windows around 10 ICP's.....	86
22. Expt 6 Results - MI in varying windows around 10 ICP's	87
23. Expt 6 Results - SD for PCP's + varying ICP's (60x60 window)	92
24. Expt 6 Results - SD for PCP's + varying ICP's (120x120 window)	93
25. Expt 6 Results - SD for PCP's + varying ICP's (180x180 window)	94

LIST OF TABLES

Table	Page
26. Expt 6 Results - MI in varying windows around 10 ICP's	87
27. Expt 6 Results - SD for PCP's + varying ICP's (60x60 window)	92
28. Expt 6 Results - SD for PCP's + varying ICP's (120x120 window)	93
29. Expt 6 Results - SD for PCP's + varying ICP's (180x180 window)	94
30. Expt 6 Results - MI over masked image for PCP's + ICP's (60x60)	95
31. Expt 6 Results - MI over masked image for PCP's + ICP's (120x120)	96
32. Expt 6 Results - MI over masked image for PCP's + ICP's (180x180)	97
33. Expt 6 Results - MI in 60x60 windows around varying ICP's	98
34. Expt 6 Results - MI in 120x120 windows around varying ICP's	99
35. Expt 6 Results - MI in 180x180 windows around varying ICP's	100
36. Slide identification numbers for each image in the MJ_MECA_* series	116
37. Number of sub-images per image pair	117

LIST OF FIGURES

Figure	Page
1. Optical artifact – variation in background illumination.....	2
2. Optical artifact – correction of background intensity.....	3
3. Optical artifact – intensity variations caused by staining variations.....	4
4. Stain dependent color variations	4
5. Tissue embedded in paraffin prior to slicing.....	5
6. Examples of tissue deformation	6
7. Optical artifact – tissue folds, air bubbles	6
8. Image registration process flow at start of study	8
9. Classification of registration methods.....	12
10. Comparison of global vs local domain for different transformations	14
11. Soft margin loss for linear SVR.....	16
12. Alternative kernels for SVR	18
13. Dual antibody process for marking antigen locations with DAB	21
14. Feature appearance varies with different antigen targets	23
15. Cropping image to form sub-image	24
16. Masking sub-image to keep largest piece of tissue.....	25
17. External control points located by Harris corner detector.....	26
18. Interior control points uniformly distributed across tissue area.....	28
19. Image registration process flow at completion of study.....	31
20. Calculate Euclidean distance between two points	33
21. Example of how Euclidean distance changes with alignment.....	33
22. Mutual information as a function of the marginal and conditional entropies.....	35
23. Orientation of background affects mutual information.....	36
24. Cropping a window centered on an ICP	38
25. Window tissue changes appearance during registration process	39

LIST OF FIGURES

Figure	Page
26. Workflow to generate a LS-SVR model	43
27. Expt 1 results - sum of distances for PCP's.....	48
28. Expt 1 results - MI over entire image.....	50
29. Expt 2 results with outlier - MI over masked image.....	55
30. Poor LS-SVR registration due to uneven distribution of PCP's.....	55
31. Expt 2 results without outlier - sum of distances PCP's	56
32. Expt 2 results without outlier - MI over masked image.....	57
33. Expt 3 Results - sum of distances for PCP's + 10 ICP's.....	61
34. Expt 3 Results - MI over masked image for PCP's + 10 ICP's.....	62
35. Expt 4 Results – MI in 60x60 windows around 10 ICP's	65
36. Expt 4 Results - MI difference in 60x60 windows around 10 ICP's	66
37. Registration change assuming the LS-SVR transform has a limited radius.....	68
38. Expt 5 Results - sum of distances for PCP's + varying ICP's.....	70
39. Expt 5 Results - MI over masked image for PCP's + varying ICP's.....	72
40. Expt 5 Results - MI in 60x60 windows around varying ICP's.....	73
41. Expt 5 Results – MI difference in 60x60 windows around varying ICP's.....	74
42. LS-SVR window MI improves with increasing number of ICP's.....	76
43. Expt 6 Results - sum of distances for PCP's + 5 ICP's.....	78
44. Expt 6 Results - sum of distances for PCP's + 10 ICP's.....	79
45. Expt 6 Results - sum of distances for PCP's + 15 ICP's.....	80
46. Expt 6 Results - MI over masked image for PCP's + 5 ICP's.....	82
47. Expt 6 Results - MI over masked image for PCP's + 10 ICP's.....	83
48. Expt 6 Results - MI over masked image for PCP's + 15 ICP's.....	84
49. Expt 6 Results - MI in varying windows around 5 ICP's.....	85

LIST OF FIGURES

Figure	Page
50. Expt 6 Results - MI in varying windows around 10 ICP's.....	86
51. Expt 6 Results - MI in varying windows around 15 ICP's.....	87
52. Expt 6 Results - MI difference in varying windows around 5 ICP's.....	88
53. Expt 6 Results - MI difference in varying windows around 10 ICP's.....	89
54. Expt 6 Results - MI difference in varying windows around 15 ICP's.....	90
55. Expt 6 Results - SD for PCP's + varying ICP's (60x60 win).....	92
56. Expt 6 Results - SD for PCP's + varying ICP's (120x120 win).....	93
57. Expt 6 Results - SD for PCP's + varying ICP's (180x180 win).....	94
58. Expt 6 Results - MI over masked image for PCP's + ICP's (60x60 win).....	95
59. Expt 6 Results - MI over masked image for PCP's + ICP's (120x120 win).....	96
60. Expt 6 Results - MI over masked image for PCP's + ICP's (180x180 win).....	97
61. Expt 6 Results - MI in 60x60 windows around varying ICP's.....	98
62. Expt 6 Results - MI in 120x120 windows around varying ICP's.....	99
63. Expt 6 Results - MI in 180x180 windows around varying ICP's.....	100
64. Expt 6 Results - MI difference in 60x60 windows for varying ICP's.....	101
65. Expt 6 Results - MI difference in 120x120 windows for varying ICP's.....	102
66. Expt 6 Results - MI difference in 180x180 windows for varying ICP's.....	103
67. Mechanism for change in window MI as function of window size.....	105
68. Mechanism for change in window MI as function of number of ICP's.....	106

LIST OF APPENDICES

Appendix	Page
8.1 Process Flow to Create Image	115
8.2 Whole Image Identification Numbers	115
8.3 Sub-Image Identification Numbers	117
8.4 Sub-Image Masking Algorithm	118
8.5 Tissue Segmentation Algorithm	119

1 INTRODUCTION

Medical imaging plays a prominent role in the planning, execution and evaluation of surgical and therapeutic procedures.[21] Imaging modalities can be divided into anatomical modes that depict morphology and functional modes that depict metabolism of anatomical features. The integration of information from two different modes often provides additional clinical insight. Clearly the first step in the integration process is the spatial alignment of images of different modalities, which is referred to as registration.

Anatomical modalities are often in-vivo 3-D imaging methods such as magnetic resonance imaging (MRI) and computed tomography (CT).[14] The typical resolution of a MRI is 1 mm per voxel. For a functional modality, one option is an ex-vivo 2-D histological section examined with optical microscopy. The typical resolution of such an optical image is 10 μm per pixel.

This study focuses on registering histological images forming contiguous sections in the context of pathological studies for pharmaceutical research. In the area of cancer research, the histological analysis of xenografts implanted into test animals enables the characterization of how the tumor reacts to different treatments during the drug development process. The concept of different “modes” arises from the application of a different immunohistochemical (IHC) stain on each image. Each type of stain highlights a specific aspect of the tissue. Registering a 2-D IHC image with its corresponding cellular morphology image facilitates the study of complex immunological behavior.[13][32]

Registration of the optical images of tissue sections, however, presents a number of difficulties that are not present in other imaging modalities. The presence of artifacts in these images causes the image quality to vary, making it troublesome to compare a pair of images. Any registration process requires the correction of these artifacts, or the accuracy of the registration would suffer immensely.

1.1 Optical Artifacts

One artifact of optical microscopy is the shading caused by background illumination, which creates intensity variations not present in the original histological section.[1] Sections mounted close to the edge of the glass slide can exhibit luminance gradients like the one seen in Figure 1.[25]



Figure 1: An example of an optical artifact affecting histological images is the variation in background illumination. [25]

Another example of a background shading effect is shown in Figure 2(a). In this case, the narrow cone of light in the microscope causes the variation. Correction of this

artifact requires applying filter algorithms to the image. Figure 2(b) shows the image after the removal of the artifact. Notice that the gray scale intensities of the tissue in the corrected image have also changed as a result of this process. This unintended side-effect may be considered the introduction of a different illumination artifact.

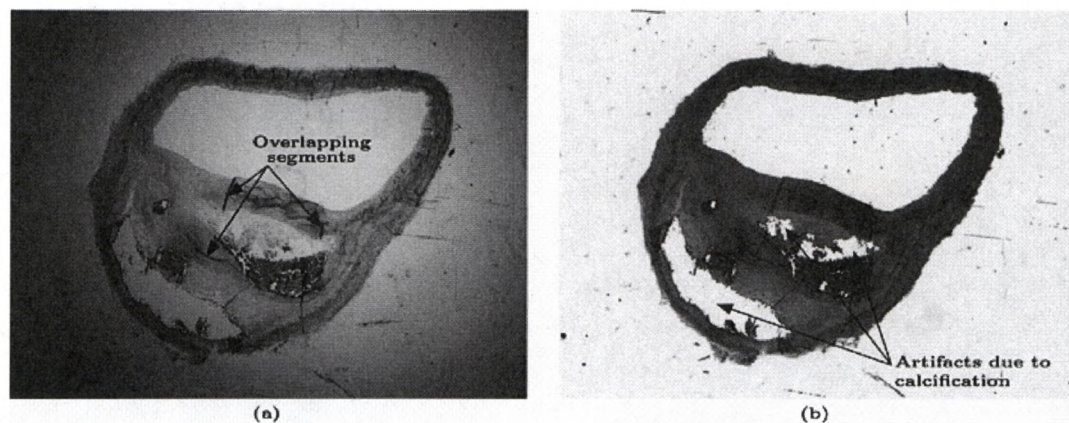


Figure 2: Correction of optical artifact: (a) raw image showing background intensity variation due to narrow cone of light. (b) processed image showing corrected background intensity. [1]

Strength of staining varies depending on differences like section thickness and staining duration. Such stain variabilities often result in color and intensity fluctuations in the specimen images.[25] Two consecutive tissue samples are shown in Figure 3(a) and Figure 3(b). The staining variation results in a large difference in intensity between the two images. Feature-based registration methods must recognize tissue boundaries even when these staining variations are present. Intensity-based registration methods must resolve tissue similarity between varying intensity values. One commonly used technique scales the specific image intensity histogram to a standard intensity histogram to avoid large registration errors.[2]

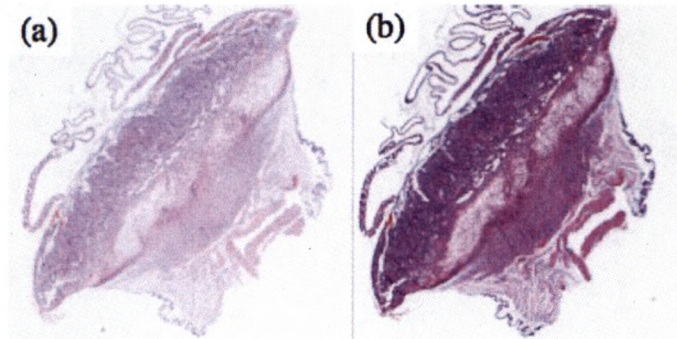


Figure 3: An optical artifact in which staining variations create intensity variations. [25]

Matching specific regions of interest across images is also challenging when comparing images with different stains. The DAB (3,3'-diaminobenzidine) stain with the hematoxylin counterstain in Figure 4(a) appears as brown on a blue background. In contrast, the hematoxylin and eosin stain in Figure 4(b) appears as purple with pink. Registration algorithms must account for color differences. For more details about the staining process, refer to Section 3.1.

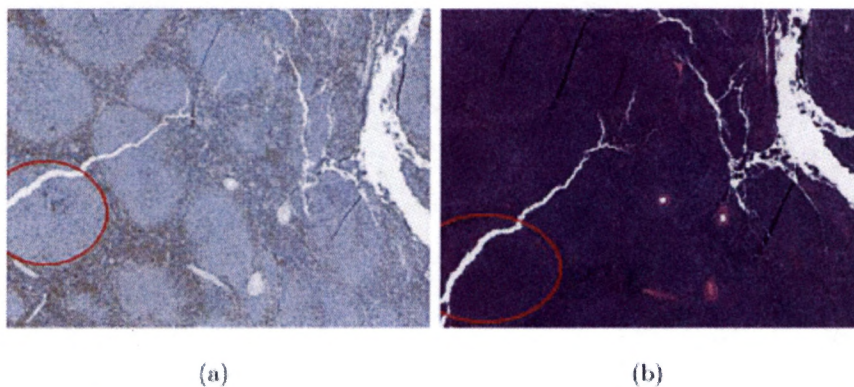


Figure 4: The region of interest outlined in red shows the color difference between (a) a DAB (3,3'-diaminobenzidine) stain with a hematoxylin counterstain and (b) a hematoxylin and eosin stain.[6]

1.2 Physical Artifacts

The preparation of histological sections is the source of many physical artifacts. A tissue sample is first embedded in paraffin as shown in Figure 5.[29] This block of tissue is sliced with a microtome into sections of constant thickness on the order of 5 μm . The thin slice is placed on a glass slide and stained. Finally, the sample is capped with a glass slide cover.



Figure 5: Tissue embedded in paraffin prior to slicing.[4]

A key challenge during registration is to compensate for distortion introduced by the above-described slide preparation.[6] There are discernible deformations between consecutive tissue sections, including bending, shearing, stretching and warping as seen in Figure 6. In some cases, the deformations globally affect the entire image. Regional distortions such as stretching and compacting mostly take place in the vertical (i.e., slicing) direction.[14] In other cases, varying mechanical properties at different tumor

sites cause localized deformations.[13] At micron resolutions, even minor deformations become conspicuous and affect accuracy.

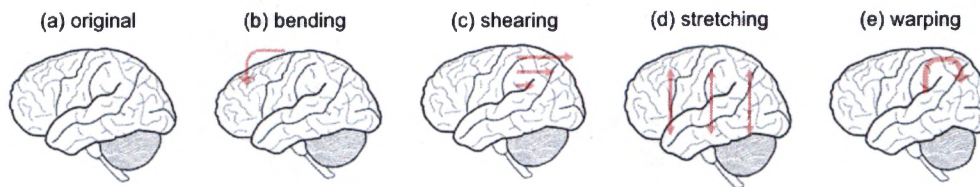


Figure 6: Examples of tissue deformation: (a) original image, (b) bending of frontal lobe on left, (c) shearing of upper half toward right, (d) stretching in vertical axis, (e) warping around occipital lobe on right.

Gross defects are also an occasional by-product of the slide preparation process. During slicing, the edges of the sections can be torn or discarded entirely.[29][2] During mounting on the glass slide, the extremely thin tissue can be folded as shown in Figure 7.[25] The final placement of the slide cover potentially traps dust that shows up as dark specks in the background.[14] Air bubbles can also be trapped, creating an out-of-focus artifact outlined in black.[34]

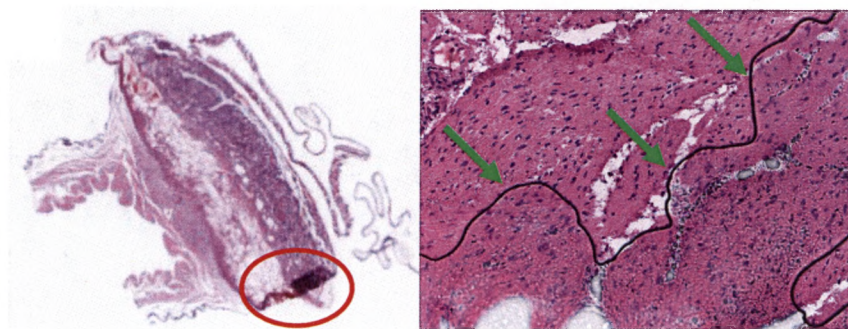


Figure 7: Examples of optical artifacts: (left) folded tissue circled in red[25], (right) green arrows point to air bubble outlined in black[34].

A registration method must be capable of discerning between a physical artifact and the inherent anatomical variance between adjacent tissue sections.[14] Despite their similarity, two successive slices cannot be anatomically equivalent, because there are differences in the number of cells and their shapes. Severe morphological differences may be observed if the gap between slices is large.[29] This suggests that the registration method should emphasize the largest physiological structures, which remain unaltered between two consecutive sections.[32] The smaller morphological differences are not artifacts and should not be corrected.

1.3 Proposed Method and Its Motivation

The origin for this study can be traced back to my internship at Genentech, Inc. My supervisor, Jeffrey Eastham-Anderson, provided Matlab code that implemented a single affine transformation as part of the process flow shown in Figure 8. I was asked to improve the performance and robustness of the registration algorithm. The resulting code at the end of the project incorporated a series of higher order polynomial transforms in stage 3 to perform non-linear registration at a fine level.

The higher order polynomial transforms tended to be unstable leading to gross mis-registration for some images. Rules were added to ignore the stage 3 transform if a gross error occurred. While this method solved the robustness issues, it resulted in a subset of images that do not receive fine registration. An alternative to polynomial transforms was necessary to perform non-linear registration.

This thesis presents a method for performing non-linear registration of histological images that is based on a machine learning technique, least-squares support vector regression.

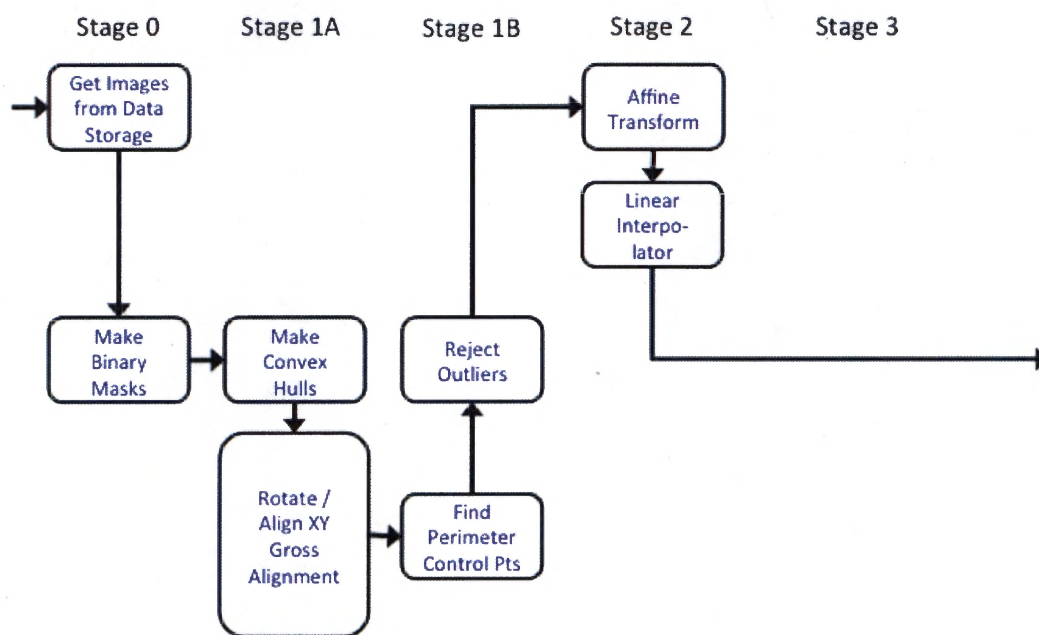


Figure 8: Image registration process flow for the code provided by Genentech at the start of my internship. A description of the stages is provided in Section 4.1.

1.4 Summary of Contributions

A number of methods for global and local warping have previously been proposed for registering a pair of two dimensional (2D) histological images. In contrast, a majority of the literature for machine learning warping methods was applied to the registration of a three-dimensional (3D) medical image to a two-dimensional medical image. My first contribution was the design of a registration workflow that made use of a machine

learning algorithm discovered during my literature study. I adapted a least-squares support vector regression (LS-SVR) warping method to the registration of a pair of 2D histological images. I incorporated this method by extending the polynomial-based algorithm that I developed during my internship project.

My second contribution was the implementation of the machine learning based registration algorithm. The implementation began with the substitution of the Procrustian algorithm for gross alignment. Local non-linear registration was added in the form of LS-SVR. Global non-linear registration remained in the form of a second order polynomial transform. I also implemented sum of distance and mutual information metrics after each stage to quantify the improvement in registration.

My third contribution was the systematic validation of the LS-SVR's merit through a series of experiments. I created ground-truth sets of control points by manually matching the features in each pair of images in the dataset. I applied the algorithm to the dataset to evaluate the following hypotheses:

[Hypothesis 1] A local non-linear transform, such as the LS-SVR transform, registers histological images better than a global non-linear transform, such as the second-order polynomial transform.

[Result 1] The LS-SVR model was better at registering the automatically generated perimeter control points, but worse at registering the entire image.

[Hypothesis 2] The pixels outside of the tissue area negatively affect the registration metric for the entire image.

[Result 2] The outside pixels negatively impact the metrics for the LS-SVR model. Masking the outside pixels improved the LS-SVR performance, but it remained worse than the polynomial model at registering the entire image.

[Hypothesis 3] The addition of interior control points (ICP's) improves the performance of the LS-SVR model.

[Result 3] The addition of ICP's helped the LS-SVR model register the entire image better than the polynomial model, but the result was not statistically significant at all thresholds.

[Hypothesis 4] The LS-SVR model performs better than the polynomial model in the neighborhood of the ICP's.

[Result 4] The LS-SVR model registers the neighborhood pixels better than the polynomial model at a statistically significant level.

[Hypothesis 5] Increasing the number of ICP's improves the performance of the LS-SVR model in the neighborhood of each ICP.

[Result 5] Some minimum number of ICP's may be required to reach optimal local performance, but adding control points beyond that number is not beneficial.

[Hypothesis 6] Increasing the number of ICPs improves the performance of the LS-SVR model in a wider neighborhood around each ICP.

[Result 6] Increasing the number of ICP's improves performance farther away from the control points, but the effect is small.

1.5 Thesis Structure

The rest of the paper is organized in the following manner. Section II briefly reviews some related methods. Section III describes the dataset provided by Genentech, Inc. Section IV details the implementation of the proposed method. Section V tabulates and evaluates the experimental results. Finally, section VI summarizes our current work and proposes some avenues for future work.

2 RELATED THEORIES & METHODS

Medical registration is an extensive field of research. A vast number of registration methods have been developed over the years. Efforts have been made to group the methods by their characteristics. The red boxes in Figure 9 describe the characteristics of the proposed method. This chapter provides some background on these relevant characteristics. For more extensive description of other aspects of registration methods, the reader is directed to literature surveys conducted by Maintz & Viergever [21], Zitova et al. [44], Sotiras et al. [40], Oliveira & Tavares [28], and Mani & Arivazhagan [22].

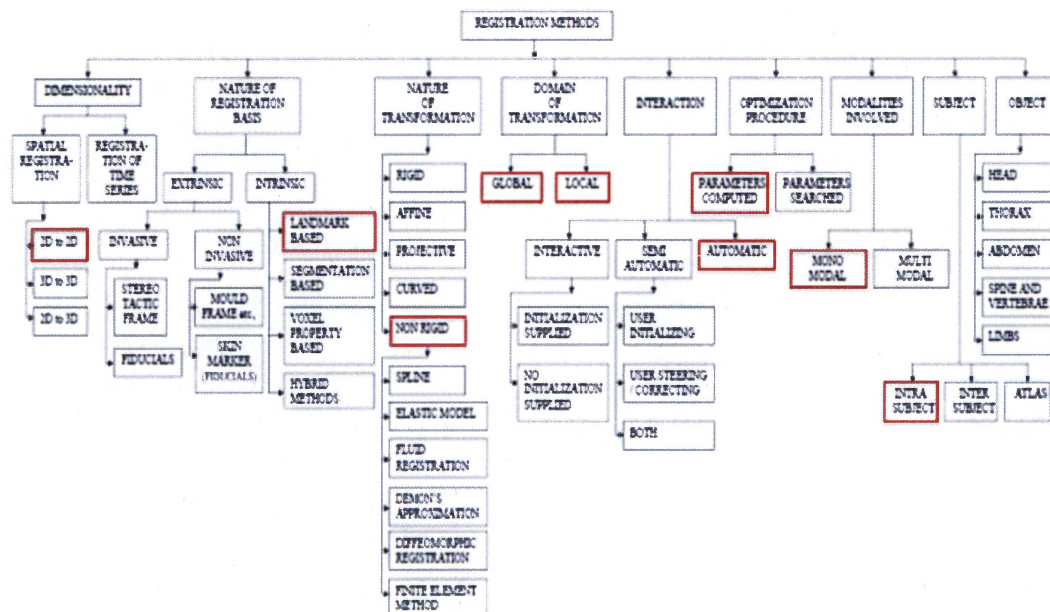


Figure 9: Tree diagram by Mani and Arivazhagan [22] that summarizes the classification scheme for medical registration methods introduced by vanden Elsen, Pol and Viergever [43].

2.1 Landmark-Based vs. Voxel Property-Based Registration

Landmark-based (or feature-based) registration methods identify salient features such as surfaces, curves and points that can be matched in the two images to be aligned.[21] These features are typically related to the anatomical morphology of the tissue, and they can be generated automatically or identified manually. The features are distributed sparsely across the images. The correspondence between the two sets of matched features defines the transformation that aligns one image to the other. The remainder of the image is aligned by interpolating between transformed features to infer the new pixel positions.

Voxel property-based (or intensity-based) registration methods do not reduce the gray-level image, but attempts to use all of the available information throughout the registration process.[21] These methods require defining a measure of intensity similarity between the two images and iteratively transforms an image until the similarity measure is maximized. The image intensities are assumed to be most alike at the optimum registration.

Landmark-based methods are much faster, since the number of landmarks utilized in calculating a transformation function is typically limited. These methods also avoid getting trapped in local minima, because the optimization path is clear. The drawback with these methods is the complexity of detecting and matching landmarks. User interaction is often required to identify landmarks. In contrast, intensity-based methods are computationally expensive, because every pixel in the image must be processed to

calculate a transform function. However, these methods benefit by no longer requiring user intervention to reduce the data prior to the registration process.

2.2 Global Rigid vs. Local Non-Rigid Registration

A transformation has a global domain if it applies to the entire image. When only translations and rotations of the image are allowed, the transformation is also labeled rigid. The global rigid transformation is often used for registering medical images, when the assumption of an incompressible body part is a good approximation. An example of the global rigid transformation is shown in Figure 10.

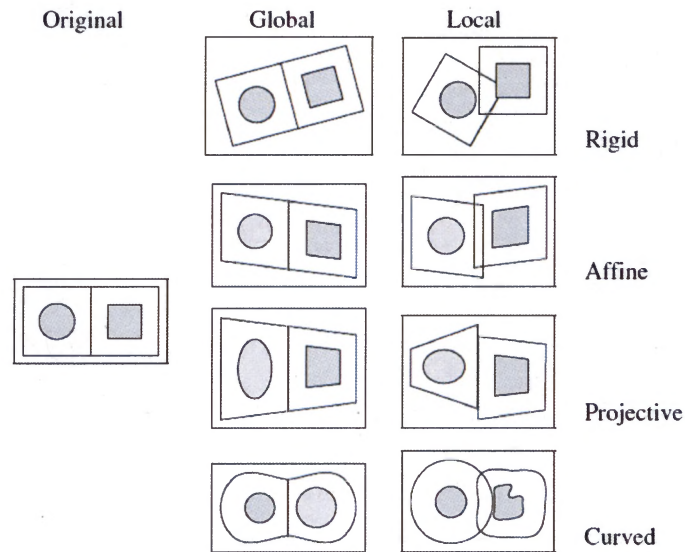


Figure 10: Comparison of global vs. local domain for different transformations.[21]

A transformation has a local domain if each subsection of an image has its own transformation. When deformation of the image takes place, the transformation is also labeled non-rigid. The local curved transformation shown in Figure 10 demonstrates this

deformation. The local non-rigid transformation is necessary for registering histological images. The tissue is compressed differently during sample preparation, violating the rigid body assumption. Moreover, small scale features may change shape or disappear from image to image.

Most local registration transformations are non-linear to allow better fitting of small scale features in an image. This non-linearity makes the transform prone to converge on an incorrect solution when the images are greatly misaligned. One solution to this issue is to add constraints that put a limit on the amount of transformation that can take place. These regularization parameters must be built into the transformation function. Another solution utilizes a multi-stage process that applies rigid or affine transformations to the image prior to applying the local non-rigid transformation. The preprocessing effectively constrains the amount of misalignment that must be transformed by the function.

2.3 Machine Learning as an Alternative Transformation Method

An alternative approach is to apply machine learning techniques to the registration problem. The use of evolutionary algorithms to register 2D and 3D medical images began in 1984.[38] A self-organizing map (SOM) is a form of neural network that was applied to medical registration in the mid-2000's.[12] Different forms of regression have also been applied to the registration of 2D to 3D medical images.[11]

2.3.1 Support Vector Regression

Support vector regression (SVR) was applied to register 3D computed tomography (CT) and 3D positron emission tomography (PET) scans to 3D magnetic resonance (MR) scans.[46] Since the scans were brain images, the authors chose a global rigid body transformation to minimize a mutual information (MI) metric. In another case, SVR was applied to register 3D MR brain scans taken pre-operatively with 2D x-ray images taken intra-operatively.[36] The authors also chose a global rigid body transformation to minimize a mutual information (MI) metric.

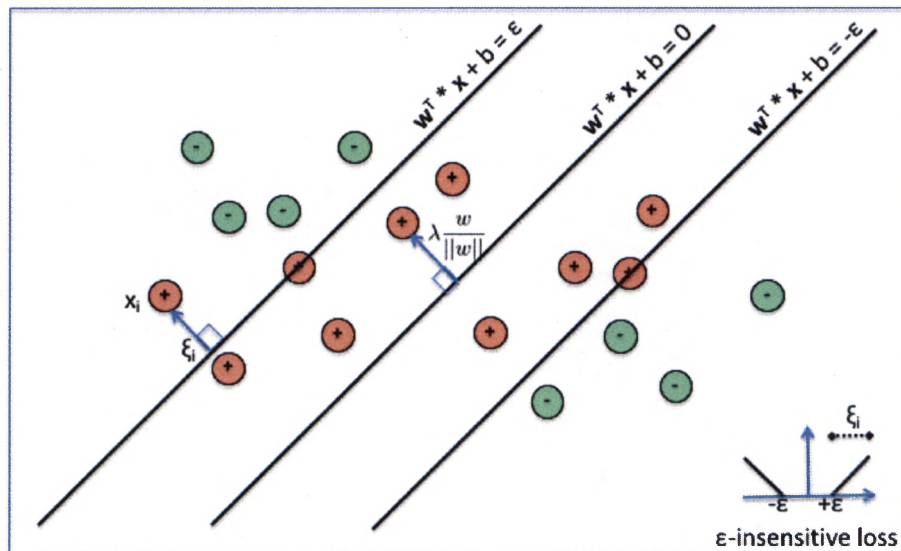


Figure 11: Soft margin loss for linear SVR. Center line is the hyperplane, while the left and right lines are the upper and lower boundaries in which there is no loss. Red circles outside the boundaries incur a loss.

SVR works by finding a function $f(x)$ that maps all of the data points x_i in such a way that the difference between the hyperplane $f(x)$ and the actual targets y_i does not exceed ϵ ,

as shown in Figure 11. Any difference less than ε is ignored, while any difference greater than ε is captured by an error variable, ξ_i . This error variable is defined as the distance from the solution boundary if the point is misclassified and zero if classified correctly. The constant $C > 0$ determines the trade-off between the flatness of hyperplane $f(x)$ and the amount that deviations larger than ε are tolerated. A smaller value of C translates into tolerance for a larger deviation.[39]

The primal formulation of the SVR minimizes the quadratic objective function,

$$\frac{1}{2} \sum_{i=1}^n \omega_i^2 + C \sum_{i=1}^n (\xi_i + \xi_i^*) \quad (1)$$

subject to the constraints

$$y_i - (\boldsymbol{\omega} \cdot \mathbf{x}_i + b) \leq \varepsilon + \xi_i \quad (2)$$

$$(\boldsymbol{\omega} \cdot \mathbf{x}_i + b) - y_i \leq \varepsilon + \xi_i^* \quad (3)$$

$$\xi_i, \xi_i^* \geq 0 \quad (4)$$

Defining a Lagrangian function, the dual formulation of the SVR minimizes the quadratic objective function in equation (1).

$$\Lambda_D(\boldsymbol{\alpha}, \boldsymbol{\alpha}^*) = -\frac{1}{2} \sum_{i,j=1}^N (\alpha_i - \alpha_i^*)(\alpha_j - \alpha_j^*) \mathbf{x}_i \cdot \mathbf{x}_j - \varepsilon \sum_{i=1}^N (\alpha_i + \alpha_i^*) + \sum_{i=1}^N y_i (\alpha_i - \alpha_i^*) \quad (5)$$

subject to the constraints

$$\alpha_j, \alpha_j^* \in [0, C] \quad (6)$$

$$\sum_{j=1}^N (\alpha_j - \alpha_j^*) = 0 \quad (7)$$

Substituting in the partial derivatives for the Lagrangian function leads to the support vector expansion:

$$f(\mathbf{x}) = \sum_{i,j=1}^N (\alpha_i - \alpha_i^*)(\alpha_j - \alpha_j^*) \mathbf{x}_i \cdot \mathbf{x}_j + b \quad (8)$$

The support vector expansion can be further modified using the “kernel trick”. The dot product term in equation (8) can be replaced by the dot product of more complex non-linear functions.

$$f(\mathbf{x}) = \sum_{i,j=1}^N (\alpha_i - \alpha_i^*)(\alpha_j - \alpha_j^*) \Phi(\mathbf{x}_i) \cdot \Phi(\mathbf{x}_j) + b \quad (9)$$

Some examples of these kernel functions are listed in Figure 12. This study makes use of the Gaussian kernel, which is also referred to as the radial basis function.

Kernel

Linear	$\Phi(\mathbf{x}_i) \cdot \Phi(\mathbf{x}_j) = \mathbf{x}_i \cdot \mathbf{x}_j$
Exponential	$\Phi(\mathbf{x}_i) \cdot \Phi(\mathbf{x}_j) = \exp(-\gamma \ \mathbf{x}_i - \mathbf{x}_j\)$
Gaussian	$\Phi(\mathbf{x}_i) \cdot \Phi(\mathbf{x}_j) = \exp(-\gamma \ \mathbf{x}_i - \mathbf{x}_j\ ^2)$
Polynomial	$\Phi(\mathbf{x}_i) \cdot \Phi(\mathbf{x}_j) = (\mathbf{p} + \mathbf{x}_i \cdot \mathbf{x}_j)^q$
Hybrid	$\Phi(\mathbf{x}_i) \cdot \Phi(\mathbf{x}_j) = (\mathbf{p} + \mathbf{x}_i \cdot \mathbf{x}_j)^q \exp(-\gamma \ \mathbf{x}_i - \mathbf{x}_j\ ^2)$
Sigmoidal	$\Phi(\mathbf{x}_i) \cdot \Phi(\mathbf{x}_j) = \tanh(k\mathbf{x}_i \cdot \mathbf{x}_j - \delta)$

Figure 12: Alternative kernels for SVR.[26]

2.3.2 Least Squares Support Vector Regression

Least squares support vector regression (LS-SVR) is a variation of SVR. This method was applied to register 3D CT brain scans taken pre-operatively with 2D ultrasound (US) images taken intra-operatively.[42] The process was divided into two stages. The pre-operative stage built a model that mapping the CT scan to a baseline US scan taken

before the operation. This stage minimized a MI metric. During the operation, a second US scan was taken. The model was applied to register the new US scan. It is unclear how the authors defined control points (CPs) on the CT and US images, but CPs were used to calculate the mean square error (MSE) and root mean square error (RMSE) in order to evaluate the quality of registration.

Another study compared the performance of LS-SVR to thin plate splines (TPS) for registering a pair of 2D MR images.[30] User defined CPs were identified in each image. LS-SVR was applied to create a model that mapped the two sets of control points. The resulting local non-rigid transformation was applied to the remaining pixels of the image to be moved. The average error and the RMSE were used to evaluate the quality of registration.

LS-SVR differs from SVR by replacing the e-insensitive loss function with a least squares loss function.[30] The primal formulation of the LS-SVR minimizes the quadratic objective function,

$$\frac{1}{2} \sum_{i=1}^n \omega_i^2 + \frac{1}{2} \gamma \sum_{i=1}^n e_i^2 \quad (10)$$

subject to the constraints

$$y_i = (\boldsymbol{\omega} \cdot \mathbf{x}_i + b) + e_i \quad (11)$$

where e_i are error terms and γ is the regularization constant.

Defining a Lagrangian function, the dual formulation of LS-SVR minimizes the quadratic objective function in equation (10).

$$\Lambda_D(\boldsymbol{\alpha}) = -\frac{1}{2} \sum_{i,j=1}^N (\alpha_i)(\alpha_j) \mathbf{x}_i \cdot \mathbf{x}_j + \frac{1}{2} \gamma \sum_{i=1}^n e_i^2 - \sum_{i=1}^N (\alpha_i)(\boldsymbol{\omega} \cdot \mathbf{x}_i + b + e_i - y_i) \quad (12)$$

subject to the constraints

$$\alpha_i \in [0, C] \quad (13)$$

$$\sum_{j=1}^N (\alpha_j) = 0 \quad (14)$$

Substituting in the partial derivatives for the Lagrangian function leads to the following support vector expansion

$$f(\mathbf{x}) = \sum_{i,j=1}^N (\alpha_i) \mathbf{x}_i \cdot \mathbf{x}_j + b \quad (15)$$

in which α and b can be found from the following system of linear equations:

$$\begin{bmatrix} 0 & \mathbf{1}^T \\ 1 & \mathbf{x}_i \cdot \mathbf{x}_j + \frac{1}{\gamma} \end{bmatrix} \begin{bmatrix} b \\ \alpha_i \end{bmatrix} = \begin{bmatrix} 0 \\ y_i \end{bmatrix} \quad (16)$$

The support vector expansion can be further modified using the “kernel trick”. The dot product term in equation (15) can be replaced by the dot product of more complex non-linear functions.

$$f(\mathbf{x}) = \sum_{i,j=1}^N (\alpha_i) \Phi(\mathbf{x}_i) \cdot \Phi(\mathbf{x}_j) + b \quad (17)$$

A major drawback with SVR is the need to use quadratic programming (QP) to solve an inequality constrained optimization problem. LS-SVR reformulates the problem in a way that solves a system of linear equations that utilize equality constraints. This change greatly reduces the computation time.

3 DATA SET

The dataset is comprised of 2D bright field images scanned from histological slides for 27 mice. A total of 135 images were provided by Genentech, Inc. for this study. Five images were scanned for each of the 27 mice. The tissue for each image was stained with one of the methods described in Section 3.1. The images vary in size with typical dimensions of 20,000 x 20,000 pixels. The images were acquired with a Hamamatsu Nanozoomer Digital Slide Scanner at a magnification of 20x (0.46 μm / pixel).

3.1 Tissue Staining

The hematoxylin & eosin (HE) stain provides the best delineation of tissue features and is relied on by pathologists for tissue diagnosis. Hematoxylin binds to acidic structures (DNA, RNA), staining the cell nuclei blue-purple. Eosin binds to basic cell structures, staining them pink-red.

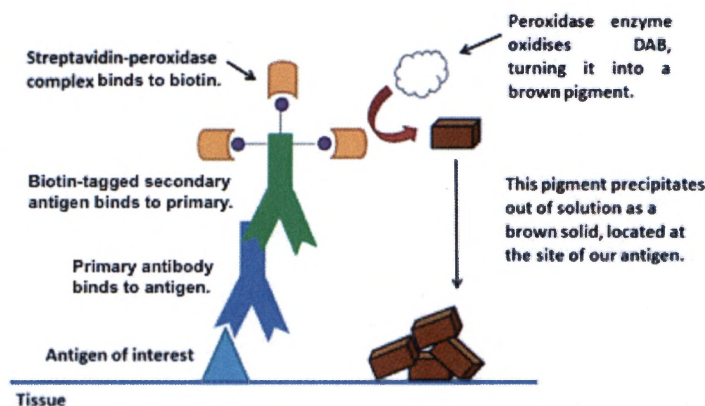


Figure 13: The dual antibody process for marking antigen locations with DAB (3,3'-diaminobenzidine). [20] Oftentimes, a single antibody cannot be found to directly connect the antigen to the marker.

The process for antigen staining with dual antibodies is illustrated in Figure 13. The first step is to attach a primary antibody to the antigen of interest. A secondary antibody with biotin tagging is then attached to the first antibody. A streptavidin-peroxidase conjugate binds to the biotin. DAB (3,3'-diaminobenzidine) in solution oxidizes on contact with the peroxidase portion of the conjugate producing a brown precipitate. This precipitate falls out of the solution, marking the site of the antigen.

The choice of target antigen depends on which biological structure is of interest. The antigens targeted in the images provided for this study are summarized in Table 1. Typically, the DAB is combined with a light hematoxylin counterstain to show other tissue features.

Table 1: Description of the antigen targets utilized in this study.

Acronym	Description
CD3	Best all-around T-cell marker that marks both helper and killer T-cells.
CD8	Cytotoxic T-cell marker.
MECA	A high endothelial venule (HEV) marker that stains all HEVs within lymphoid tissues and does not react with postcapillary venules or large vessels in spleen, thymus or non-lymphoid tissues.
GR1	The Gr-1 antigen is primarily a marker of myeloid differentiation. MDSC (myeloid-derived suppressor cells) help regulate the function of immune cell types such as T-cells.

Each different target antigen requires a series of unique chemical processes to bind the appropriate antibodies. These processes affect the appearance of the background staining as shown in Figure 14. Although our dataset uses different antigens than the

example figure, the concept still applies. For our dataset, the HE and MECA-32 stains delineated the features most clearly. However, these two groups of tissue samples were not sliced sequentially, so the feature variation is too great. The background staining of the CD3 and CD8 groups was weaker than the background staining for the GR1 group. Thus, the MECA32 and GR1 groups were chosen as the best adjoining sets of samples.

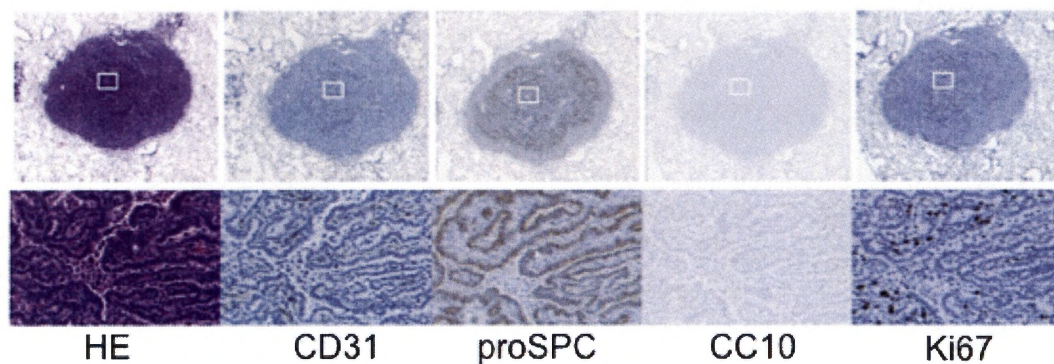


Figure 14: An example of how feature appearance varies with different antigen targets.[3]

3.2 Creating Sub-Images

A typical study consists of approximately twenty animals broken into four branches of five animals. Each animal provides a tissue sample to generate a whole image. The limited number of samples makes it difficult to statistically validate any performance improvement from using LS-SVR. Combining different studies to increase the total number of images can potentially lead to algorithm failure due to variability in the staining of different batches as described in Section 1.1.

Cropping a whole image to form multiple sub-images is an alternative way to generate more samples (see). Each sub-image is created by the author, who selected an isolated, smaller piece of tissue and defined the corner coordinates to crop a window around that tissue. Thirty-six pairs of sub-images were utilized in this study. For a detailed list of the images and the sub-images, refer to section 8.2 and section 8.3 in the Appendix.

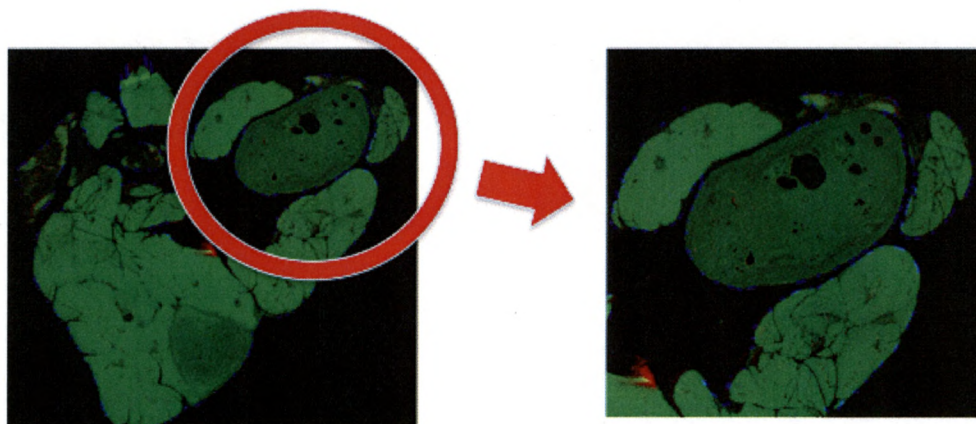


Figure 15: Cropping image to form sub-image.

3.3 Masking Sub-Images

Each sub-image has a piece of central tissue and additional tissue beyond the perimeter of the central tissue, as seen in Figure 16. The additional tissue is removed by the following process. A binary mask is created from background pixels over a certain threshold. Morphological operations, such as dilation and skeletonization, are applied to form a separation mask, which isolates each large piece of tissue in the sub-image. All pieces of tissue except the largest in area are discarded. The author chose each sub-image

window to guarantee that the piece of central tissue will be the largest in the sub-image. For more details about the masking process, refer to section 8.4 and section 8.5 in the Appendix.

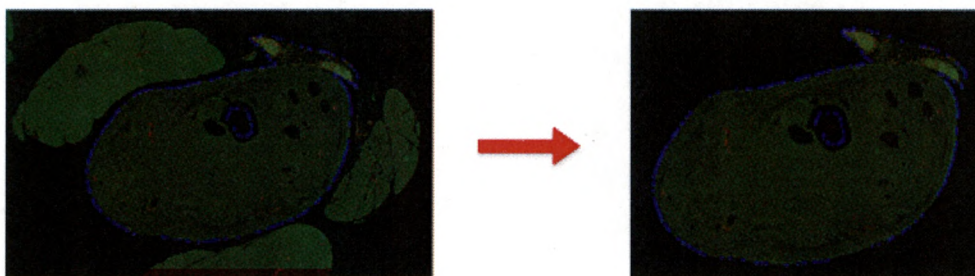


Figure 16: Masking sub-image by deleting anything besides the largest piece of tissue located in the center of the sub-image.

3.4 Perimeter Control Points

The characteristics of landmark-based registration were discussed in Section 2.1. Specifically, the correspondence between the two sets of matched features defines the transformation that is used to align the remaining pixels of the image. The features in this study are the surface non-uniformities of the tissue. Once the tissue is cross-sectioned, the grooves on the perimeter of the tissue become the features of interest. The bottom of a groove is equivalent to the vertex of an angle. These vertices can be automatically located by applying the Harris corner detector.[35] For this study, the detected vertices on the perimeter of the tissue are called perimeter control points (PCP's). An example of the automatically selected PCP's is shown in Figure 17.

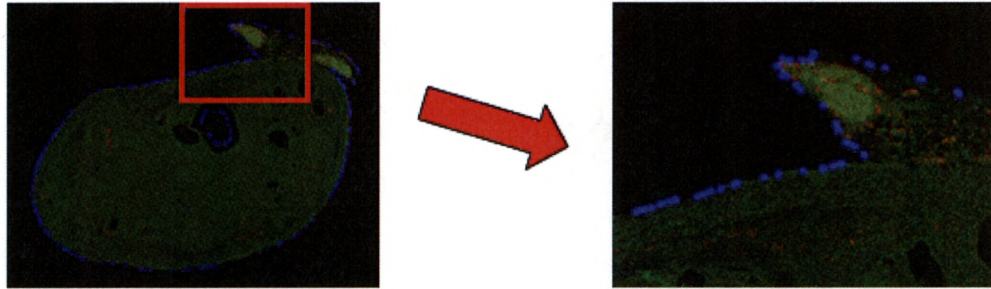


Figure 17: Perimeter control points automatically located by the Harris corner detector are marked by blue dots. The right image shows a higher magnification of the area in the red box.

3.5 Interior Control Points

The transformations described in Section 2.2 that only utilize PCP's lack sufficient accuracy. Interior control points (ICP's) are also necessary for improving registration accuracy. Unfortunately, the automatic selection of ICP's is a complex topic that is beyond the scope of this thesis. For this study, fifteen ICP's were manually selected by the author, who identified corresponding features in each pair of images and recorded their respective coordinates. For experiments that required five or ten ICP's, a subset of the fifteen ICP's was selected such that the ICP's maintained a uniform distribution across the tissue area. An example of the ICP distribution is shown in Figure 18.

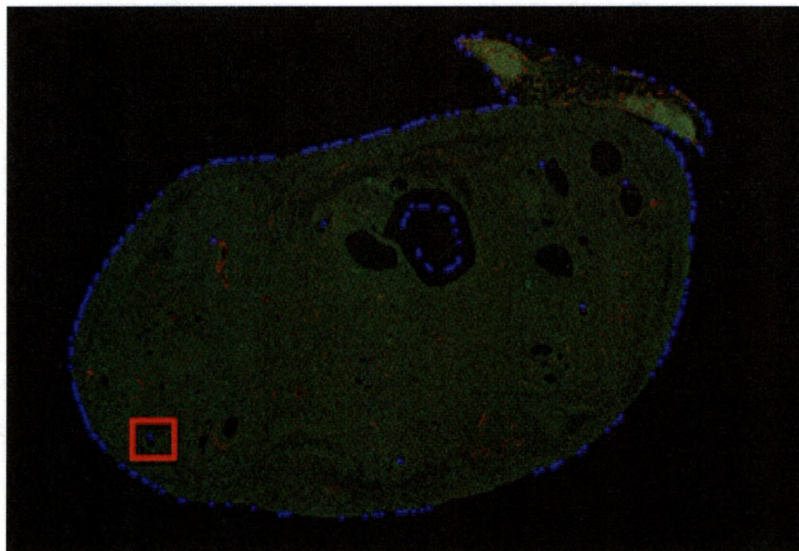


Figure 18: Interior control points (ICP's) distributed across tissue in a roughly uniform manner. The ICP's are represented by blue dots that are located in the green tissue. The red box highlights a single ICP.

4 PROPOSED METHOD

4.1 Concept

A hierarchical approach to registration can be described as a “coarse-to-fine” strategy, where the calculation of local registration is preceded by more global registration. The type of hierarchy can consist of increasing levels of data complexity, warp complexity or model complexity.[18] In this study, a three-level hierarchy of increasing model complexity was utilized. The first level centers the tissue. The second level makes minor adjustments in rotation and along the x and y axes. The third level locally warps the tissue.

4.2 Image Registration Process Flow

An overview of the process flow is shown in Figure 19. Stage 0 performs pre-transformation processing to isolate the tissue in the image. Stages 1 through 3 performs transformation of one image to bring it into closer registration with the other image. At the end of each transformation stage, metrics are calculated to evaluate the improvement in registration. The remainder of this section describes the details of each stage.

4.2.1 Stage 0: Pre-processing

Pre-processing prior to transformation begins with the retrieval of both images from the data storage. Both of the images are cropped to form matching sub-images as described in section 3.2. The central piece of tissue in each sub-image is isolated, while the remainder of the sub-image is masked off in the manner described in section 0.

Finally, binary masks of the central tissue are formed by combining intensity thresholds and morphological operations such as opening and closing to segment the tissue from the background.

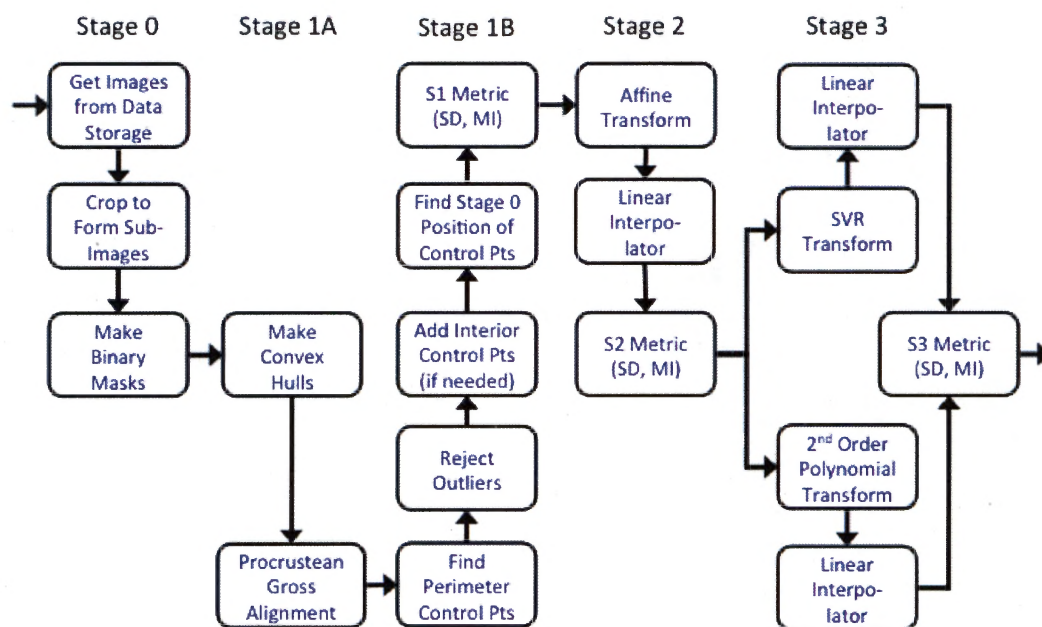


Figure 19: Image registration process flow at the completion of the study. A description of the stages is provided in Section 4.1.

4.2.2 Stage 1A: Gross Alignment

Gross alignment is the rough but robust registration between the pair of sub-images. The first step is to simplify the binary mask for each sub-image to a convex hull. A transform model is constructed by applying the Procrustian algorithm, which aligns the centroids of the convex hulls with the center of the largest image and rotates the hulls

until they overlap.[24] This gross alignment transform model is applied to both of the sub-images.

4.2.3 Stage 1B: Determine Control Points

The PCP's for each sub-image are automatically generated by applying a Harris corner detector as specified in section 3.4. Each control point in an image is matched to a corresponding control point in the other image by applying the correlation function described in section 4.4.3. Unmatched points are rejected as outliers. Manually matched ICP's, which are defined in section 1, are added to the set of points. The inverse of the gross alignment transform is applied to the control points to determine their positions at stage 0. The stage 0 position is needed to calculate the metrics that evaluate the registration performance of the gross alignment transform model.

4.2.4 Stage 2: Affine Transform

An affine transform model is generated from the matched sets of control points by using the *cp2tform* function in Matlab.[35] This affine transform model is applied to both of the sub-images. Any blank pixels in the post-transform image are filled in by the linear interpolation of neighboring pixels. At the end of this process, the metrics are applied to evaluate the registration performance of the affine transform model.

4.2.5 Stage 3 SVR: Least-Squares SVR Transform

An LS-SVR transform model is generated from the matched sets of control points by applying the library functions described in section 4.4.5. This LS-SVR transform model

is applied to both of the sub-images. Any blank pixels in the post-transform image are filled in by the linear interpolation of neighboring pixels. At the end of this process, the metrics are applied to evaluate the registration performance of the LS-SVR transform model.

4.2.6 Stage 3 Poly: Second Order Polynomial Transform

A second-order polynomial transform model is generated from the matched sets of control points by applying the *cp2tform* function in Matlab. This polynomial transform model is applied to both of the sub-images. Any blank pixels in the post-transform image are filled in by the linear interpolation of neighboring pixels. At the end of this process, the metrics are applied to evaluate the registration performance of the polynomial transform model.

4.3 Metrics

The analysis of an image-to-image metric provides a concrete way to evaluate the quality of registration. The metrics can be divided in two main groups: those based on the distance between extracted features points and those based on the intensity of gray levels in the image. Intensity-based techniques are theoretically more flexible, because they make use of the entire image content.[13]

4.3.1 Sum of Distances Over Control Points

The mean sum of distance (SD) metric, M_{SD} , is reported as the result of an experimental run. It is the average across all the pairs of sub-images as seen in equation

(18). The sum of distances metric is designed to have a more negative value with improving registration. This allows a gradient descent method to be applied to optimize the transform function.

$$M_{SD} = \frac{\sum_{k=1}^n M_{sub_image_k}}{n}, \text{ where } n = \# \text{ of } sub_images \quad (18)$$

The sum of distance metric for a pair of sub_images, $M_{sub_image_k}$, is calculated according to equation (19). The sum of distances after the LS_SVR or polynomial transform (stage 3) is subtracted from the sum of distances after the affine transform (stage 2). If the registration improves after the final transform, the difference should result in a negative value. This difference is divided by the sum of distances after gross alignment (stage 1). Dividing by the stage 1 sum normalizes the metric with respect to the number of control points. Otherwise, samples with a larger number of control points will show a greater difference than samples with fewer control points.

$$M_{sub_image_k} = \frac{\sum_{i=1}^m d_{non_lin_i} - \sum_{i=1}^m d_{affine_i}}{\sum_{i=1}^m d_{gross_i}} \quad (19)$$

where m is the number of matched control points.

The Euclidean distance between each pair of matched control points is calculated with the formula shown in Figure 20. An example of how the distances change between stages is shown in Figure 21.

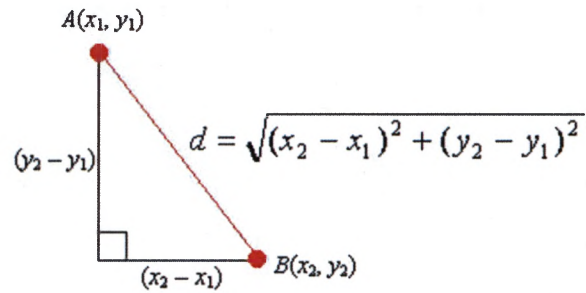


Figure 20: Calculate Euclidean distance between two points.[31]

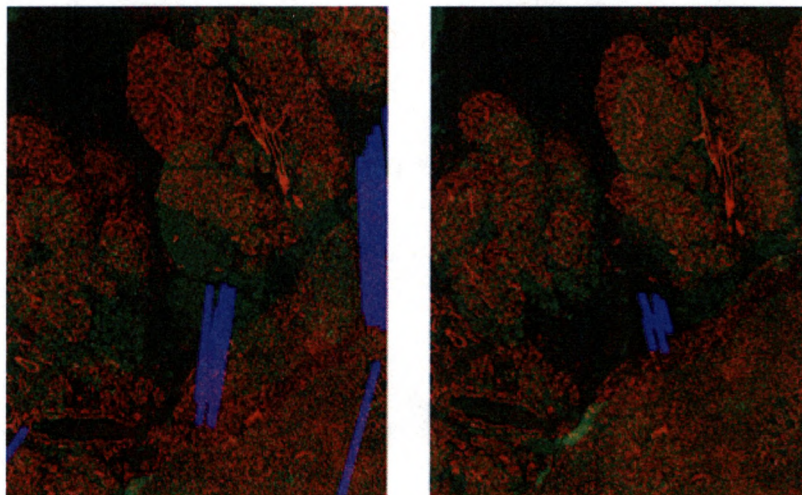


Figure 21: Example of how Euclidean distance changes with alignment. A pair of sub-images is shown in red and green. Each blue line shows the distance between a pair of matched PCP's. The left part of the figure shows the position of the sub-images prior to any registration. The greater degree of misalignment is reflected in the longer blue lines. The right part of the figure shows the respective positions after gross alignment. The blue lines grow shorter as the registration improves.

4.3.2 Mutual Information Concepts

Information theory applies the term marginal entropy as a measure of information in a single image.[33] An image with low marginal entropy would consist of almost a single intensity. This type of image contains little information, since there is no pattern or

variation. An image with high marginal entropy has larger quantities of multiple intensities. Such an image often contains a lot of information in spatial patterns. The marginal entropy for an image is computed by estimating the probability distribution of gray values over the pixels in the image.

$$H = \sum_i p_i \log \frac{1}{p_i} = -\sum_i p_i \log p_i \quad (20)$$

where p_i is the probability of a pixel having intensity i .

The concept of a joint histogram extends the definition of entropy to two images. A joint histogram will show clusters of gray values when two identical, grayscale images are correctly registered. A dispersion of the clusters appears as the images become misaligned due to structures in one image no longer overlapping their counterparts in the other image. The joint entropy for the joint distribution of two images is computed by estimating the probability distribution of gray values over the pixels in both images.

$$H = -\sum_{i,j} p_{i,j} \log p_{i,j} \quad (21)$$

where $p_{i,j}$ is the probability of a pixel having intensity i in image one and intensity j in image two.

Mutual information is an information theoretic technique that measures the amount of information one variable contains about another variable.[37] During the registration process, we are comparing the spatial alignment between a pair of images. The alignment of each image is represented by its individual marginal entropy as shown in Figure 22. The information from the overlapping images is described by the joint entropy. The goal is to explain as much of the individual alignments as possible during

the registration process by minimizing the joint entropy. Mutual information, $MI(M,N)$, is defined as the difference between the marginal entropies and the joint entropy.[5][18][44]

$$MI(M,N) = H(M) + H(N) - H(M,N) \quad (22)$$

where $H(M)$ and $H(N)$ are the marginal entropies of images M and N , $H(M,N)$ is the joint entropy between images M and N , and $MI(M,N)$ is the mutual information between images M and N .

Alternative formulations make use of conditional entropy, which is the probability of a pixel in image one having a gray value of i given a corresponding pixel in image two has a gray value of j .

$$MI(M,N) = H(M) - H(M|N) \quad \text{or} \quad MI(M,N) = H(N) - H(N|M) \quad (23)$$

where $H(M)$ and $H(N)$ are the marginal entropies of images M and N , $H(M|N)$ and $H(N|M)$ is the conditional entropy between images M and N , and $MI(M,N)$ is the mutual information between images M and N .

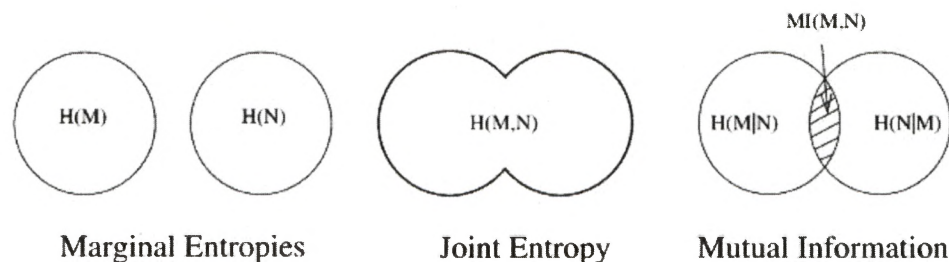


Figure 22: Mutual information as a function of the marginal and conditional entropies. For image M and N , the marginal entropies are defined as $H(M)$ and $H(N)$, the joint entropy is defined as $H(M,N)$, the conditional entropies are defined as $H(M|N)$ and $H(N|M)$ and the mutual information is defined as $MI(M,N)$. [41]

Measuring joint entropy and mutual information from our images undergoing registration poses some challenges. It is possible for the object of interest to be aligned, while the background may be misaligned. Figure 23 shows an example of this problem. Images m and n are registered based on the white circle. For both solution T_1 and T_2 , the circles are perfectly aligned. However, T_1 orients the images such that more of the gray background pixels overlap than T_2 . This results in different mutual information values despite the identical alignment of the white circles.

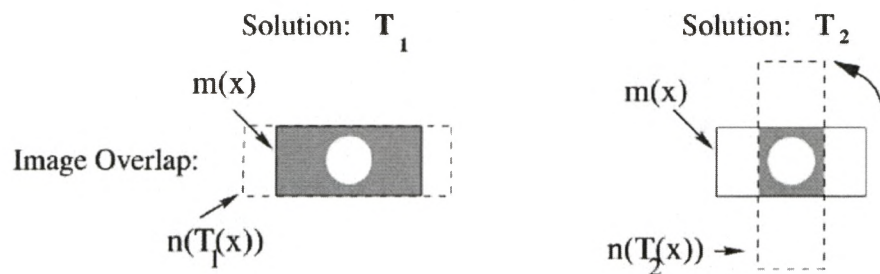


Figure 23: Orientation of background affects mutual information.[41] For solution T_1 and T_2 , the white circle is perfectly aligned. However, T_1 more overlap of the gray background pixels. This results in different mutual information values despite identical alignment of the circles.

In this study, this problem can occur when the control points are registered, but the pixels farther away from the CP's are not. It can also occur if the central tissue is registered correctly, while the other pieces of tissue are not.

The Normalized Mutual Information (NMI) metric was developed by Studholme, et al to provide a measure that was invariant to the changes in overlap.[41] NMI evaluates the ratio of the joint and marginal entropies:

$$NMI(M, N) = \frac{H(M)+H(N)}{H(M,N)} \quad (24)$$

Maximization of $NMI(M,N)$ searches for a transformation in which the joint entropy is minimized with respect to the marginal entropies. Registration is the process of finding the transform that minimizes the displacement, d , which can be expressed as:

$$d = \arg \max (NMI(M, N)) \quad (25)$$

An alternative formulation to equation (25) is:[27]

$$d = \arg \min (-NMI(M, N)) \quad (26)$$

For this work, the negative $NMI(M, N)$ from equation (26) is being calculated.

4.3.3 Mutual Information Over Entire Image

The mean mutual information (MI) metric over an image, M_{MI_img} , is reported as the result of an experimental run. It is the average across all the pairs of sub-images as seen in equation (27). The mutual information metric is designed to have a more negative value with improving registration. This allows a gradient descent method to be applied to optimize the transform function.

$$M_{MI_img} = \frac{\sum_{k=1}^n M_{sub_image_k}}{n} , \text{ where } n = \# \text{ of sub_images} \quad (27)$$

The MI metric for a pair of sub_images, $M_{sub_image_k}$, is calculated according to equation (28).

$$M_{sub_image_k} = \frac{negNMI_non_lin - negNMI_affine}{|negNMI_gross|} \quad (28)$$

The NMI after the LS_SVR or polynomial transform (stage 3) is subtracted from the NMI after the affine transform (stage 2). If the registration improves after the final transform, the difference should result in a negative value. This difference is divided by

the absolute value of the NMI after gross alignment (stage 1). Dividing by the stage 1 value normalizes the metric with respect to the size of the sample image. Otherwise, samples with larger images will show a greater difference than samples with smaller images.

4.3.4 Mutual Information Over Window

The evaluation of the LS-SVR transform in the local neighborhood of an interior control point (ICP) requires replacing the entire sub-image with a set of windows. Each window is centered on an ICP. A window is formed by manually cropping the sub-image to the appropriate dimensions as shown in Figure 24.

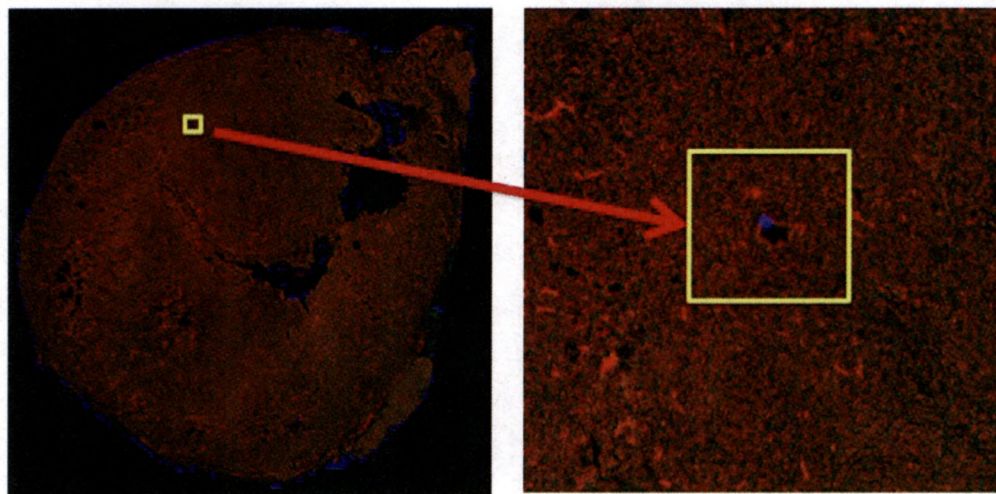


Figure 24: Cropping a window centered on an ICP. The blue point in the center of the box is the ICP. The yellow box outlines the boundary of the window.

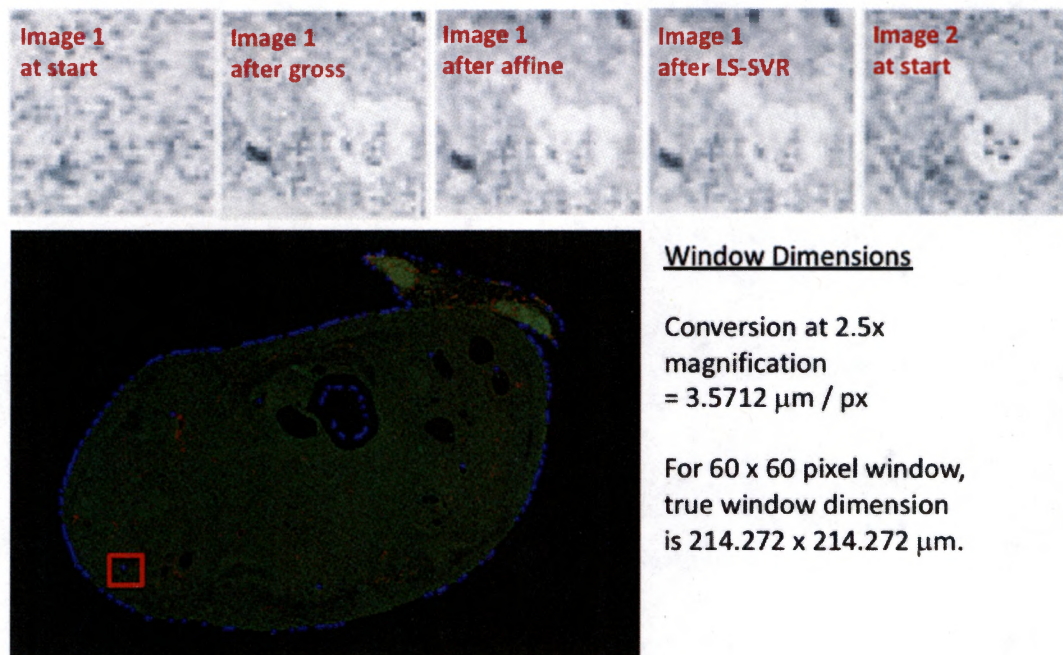


Figure 25: Window tissue changes appearance during registration process. The red box outlines the boundary of the window. The small square pictures on top illustrate the change in window appearance after each transform. The fourth and fifth pictures shows the similarity of the registered tissue to the target.

An example of how the tissue in the window changes is demonstrated in Figure 25. The red box on the green tissue outlines the boundary of the window. The series of the images at the top displays what happens during the registration process. The first square shows the appearance of the window from first image prior to registration. The second square shows the effect of gross alignment, while the third square shows the effect of the affine transform. The fourth square shows the final appearance after the LS-SVR transform. It closely resembles the square on the right, which is the target in the second image.

The window mutual information (MI) metric, M_{MI_win} , quantifies the registration of the tissue in the neighborhood of a sub-image's ICP's. It is calculated with equation (27) as described in section 4.3.3. The window MI metric also has a more negative value with improving registration.

There are two small differences between the window MI and the MI over the entire image. The first difference is the calculation of the MI for a sub-image. The window MI for a sub-image is the sum of the MI for each window in the sub-image as shown in equation (29).

$$M_{sub_img} = \frac{\sum_{j=1}^m M_j}{m} , \text{ where } m = \# \text{ of windows} \quad (29)$$

The second difference is the calculation of the MI for each window. The method is the same as equation (28) in section 4.3.3. However, only the part of the image in the window is used instead of the entire sub-image.

4.3.5 Testing Statistical Significance

The paired Student t-test is used to verify statistical significance when there is a single measurement variable and two nominal variables.[23] One of the nominal values can have two values. The other nominal variable is the multiple pairs of observations. This test checks if the mean difference in the multiple pairs is different from zero as null hypothesis. The null hypothesis is true when the mean difference is zero. In other words, the means of the two groups are equal.

The paired t -test assumes that the differences between pairs are normally distributed. The test does not assume that observations within each group are normal, only that the differences are normal.

The measurement variable is one of the three metrics described in sections 1.1.1, 4.3.3, and 4.3.4. The nominal value is the LS-SVR transform vs. the polynomial transform. For the SD and the MI over image metrics, each pair of sub-images is a pair of observations. For the window MI, each pair of windows for two corresponding sub-images is a pair of observations. The paired t -tests were performed using Microsoft Excel for Mac 2011 version 14.7.4.

4.4 Implementation

4.4.1 Computer Resources

The experiments in this study were conducted in a cluster computing environment at Genentech, Inc. Each pair of sub-images was registered by running a batch process on a single core of a Xeon CPU with 100 GB of dedicated RAM.

4.4.2 Software: Matlab

The software implementation for this study was written by me and compiled with Matlab version R2016b and its Image Processing Toolbox.

4.4.3 Software: Match Correlation

The Matlab functions for matching control points from different images and rejecting bad matches were written by Peter Kovesi.[15] These functions can be downloaded from his website at <http://www.peterkovesi.com/matlabfns/> .

The feature matching function is in the file *matchbycorrelation.m* . This function “generates putative matches between previously detected feature points in two images by looking for points that are maximally correlated with each other within windows surrounding each point. Only points that correlate most strongly with each other in both directions are returned. This is a simple-minded N^2 comparison.”[15]

The outlier rejection function is in the file *ransac.m* . This function is “a general purpose implementation of the RANSAC algorithm.” Random sample consensus (RANSAC) iteratively fits a model to a set of observed data. Points that do not fit the model are rejected as outliers and assumed to have no effect on the model.[9]

4.4.4 Software: Mutual Information

The Matlab function for calculating mutual information from different images was written by Dirk-Jan Kroon.[17] This function can be downloaded from the Mathworks website at <https://www.mathworks.com/matlabcentral/fileexchange/20057-b-spline-grid--image-and-point-based-registration> .

The function for calculating the mutual information between two images is in the file *image_difference.m*. This function outputs the registration error between the two images and an error image.

4.4.5 Software: Support Vector Regression

The Matlab functions for LS-SVR were written by a group based at the Katholieke Universiteit Leuven.[8] These functions can be downloaded from their website at <http://www.esat.kuleuven.be/sista/lssvmlab/>.

The basic workflow to generate the LS-SVR model is shown in Figure 26. This study makes use of the functional interface to tune the model parameters, train the model and simulate the results of applying the model to the image.

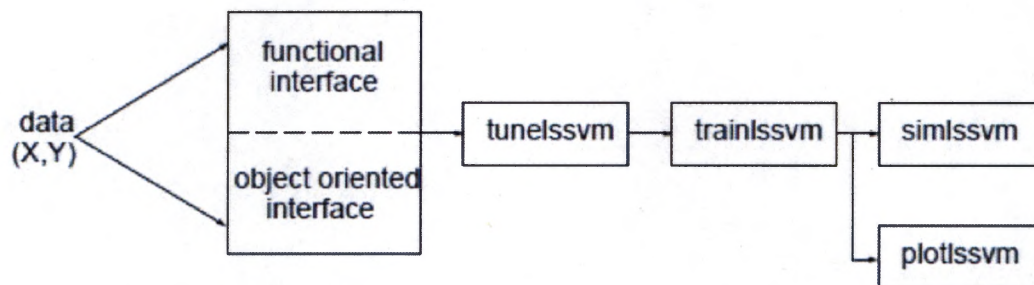


Figure 26: Workflow to generate a LS-SVR model.[8] This study uses the functional interface.

The tuning step searches for optimal values of two parameters: γ (gam), which is the regularization parameter that determines the trade-off between the training error minimization and smoothness of the estimated function, and σ^2 (sig2), which is the radial basis function (RBF kernel) parameter. The general syntax for the function call is:

$$[gam, sig2, cost] = tunelssvm(\{X,Y,type,[],[]\}, optfun, costfun, costargs)$$

My implementation required the x and y dimensions to be tuned independently, so the function was called twice. The options that I chose appear between the single quotes.

The specific syntax from my code is:

```

gam_x,sig2_x,cost_x] =
tunelssvm({X,Y_x,type,igam,isig2,'RBF_kernel','preprocess'},...
          'simplex','leaveoneoutlssvm',{'mse'});

[gam_y,sig2_y,cost_y] =
tunelssvm({X,Y_y,type,igam,isig2,'RBF_kernel','preprocess'},...
          'simplex','leaveoneoutlssvm',{'mse'});

```

The “preprocess” flag asks for coupled simulated annealing (CSA) to generate initial values for gam and sig2. According to the authors, CSA generates better starting points than random starts followed by gradient descent. During this study, it was observed that the initial values for gam and sig2 vary widely from run to run, creating inconsistent results.

The optimization flag allows the user to choose between “simplex” and “gridsearch”. The “simplex” option performs multidimensional, unconstrained, non-linear optimization. It works by finding a local minimum of a function, starting from an initial point X. The local minimum is located via the Nelder-Mead simplex algorithm, which does not require any gradient information.

The “gridsearch” option determines the best value of a cost function with possibly multiple minima by evaluating a grid over the parameter space and picking the set of parameters that results in the lowest cost. This procedure is supposed to iteratively shrink the grid space to zoom in to the candidate optimum. The starting values from the CSA determine the initial limits of the parameter space that will be searched.

The original version of the *tunelssvm* function only iterates once (i.e. search a single grid). I modified the *gridsearch.m* function in the library by increasing the maximum

number of function evaluations to allow iterative grid searches until the change in cost function drops below a specified value. This modification results in end values of gamma and sig2 that are reasonably close even when the initial values generated by CSA are far apart.

Training the LS-SVR model is straightforward once the tuning parameters have been determined. The specific syntax from my code is:

```
[alpha_x,b_x] = trainlssvm({X,Y_x,type,gam_x,sig2_x,'RBF_kernel'});
```

```
[alpha_y,b_y] = trainlssvm({X,Y_y,type,gam_y,sig2_y,'RBF_kernel'});
```

Note that the x and y dimensions are modeled independently.

The final step is to apply the LS-SVR model to the image. Since the x and y dimensions are being independently transformed, the image must be reshaped into a list of x-coordinates and y-coordinates. The specific syntax from my code is:

```
% Xtt is the x-y coord of pixels in a list
```

```
LSSVM_xtt = simlssvm({X,Y_x,type,gam_x,sig2_x,'RBF_kernel','preprocess'},...  
                    {alpha_x,b_x},Xtt);
```

```
LSSVM_ytt = simlssvm({X,Y_y,type,gam_y,sig2_y,'RBF_kernel','preprocess'},...  
                    {alpha_y,b_y},Xtt);
```

5 EXPERIMENTS

This study was divided into a series of six experiments that answer hypotheses for evaluating the merit of applying LS-SVR for registration of histological images in comparison to the standard baseline method utilizing a second order polynomial model.

Two thresholds will be used to determine statistical significance: A lower threshold of 0.05 (5.00 E-2) and a higher threshold of 0.001 (1.00 E-3). In sections 5.1 through 5.6, p-values that meet both thresholds will be highlighted in green. P-values that meet the lower threshold, but do not meet the higher threshold will be marked in yellow. P-values that do not meet either threshold will be marked in red.

5.1 Expt 1: Align Entire Image with Perimeter Control Points

The primary goal of the first experiment was to test the following hypothesis:
[Hypothesis 1] A local non-linear transform, such as the LS-SVR transform, registers histological images better than a global non-linear transform, such as the second-order polynomial transform. The secondary goal was to evaluate the effect on performance caused by the random starting point for optimizing the LS-SVR parameters.

5.1.1 Procedure

An experiment was designed to test Hypothesis 1 by comparing the results of applying both the multistage LS-SVR and polynomial registration algorithms to an image set that exceeded thirty samples to facilitate the testing of statistical significance. The set of 36 paired sub-images was generated by the process described in section 3.2. The

multistage algorithms described in section 4.1 relied strictly on automatically selected PCP's to register the sub-images. A successful test would suggest that completely automated processing of the whole image is feasible.

The second goal was tested by repeating the multistage LS-SVR registration five times. The repetition would expose any large fluctuations in the registration result. The polynomial registration was not repeated, because there is no random element. An alternative approach is to fix the starting point of the parameter optimization. However, that method could lead to sub-optimal registration for some image pairs that are dependent on the order in which the pairs are processed. A random starting point avoids this issue. More details regarding the optimization of the LS-SVR parameters can be found in section 4.4.5.

5.1.2 Results

The SD metric is evaluated for each LS-SVR and polynomial run according to the procedure described in section 4.3.1. Table 2 lists the LS-SVR results in column 2 and the polynomial result in column 3. The distance between paired PCP's decreases more quickly when applying the LS-SVR transform model. The p-value in column 4 shows that the difference between the two models is statistically significant.

Table 2: Expt 1 results - sum of distance for PCP's. Distance between paired PCP's decreases more quickly for the LS-SVR transform model.

Expt 1: Sum of Distances for PCP's			
	LS-SVR	Polynomial	p-value
Run 1	-0.1652	-0.0687	4.73 E-9
Run 2	-0.1653		2.22 E-9
Run 3	-0.1652		3.20 E-9
Run 4	-0.1647		2.69 E-9
Run 5	-0.1640		2.62 E-9

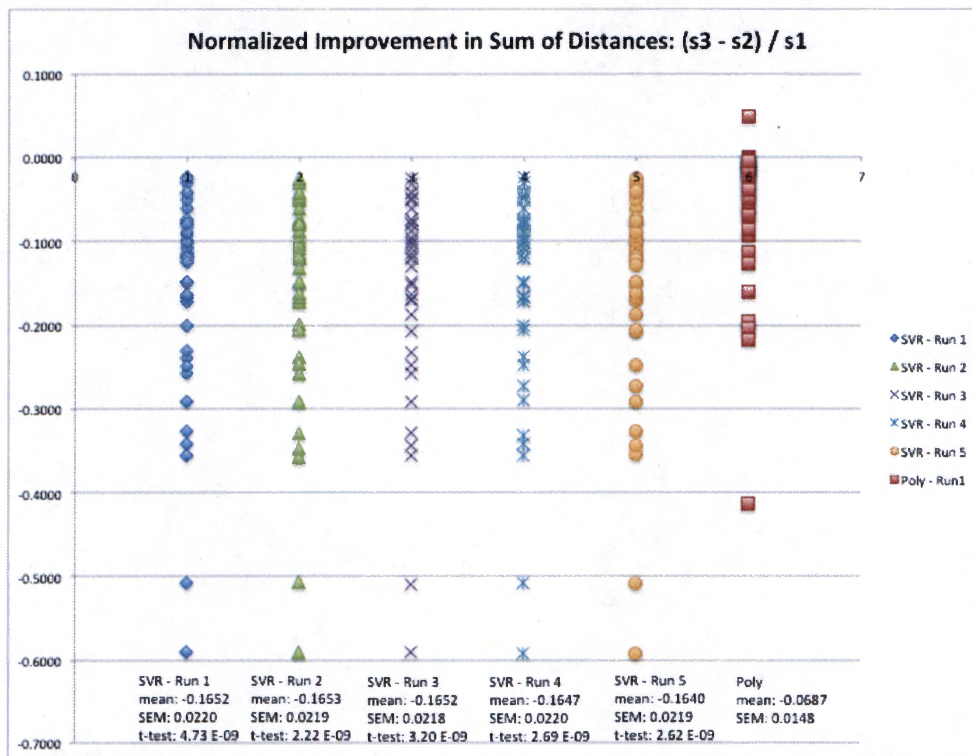


Figure 27: Expt 1 results - sum of distances for PCP's. First five columns are the LS-SVR results, while the right-most column is the polynomial result. Each point is the result for a sub-image pair.

A graphical representation of the SD metric is shown in Figure 27. The first five columns of points show the LS-SVR results, while the column on the right shows the polynomial result. Each point is the result of registering a sub-image pair. The mean of each LS-SVR run is lower than the mean of the polynomial run. The run-to-run variability of the LS-SVR results is minimal as shown by the standard error of the mean (SEM) values.

The MI metric over the entire image is evaluated for each LS-SVR and polynomial run according to the procedure described in section 4.3.3. Table 3 shows the MI decreases more quickly when applying the polynomial transform model and the difference between the two models is statistically significant.

Table 3: Expt 1 results - mutual information over entire image. MI decreases more quickly for the polynomial transform model.

Expt 1: Mutual Information Over Entire Image			
	LS-SVR	Poly	p-value
Run 1	0.0603	-0.0026	2.90 E-11
Run 2	0.0591		1.78 E-11
Run 3	0.0599		2.23 E-11
Run 4	0.0580		1.56 E-11
Run 5	0.0589		4.57 E-11

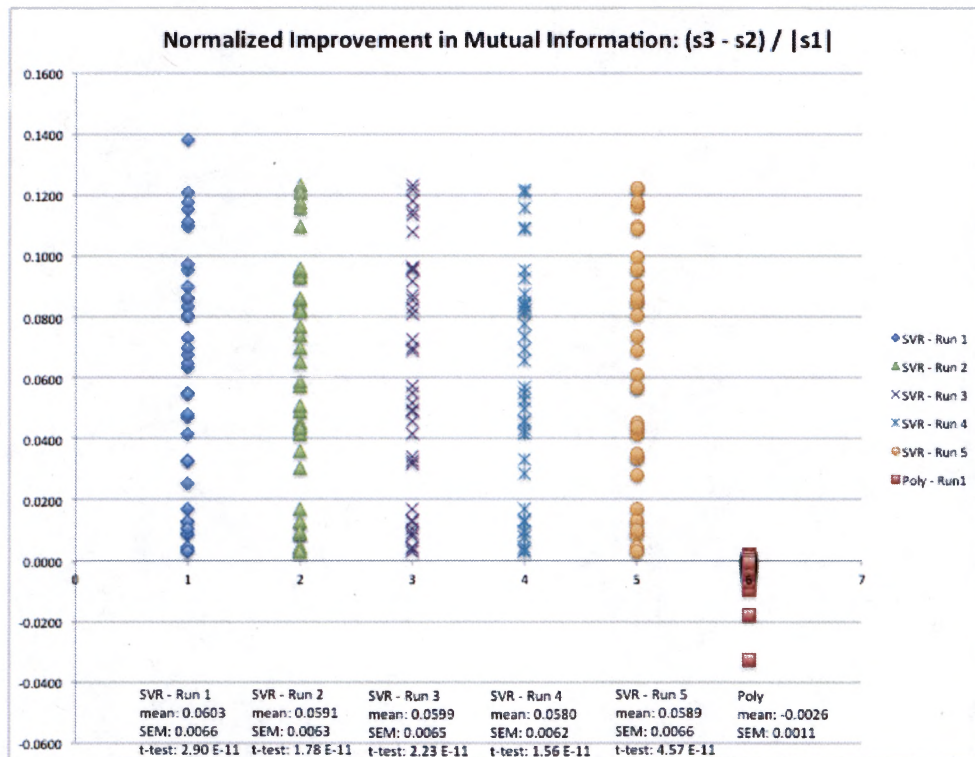


Figure 28: Expt 1 results - mutual information over entire image. First five columns are the LS-SVR results, while the right-most column is the polynomial result. Each point is the result for a sub-image pair.

A graphical representation of the registration improvement is shown in Figure 28.

The mean of each LS-SVR run is greater than the mean of the polynomial run. The run-to-run variability of the LS-SVR results is minimal as shown by the standard error of the mean (SEM) values.

5.1.3 Discussion

The results of experiment 1 were mixed with respect to the primary goal of testing whether a LS-SVR transform performs better non-linear registration than a polynomial transform over the entire image. The LS-SVR model was better at aligning the PCP's, but worse at aligning the entire image.

A possible cause for this difference is an artifact created by the generation of sub-images. Cropping the original image leaves portions of tissue around the central tissue of interest. It is believed that the pixels outside of the central tissue are not registered well, because the LS-SVR model is extrapolating beyond the PCP's. Without the control points to regulate the model, the extrapolation can be inaccurate.

The results of experiment 1 were definitive with respect to the secondary goal of evaluating the variability caused by the random starting point for optimizing the LS-SVR parameters. The mean improvement for both the SD and MI metrics stays within a narrow range over all five of the LS-SVR runs as seen in Table 2 and Table 3. In addition, the distribution of the improvement for each sub-image remains consistent as seen in Figure 27 and Figure 28.

It was not necessary to repeat the polynomial run five times. In spite of a random number generator used in the match correlation code described in section 4.4.3, the rejection of outlier control points is consistent between runs. Thus, the polynomial result does not change from run to run. This result will be demonstrated in experiment 3.

5.2 Expt 2: Align Masked Image with Perimeter Control Points

The primary goal of the second experiment was to test the following hypothesis:
[Hypothesis 2] The pixels outside of the tissue area negatively affect the registration metric for the entire image.

5.2.1 Procedure

An experiment was designed to test Hypothesis 2 by comparing the results of applying both the multistage LS-SVR and polynomial registration algorithms to the set of 36 paired sub-images generated by the process described in section 3.2. Each sub-image was masked using the procedure specified in section 0 to remove all tissue except the central piece. Transform models were generated from automatically selected PCP's. The multistage LS-SVR registration was run three times to verify the results were repeatable.

5.2.2 Results

5.2.2.1 With Outlier

The SD metric is evaluated for each LS-SVR and polynomial run according to the procedure described in section 4.3.1. Table 4 lists the LS-SVR results in column 2 and the polynomial result in column 3. The distance between paired PCP's decreases more quickly when applying the LS-SVR transform model. The difference between the two columns quantifies the improvement in PCP registration.

Table 4: Expt 2 results with outlier - sum of distances for PCP's. Distance between paired PCP's decreases more quickly for the LS-SVR transform model.

Expt 2: Sum of Distances for PCP's			
	LS-SVR	Poly	p-value
Run 1	-0.1781	-0.0663	5.21 E-9
Run 2	-0.1774		7.32 E-9
Run 3	-0.1772		6.41 E-9

The MI metric over the entire image is evaluated for each SVR and polynomial run according to the procedure described in section 4.3.3. Table 5 shows the MI is getting worse with both models, but the decline is smaller when applying the polynomial transform model. The result of the t-tests in column show that the difference in model performance is not statistically significant. A graphical representation of the registration deterioration is shown in Figure 29.

Table 5: Expt 2 results with outlier - mutual information over masked image. MI declines more slowly for the polynomial transform model, but the results are not statistically significant.

Expt 2: Mutual Information Over Masked Image			
	LS-SVR	Poly	p-value
Run 1	0.0030	0.0005	7.52 E-2
Run 2	0.0023		1.14 E-1
Run 3	0.0026		1.45 E-1

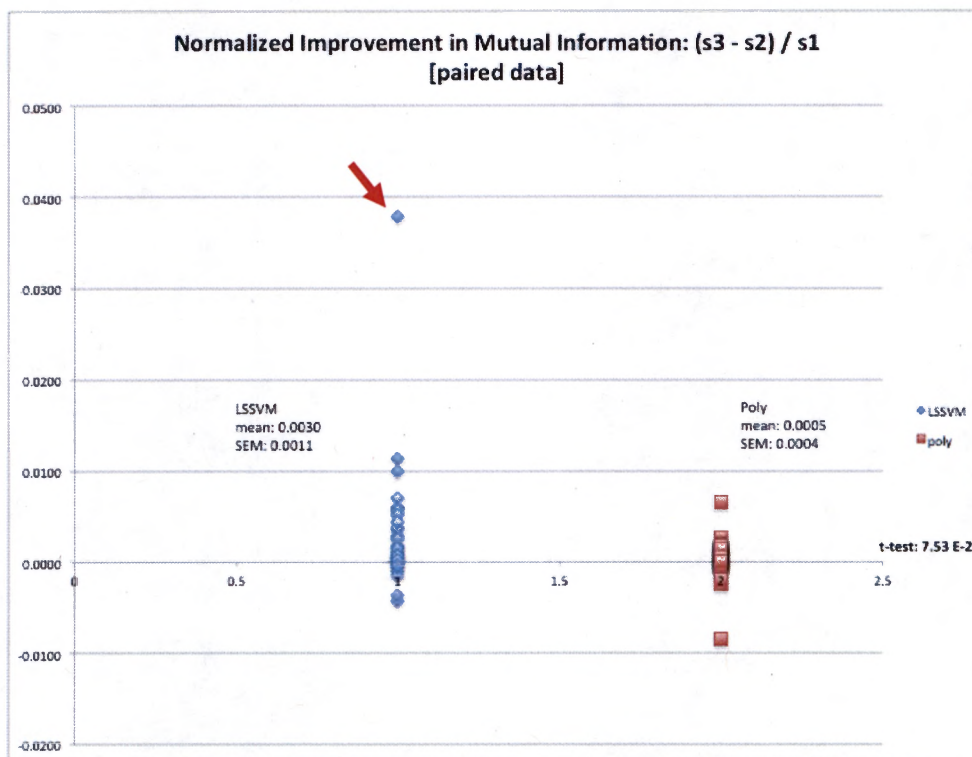


Figure 29: Expt 2 results with outlier - mutual information over masked image. Red arrow points to outlier present in the LS-SVR results on left.

5.2.2.2 Without Outlier

An outlier is clearly visible in Figure 29. The outlier elevates the mean MI for the LS-SVR model. It also increases the SEM, which makes it more difficult to determine statistical significance by inflating the p-values.

The outlier was traced back to the sub-image pair, 18WN/18XI subset 1. The root cause for the outlier is the uneven distribution of PCP's around the perimeter of the tissue. The LS-SVR model is unconstrained in the areas without PCP's, resulting in the incorrect transform shown in Figure 30.

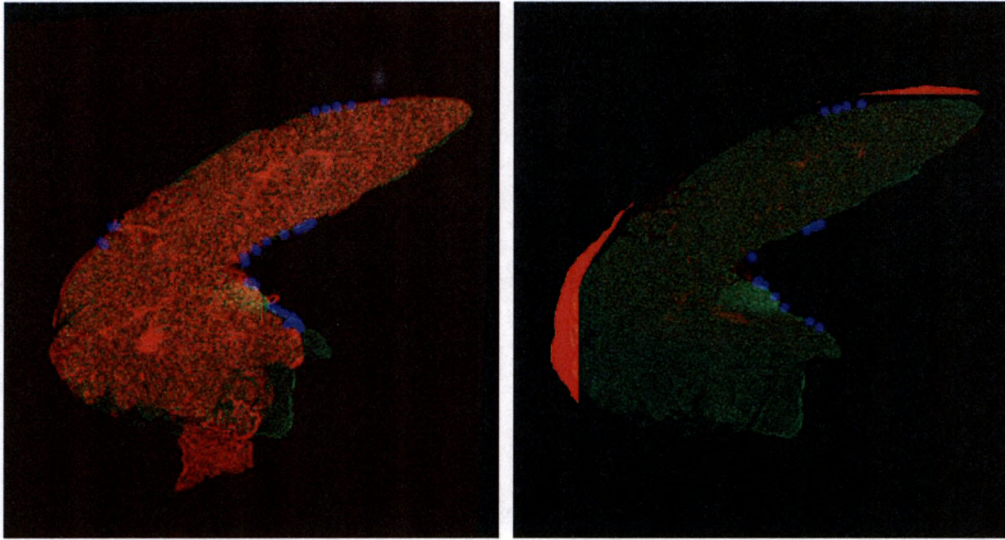


Figure 30: Poor LS-SVR registration due to uneven distribution of PCP's. Outlier traced to sub-image pair, 18WN/18XI subset 1. Left side shows red tissue prior to transform. Right side shows distorted red tissue from incorrect transform.

After removing the outlier, the SD metric is re-evaluated for each LS-SVR and polynomial run according to the procedure described in section 4.3.1. Comparing Table 6 to Table 4, there is no effect on the registration of the PCP's by removing the outlier.

Table 6: Expt 2 results without outlier - sum of distances for PCP's. Distance between paired PCP's decreases more quickly for the LS-SVR transform model.

Expt 2: Sum of Distances for PCP's (removed outlier)			
	LS-SVR	Poly	p-value
Run 1	-0.1771	-0.0702	8.20 E-9
Run 2	-0.1763		1.17 E-8
Run 3	-0.1761		1.01 E-8

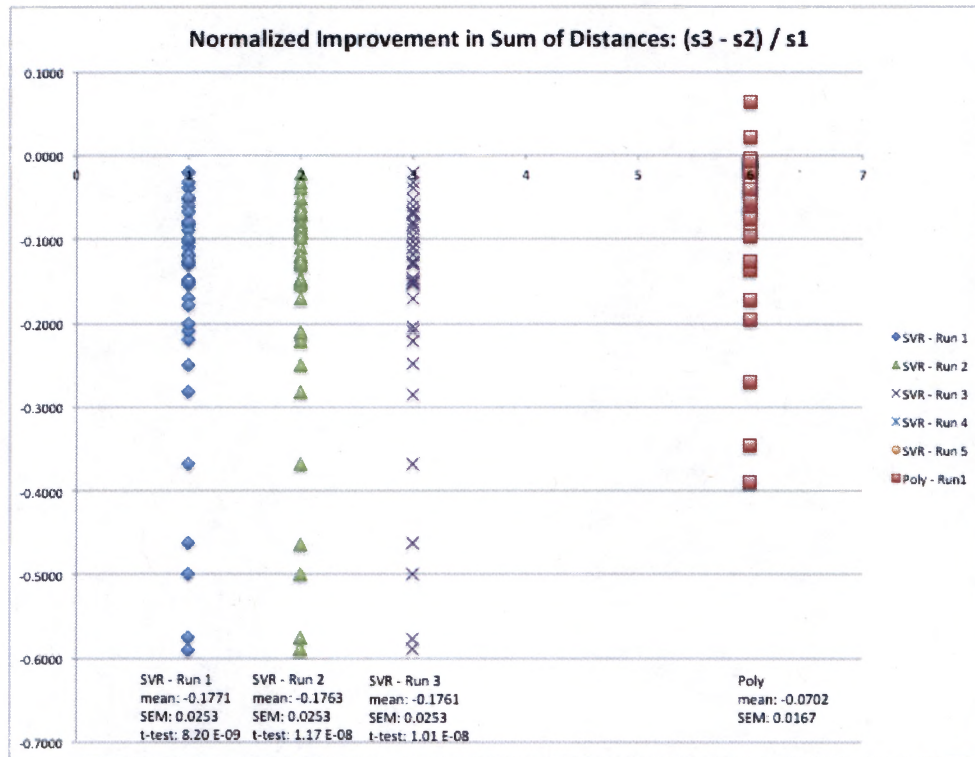


Figure 31: Expt 2 results without outlier - sum of distances PCP's. First three columns are the LS-SVR results, while the right-most column is the polynomial result. Each point is the result for a sub-image pair.

A graphical representation of the SD metric is shown in Figure 31. The mean of each LS-SVR run is lower than the mean of the polynomial run. The run-to-run variability of the LS-SVR results is minimal as shown by the standard error of the mean (SEM) values.

After removing the outlier, the MI metric over the entire image is also re-evaluated for each LS-SVR and polynomial run according to the procedure described in section 4.3.3. Comparing Table 7 to Table 5, the LS-SVR performance improved by removing the outlier. However, Table 7 still shows the MI is getting worse with both models, and the decline is smaller when applying the polynomial transform model.

Table 7: Expt 2 results without outlier - mutual information over masked image. MI decline for LS-SVR improved after removing outlier, but MI continues to decline more slowly for the polynomial transform model.

Expt 2: Mutual Information Over Masked Image (removed outlier)			
	LS-SVR	Poly	p-value
Run 1	0.0020	0.0007	2.21 E-2
Run 2	0.0015		4.34 E-2
Run 3	0.0015		5.25 E-2

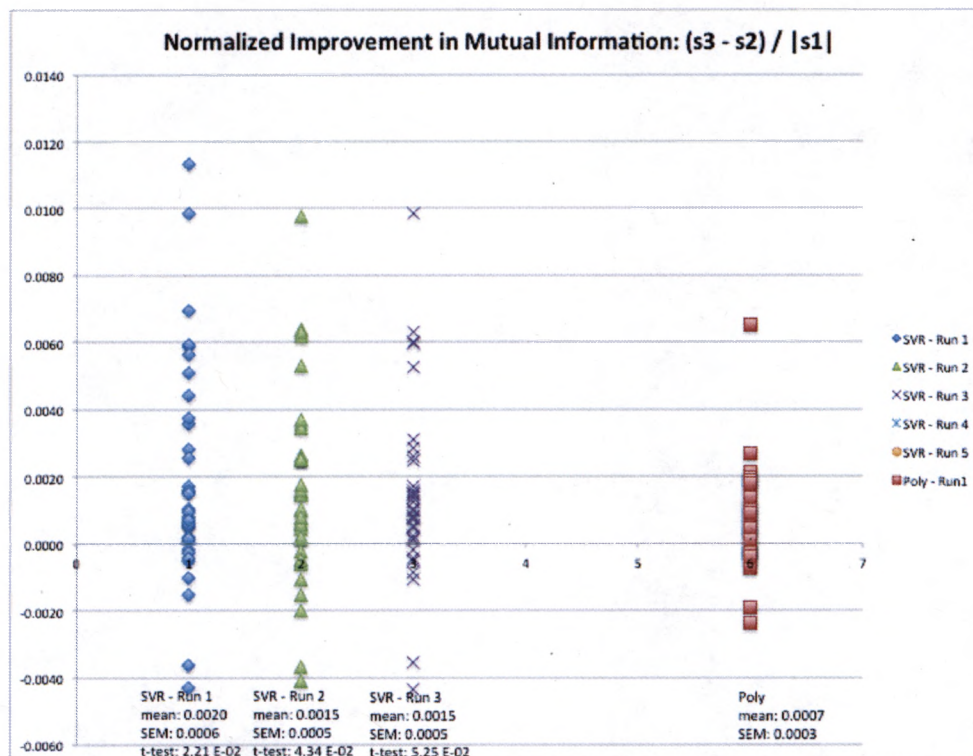


Figure 32: Expt 2 results without outlier - mutual information over masked image. First three columns are the LS-SVR results, while the right-most column is the polynomial result. Each point is the result for a sub-image pair.

The result of the t-tests has marginally improved. The difference between the two models continues to be statistically insignificant at the higher threshold of $1.0 \text{ E-}3$.

However, two of the three LS-SVR runs underperform the polynomial run in a statistically significant manner at the lower threshold of 5.0×10^{-2} .

A graphical representation of the registration improvement is shown in Figure 32. The mean of each LS-SVR run continues to be greater than the mean of the polynomial run. The run-to-run variability of the LS-SVR results remains minimal.

5.2.3 Discussion

The results of experiment 2 continued to show mixed results with respect to the goal of testing whether a LS-SVR transform performs better non-linear registration than a polynomial transform over a masked version of the image. The LS-SVR model was better at aligning the control points, but still worse at aligning the entire masked image. It should be noted that the comparison of registration over the masked image is of questionable statistical significance, even after removing the outlier.

The effect of masking the image outside of the central tissue can be seen by comparing Table 7 to Table 3. There is a distinct decrease in the registration improvement for the LS-SVR transform, supporting the idea that the unmasked pixels were skewing the LS-SVR results. However, the MI is positive, which means the image registration still got worse after the transform. In contrast, the polynomial transform showed a distinct increase in the MI metric, suggesting that the unmasked pixels were contributing to better polynomial results. The polynomial MI metric also turned positive, which means the image registration got worse after the polynomial transform.

The decline in the performance of both models can be explained by their fundamental properties. The LS-SVR model provides a non-linear transform that is weighted more strongly in the neighborhood of the control points. For pixels outside of the neighborhood, the LS-SVR model extrapolates behavior with corresponding inaccuracies from lack of regularization. Since the size of the neighborhood is not clear, it is possible that control points within the interior of the tissue must be added to act as a regularization constraint. The ultimate extension of this concept is to make every pixel in the tissue a control point. In that case, the LS-SVR model transforms every pixel perfectly, and the registration is already solved.

The polynomial model represents the non-linear transform as an equation. For pixels beyond the perimeter, this equation limits inaccuracies by regulating the transformation. However, within the perimeter, the same equation limits the registration accuracy. The masking process in experiment 2 only retained the pixels within the perimeter, effectively removing information from the MI metric. The remaining pixels could only be registered with limited accuracy. The addition of interior control points should increase the complexity of the equation, thereby improving the accuracy.

5.3 Expt 3: Align Masked Image with Perimeter and 10 ICP's

The primary goal of the third experiment was to test the following hypothesis:
[Hypothesis 3] The addition of interior control points (ICP's) improves the performance of the LS-SVR model. The secondary goal was to verify the repeatability of the polynomial runs.

5.3.1 Procedure

An experiment was designed to test Hypothesis 3 by comparing the results of applying the LS-SVR and polynomial registration algorithms to the set of 36 paired sub-images that were masked to remove all tissue except the central piece. Transform models were generated from automatically selected PCP's and ten manually selected ICP's. Both the LS-SVR and polynomial registration were run three times to verify the results were repeatable.

5.3.2 Results

The SD metric is evaluated for each LS-SVR and polynomial run according to the procedure described in section 4.3.1. Table 8 shows the distance between paired PCP's and ICP's decreases more quickly when applying the LS-SVR transform model. A graphical representation of the SD metric is shown in Figure 33. The left three columns of points show the LS-SVR results, while the right three columns show the polynomial results. There is no run-to-run variability in the polynomial results.

Table 8: Expt 3 results - sum of distances for PCP's + 10 ICP's. Distance between paired PCP's and ICP's decreases more quickly for the LS-SVR transform model.

Expt 3: Sum of Distances for PCP's + 10 ICP's			
	LS-SVR	Poly	p-value
Run 1	-0.1398	-0.0645	4.53 E-9
Run 2	-0.1413	-0.0645	6.44 E-9
Run 3	-0.1399	-0.0645	2.11 E-9

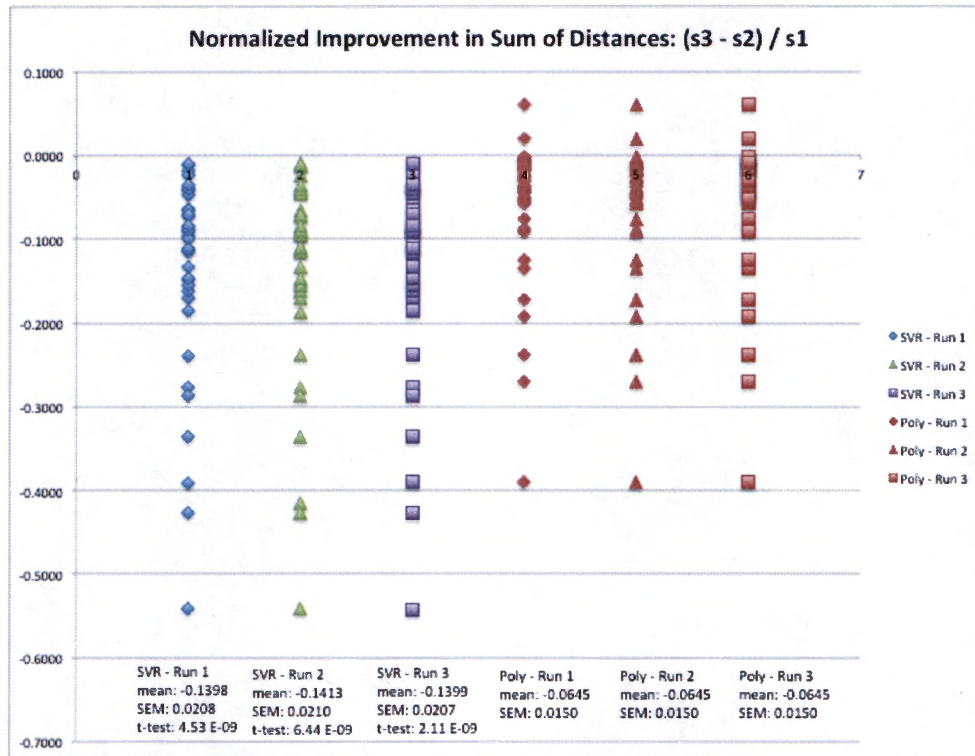


Figure 33: Expt 3 results - sum of distances for PCP's + 10 ICP's. Left three columns are the LS-SVR results, while the right three columns are the polynomial results. Each point is the result for a sub-image pair.

The MI metric over the entire image is evaluated for each LS-SVR and polynomial run according to the procedure described in section 4.3.3. Table 9 shows the MI decreases more quickly when applying the LS-SVR transform model. The difference between the two models is statistically significant at the lower threshold of 5.0 E-2. However, the difference in two of the three LS-SVR runs is still not statistically significant at the higher threshold of 1.0 E-3.

Table 9: Expt 3 results - mutual information over masked image for PCP's + 10 ICP's. MI decreases more quickly for the LS-SVR transform model.

Expt 3: Mutual Information Over Masked Image for PCP's + 10 ICP's			
	LS-SVR	Poly	p-value
Run 1	-0.0003	0.0006	7.30 E-4
Run 2	-0.0002	0.0006	2.37 E-3
Run 3	-0.0001	0.0006	7.95 E-3

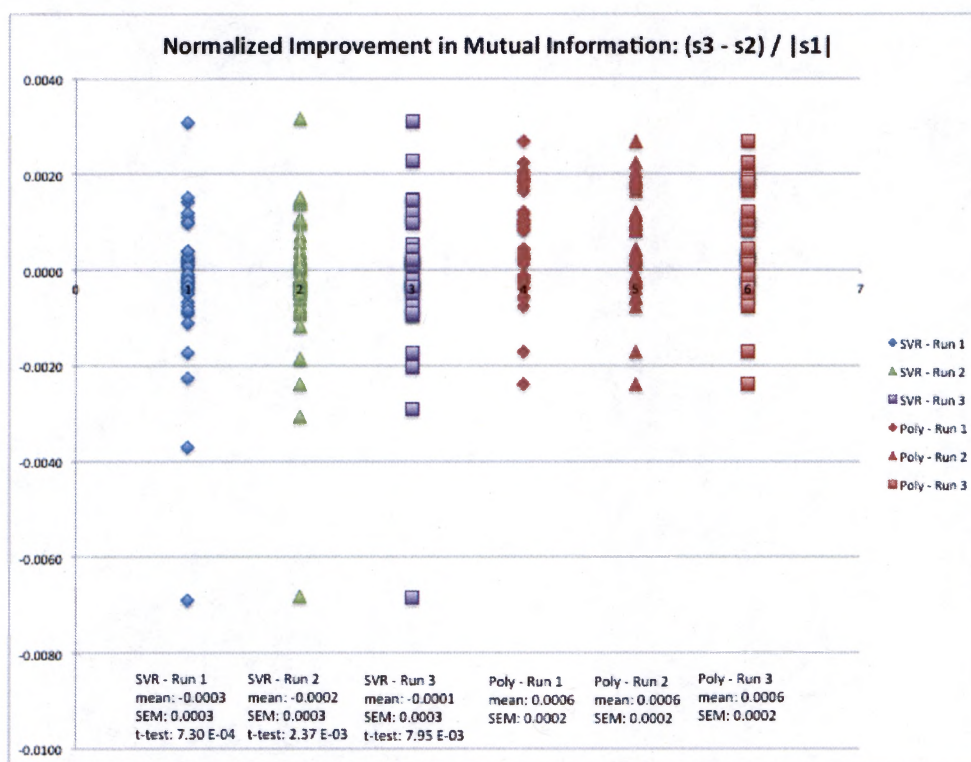


Figure 34: Expt 3 results - mutual information over masked image for PCP's + 10 ICP's. Left three columns are the LS-SVR results, while the right three columns are the polynomial results. Each point is the result for a sub-image pair.

A graphical representation of the registration improvement is shown in Figure 34.

The mean of each LS-SVR run is less than the mean of each polynomial run.

5.3.3 Discussion

At last, the results of experiment 3 show that a LS-SVR transform performs better non-linear registration than a polynomial transform over a masked version of the image when control points are distributed across the tissue. The LS-SVR model was better at aligning the control points and at aligning the entire masked image. However, the comparison of registration over the masked image shows some issues with statistical significance at the higher t-test threshold. In addition, the absolute improvement in the overall image registration is minimal as shown in Table 9.

The issue of neighborhood size is believed to be the root cause of both the higher p-values and minute improvement in registration by the LS-SVR model. As mentioned section 2.3.1, the LS-SVR model utilizes a Gaussian kernel that more heavily weights the model in the neighborhood of a control point. The accuracy of the model decreases with increasing distance from a control point. If the neighborhood size is small and the other nearest control points are far away, the model will be extrapolating new pixel positions with insignificant regularization.

The higher p-value is a function of increased variability when comparing the LS-SVR results to the polynomial results. The polynomial results show negligible fluctuation from run to run as seen in Figure 34. In contrast, the LS-SVR results show varying degrees of scatter from run to run. The scatter is attributed to extrapolation inaccuracies that prevent the LS-SVR model from converging on the same solution. The convergence process is described in section 4.4.5.

The minimal improvement in registration by using the LS-SVR model can be explained by another aspect of the neighborhood. Not only does the accuracy of the model decrease, the influence of the model also decreases with increasing distance from a control point. If the neighborhood size is small, pixels outside of the neighborhood may not be significantly moved by the transform. Since this type of pixel comprises the majority of the image, little change is apparent after applying the LS-SVR transform.

In order to evaluate the neighborhood effect, a new metric must be developed to measure the registration performance in the neighborhood of the control points. The LS-SVR model is expected to show a greater improvement in performance with this metric.

5.4 Expt 4: Evaluate 60x60 Pixel Window Around 10 ICP's

The primary goal of the fourth experiment was to test the following hypothesis: [Hypothesis 4] The LS-SVR model performs better than the polynomial model in the neighborhood of the ICP's.

5.4.1 Procedure

An experiment was designed to test Hypothesis 4 by comparing the results of applying the LS-SVR and polynomial registration algorithms to the masked sub-image dataset. Transform models were generated from automatically selected PCP's and ten manually selected ICP's. A new metric, described in section 4.3.4, was created to measure the MI in a window around each ICP. A window length of 60 pixels was chosen because the actual dimension of 214 μm is larger than the diameter of common cells.

5.4.2 Results

The MI metric over the 60 x 60 pixel window is evaluated for each LS-SVR and polynomial run according to the procedure described in section 4.3.4. Table 10 shows the window MI decreases more quickly when applying the LS-SVR transform model. It also shows the window MI becomes worse with both models, although the decline is much smaller when applying the LS-SVR model.

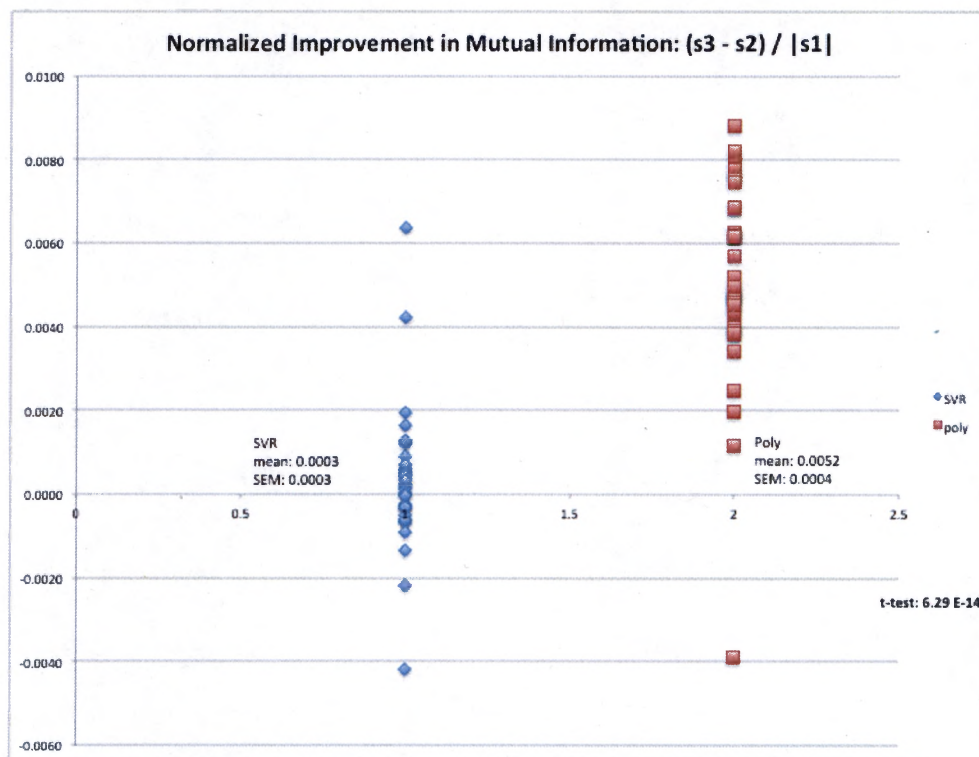


Figure 35: Expt 4 results – mutual information in 60x60 windows around 10 ICP's. Left column is the LS-SVR result, while the right column is the polynomial result. Each point is the result for a sub-image pair.

Table 10: Expt 4 results – mutual information in 60x60 windows around 10 ICP's. Window MI declines more slowly for the LS-SVR model.

Expt 4: Mutual Information in 60x60 Windows Around 10 ICP's				
	LS-SVR	Poly	LS-SVR - Poly	p-value
Perimeter + 10 Interior CP's	0.0003	0.0052	-0.0048	6.29 E-14

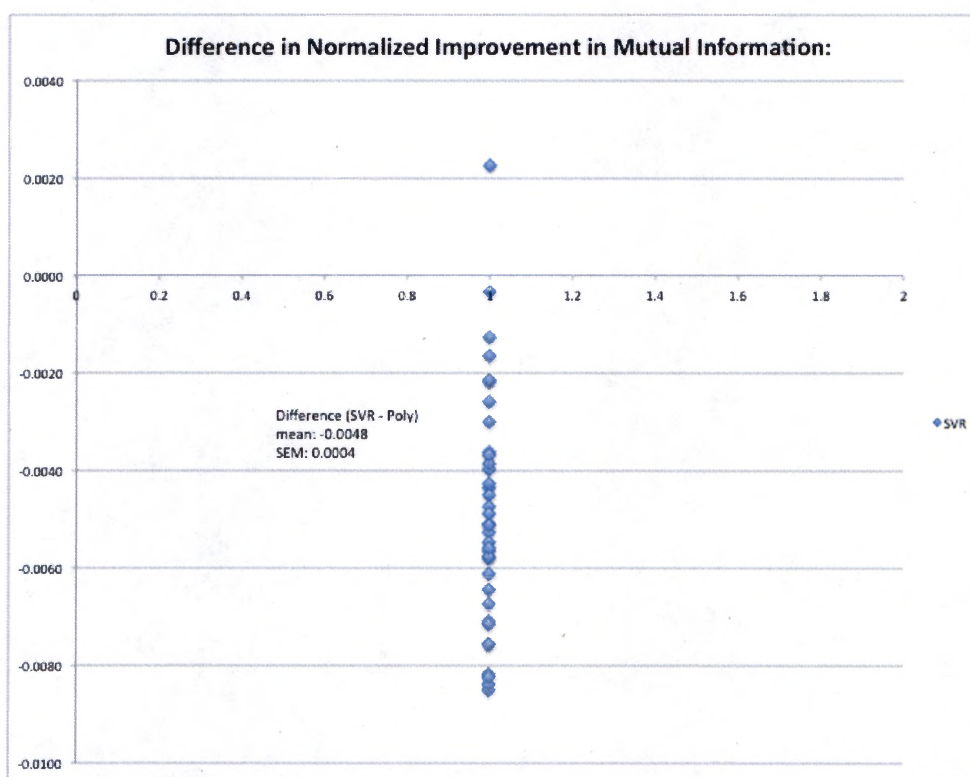


Figure 36: Expt 4 results – MI difference in 60x60 windows around 10 ICP's. For almost all sub-image pairs, the LS-SVR model improves registration of the window pixels.

A graphical representation of the window MI metric is shown in Figure 35. The mean of the LS-SVR run is greater than the mean of the polynomial run. The difference between the two models can be visualized by subtracting the polynomial result from the

LS-SVR result for each sub-image pair as shown in Figure 36. For almost all sub-image pairs, the LS-SVR model is better than the polynomial model at improving the registration of the window pixels.

5.4.3 Discussion

The results of experiment 4 show that the LS-SVR model performs better non-linear registration than the polynomial model in the neighborhood of the ICP's. The difference in performance is statistically significant at both t-test thresholds. This outcome supports the concept that localized non-linear registration should outperform global non-linear registration.

The LS-SVR model also shows a positive window MI in Table 10, which indicates that the registration within the window is getting worse. In contrast, the experiment 3 results in Table 9 show a negative MI across the entire image, which indicates that the registration across the entire image is getting better. It seems contradictory that the LS-SVR model performs worse locally, but better overall.

The apparent contradiction can be explained by making the following two assumptions. First, the LS-SVR transform only affects the pixels local to the control point. Second, the LS-SVR transform performs more accurately with increasing numbers of nearby control points. A detailed justification for these assumptions can be found in sections 5.5.3 and 5.6.4. Based on these assumptions, it is possible for the registration improvement to be distributed in the manner shown in Figure 37.

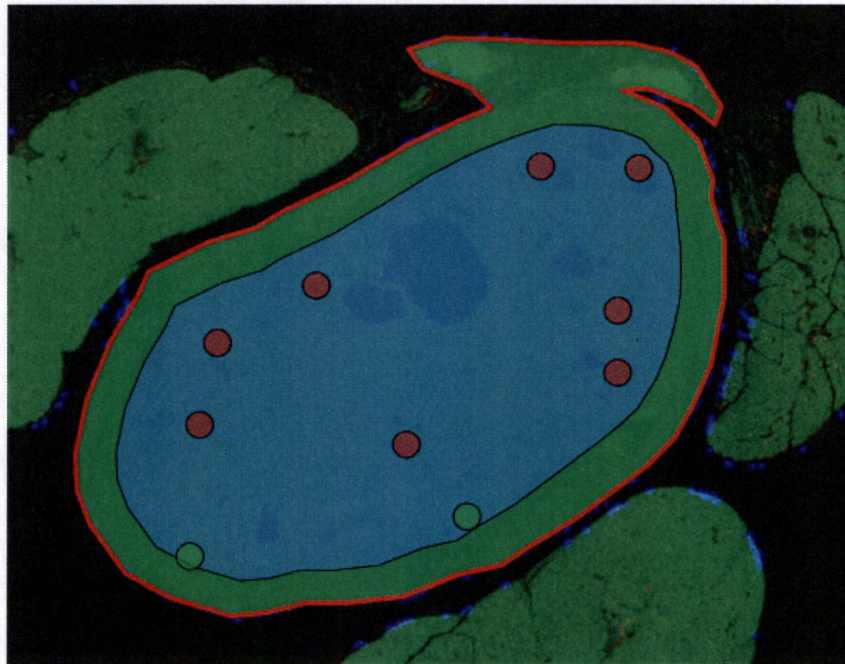


Figure 37: Registration change assuming the LS-SVR transform has a limited radius. The green outer region shows pixels near the PCP's with a negative MI metric. The blue central region shows pixels too far from any CP's to be affected by the LS-SVR transform. The circles inside the blue region highlight the areas near the ICP's that are affected by the LS-SVR transform. A red circle shows pixels with a positive MI metric. A green circle shows pixels with a negative MI metric.

The green outer region of Figure 37 highlights the pixels neighboring the PCP's, where the negative MI metric represents a registration improvement. The blue central region highlights the pixels that are too far from any control points to be affected by the LS-SVR transform. These pixels remain unmoved from their positions at the end of the affine transform. The circles inside the blue region highlight the areas near the ICP's that are affected by the LS-SVR transform. A red circle is an area where a positive MI metric represents registration deterioration. A green circle is an area where a negative MI metric represents registration improvement.

The positive window MI is visually exhibited by the eight red circles versus the two green circles. The negative MI over the entire image is exhibited by the green outer region plus the green circles minus the red circles.

5.5 Expt 5: Evaluate 60x60 Pixel Window Around 5/10/15 ICP's

The primary goal of the fifth experiment was to test the following hypothesis:
[Hypothesis 5] Increasing the number of ICP's improves the performance of the LS-SVR model in the neighborhood of each ICP.

5.5.1 Procedure

An experiment was designed to test Hypothesis 5 by comparing the results of applying the LS-SVR and polynomial registration algorithms to the masked sub-image dataset. Transform models were generated from automatically selected PCP's and varying numbers of manually selected ICP's. Five, ten and fifteen ICP's were selected for this experiment. The window MI metric described in section 4.3.4 was applied to a 60 x 60 pixel window around each ICP.

5.5.2 Results

The SD metric is evaluated for each LS-SVR and polynomial run according to the procedure described in section 4.3.1. Table 11 shows the distance between paired PCP's and ICP's decreases more quickly when applying the LS-SVR transform model. Figure 38 shows a graphical representation of the SD metric. The left three columns of points show the LS-SVR results, while the right three columns show the polynomial results.

Table 11: Expt 5 results - sum of distances for PCP's + varying ICP's. Distance between paired PCP's and ICP's decreases more quickly for the LS-SVR transform model.

Expt 5: Sum of Distances for PCP's + Varying ICP's			
	LS-SVR	Poly	p-value
Perimeter + 5 Interior CP's	-0.1452	-0.0636	8.07 E-7
Perimeter + 10 Interior CP's	-0.1398	-0.0645	4.53 E-9
Perimeter + 15 Interior CP's	-0.1317	-0.0631	8.98 E-8

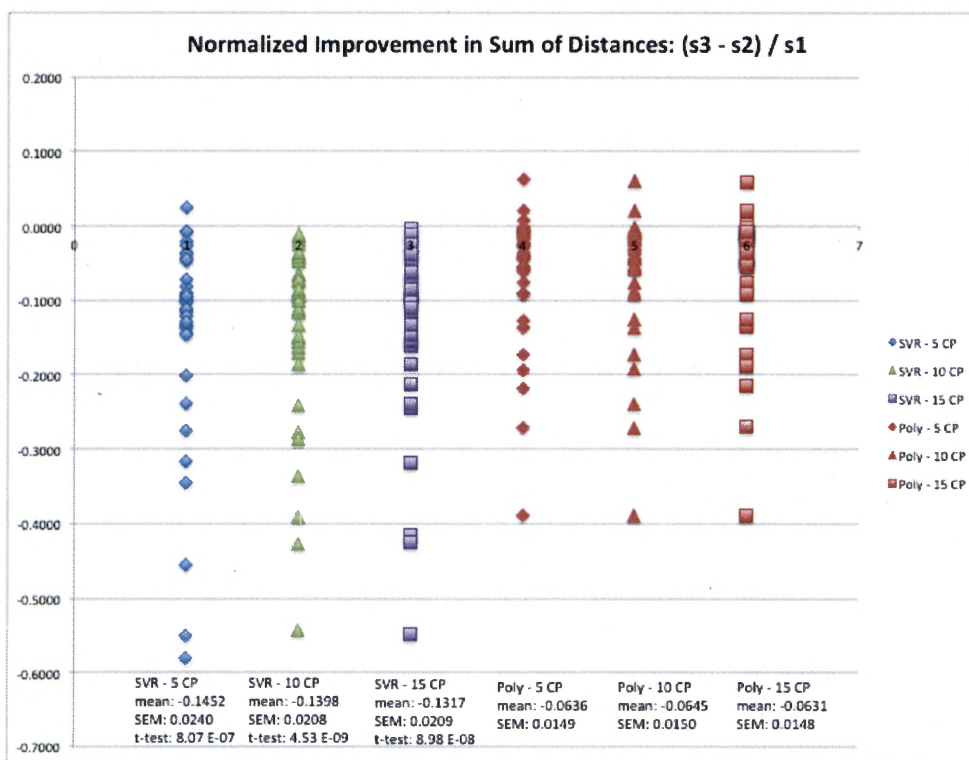


Figure 38: Expt 5 results - sum of distances for PCP's + varying ICP's. Left three columns are the LS-SVR results, while the right three columns are the polynomial results. Each point is the result for a sub-image pair.

The MI metric over the entire image is evaluated for each LS-SVR and polynomial run according to the procedure described in section 4.3.3. Table 12 shows the MI decreases more quickly when applying the LS-SVR transform model. Furthermore, the overall registration is improving with the LS-SVR model, while it is getting worse with the polynomial model. The difference between the two models is statistically significant at the lower threshold of 5.0 E-2. However, the difference in two of the three LS-SVR runs is still not statistically significant at the higher threshold of 1.0 E-3. A graphical representation of the registration improvement is shown in Figure 39.

Table 12: Expt 5 results - mutual information over masked image for PCP's + varying ICP's. MI decreases more quickly for the LS-SVR transform model.

Expt 5: Mutual Information Over Masked Image for PCP's + Varying ICP's			
	SVR	Poly	p-value
Perimeter + 5 Interior CP's	-0.0002	0.0005	1.58 E-2
Perimeter + 10 Interior CP's	-0.0003	0.0006	7.30 E-4
Perimeter + 15 Interior CP's	-0.0001	0.0006	2.32 E-3

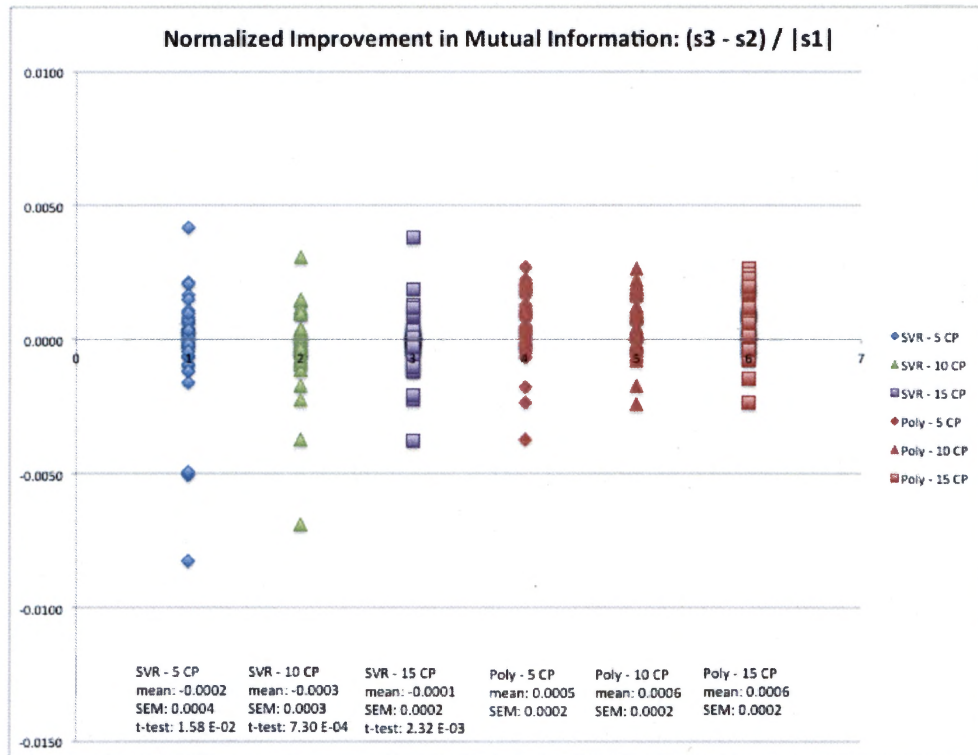


Figure 39: Expt 5 results - mutual information over masked image for PCP's + varying ICP's. Left three columns are the LS-SVR results, while the right three columns are the polynomial results. Each point is the result for a sub-image pair.

The MI metric over the 60 x 60 pixel window is evaluated for each LS-SVR and polynomial run according to the procedure described in section 4.3.4. Table 13 shows the window MI decreases more quickly when applying the LS-SVR transform model. Furthermore, the window MI improves with additional ICP's.

Table 13: Expt 5 results - mutual information in 60x60 windows around varying ICP's. For the LS-SVR model, window MI improves with additional ICP's.

Expt 5: Mutual Information in 60x60 Windows Around Varying ICP's				
	LS-SVR	Poly	LS-SVR - Poly	p-value
Perimeter + 5 Interior CP's	0.0013	0.0047	-0.0033	3.40 E-6
Perimeter + 10 Interior CP's	0.0003	0.0052	-0.0048	6.29 E-14
Perimeter + 15 Interior CP's	-0.0003	0.0047	-0.0050	2.27 E-12

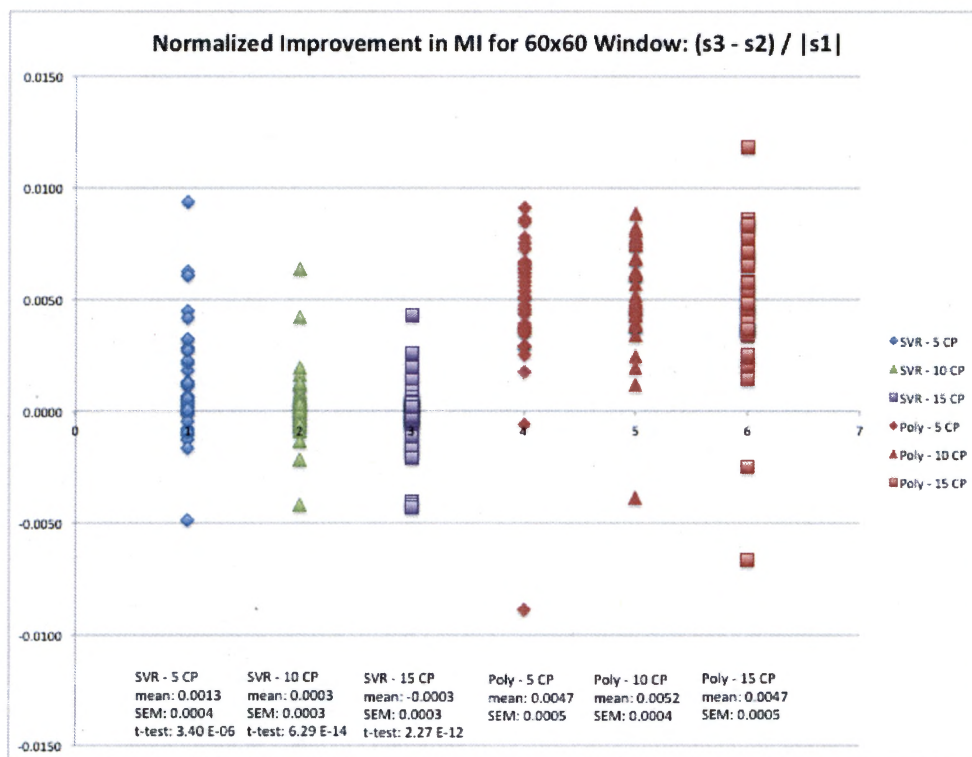


Figure 40: Expt 5 results - mutual information in 60x60 windows around varying ICP's. Left three columns are the LS-SVR results, while the right three columns are the polynomial results. Each point is the result for a sub-image pair.

A graphical representation of the window MI is shown in Figure 40. The mean of each LS-SVR run is less than the mean of each polynomial run. The difference between the two models can be visualized by subtracting the polynomial result from the LS-SVR result for each sub-image pair as shown in Figure 41. The MI difference increases with an increasing number of ICP's.

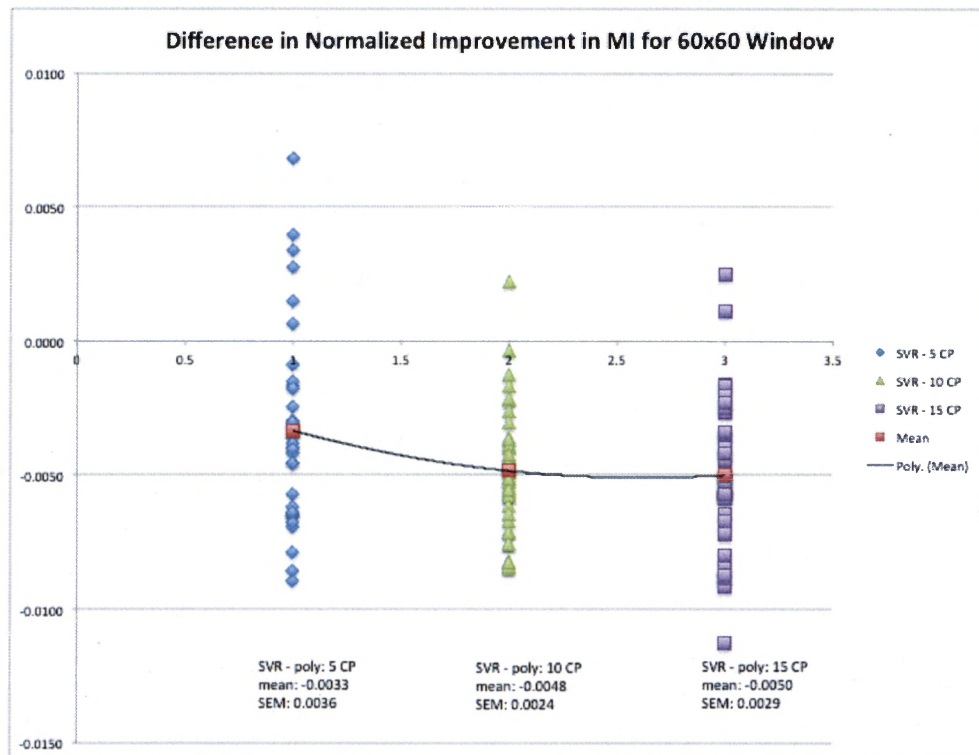


Figure 41: Expt 5 results – MI difference in 60x60 windows around varying ICP's. The MI difference increases with additional ICP's.

5.5.3 Discussion

Experiment 5 tests the effect of increasing the number of ICP's. The sum of distances metric shows a decrease in mean improvement as the number of ICP's is increased. This trend suggests that the model overfits the PCP's. As the number of ICP's increases, the overall registration improves at the expense of the PCP registration.

The negative mean improvement for MI across the entire image does not appreciably change with the number of ICP's. It is believed that the large area near the perimeter has a negative mean improvement, while the small areas near the ICP's have a positive mean improvement as shown in Figure 37. If the perimeter area is much larger than the sum of the small interior areas, the mean improvement for MI across the entire image will be unaffected by an increase in the number of ICP's.

The mean improvement for window MI moves from positive to negative with increasing numbers of ICP's. This trend reflects the improving accuracy of the LS-SVR transform in the area near the ICP's as illustrated in Figure 42. Since the effect of the transform is weighted by the number of nearby control points, the windows closest to the perimeter turn negative first with improving model accuracy.

The MI difference (LS-SVR – Poly) also decreases with additional ICP's, but Figure 41 suggests that it may be asymptotically approaching a final value. Unfortunately, the three levels of ICP's are insufficient to determine if this is the case.

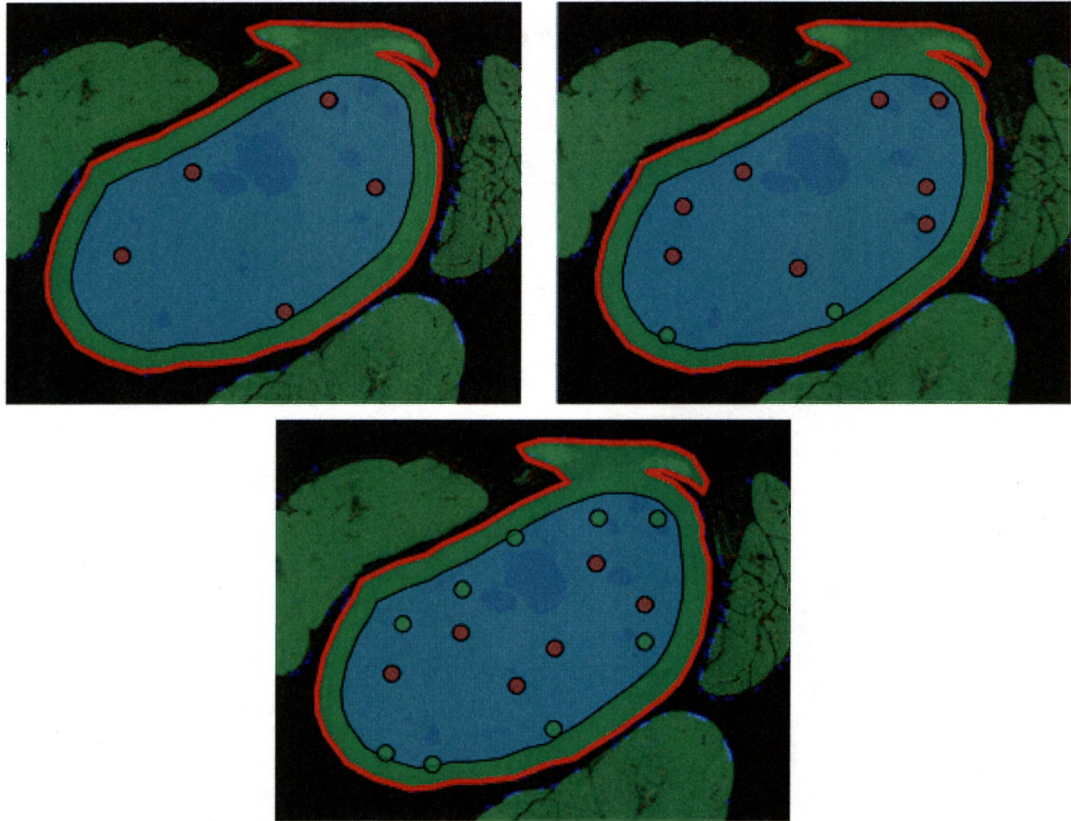


Figure 42: The LS-SVR window MI improves with increasing number of ICP's with greatest improvement near the perimeter. The green outer region shows pixels near the PCP's with a negative MI metric. The blue central region shows pixels too far from any CP's to be affected by the LS-SVR transform. The circles inside the blue region highlight the areas near the ICP's that are affected by the LS-SVR transform. A red circle shows pixels with a positive MI metric. A green circle shows pixels with a negative MI metric.

5.6 Expt 6: Evaluate 60x60/120x120/180x180 Pixel Windows Around 5/10/15 ICP's

The primary goal of the sixth experiment was to test the following hypothesis:

[Hypothesis 6] Increasing the number of ICPs improves the performance of the LS-SVR model in a wider neighborhood around each ICP.

5.6.1 Procedure

An experiment was designed to test Hypothesis 6 by comparing the results of applying the LS-SVR and polynomial registration algorithms to the masked sub-image dataset. Transform models were generated from automatically selected PCP's and varying numbers of manually selected ICP's. Three quantities of ICP's, five, ten and fifteen, were selected for this experiment. For each quantity of ICP's, the window MI metric described in section 4.3.4 was applied to varying window sizes around each ICP. Three window sizes were tested: 60 x 60 pixel, 120 x 120 pixel, and 180 x 180 pixel.

The experimental results are analyzed from two viewpoints. In section 5.6.2, the plots and tables emphasize the effect of the window size by examining one ICP quantity at a time. In section 5.6.3, the plots and tables emphasize the effect of different ICP quantities by examining one window size at a time. The latter section is an extension of experiment 5, which only dealt with a single window size.

5.6.2 Results – Varying Window Sizes

In this section, the plots and tables emphasize the effect of the window size by examining one ICP quantity at a time. The SD metric is evaluated for each LS-SVR and polynomial run according to the procedure described in section 4.3.1. Table 14, Table 15, and Table 16 show the distance between paired PCP's and ICP's decreases more quickly when applying the LS-SVR transform model. For a given number of ICP's, there is a small, run-to-run variation in the mean value due to the LS-SVR parameter optimization as explained in section 5.1.3.

Table 14: Expt 6 results - sum of distances for PCP's + 5 ICP's. Distance between paired PCP's and ICP's decreases more quickly for the LS-SVR transform model.

Expt 6: Sum of Distances in Varying Windows for PCP's + 5 ICP's			
	LS-SVR	Poly	p-value
60x60 window	-0.1452	-0.0636	8.07 E-7
120x120 window	-0.1461	-0.0636	1.29 E-7
180x180 window	-0.1463	-0.0636	5.47 E-7

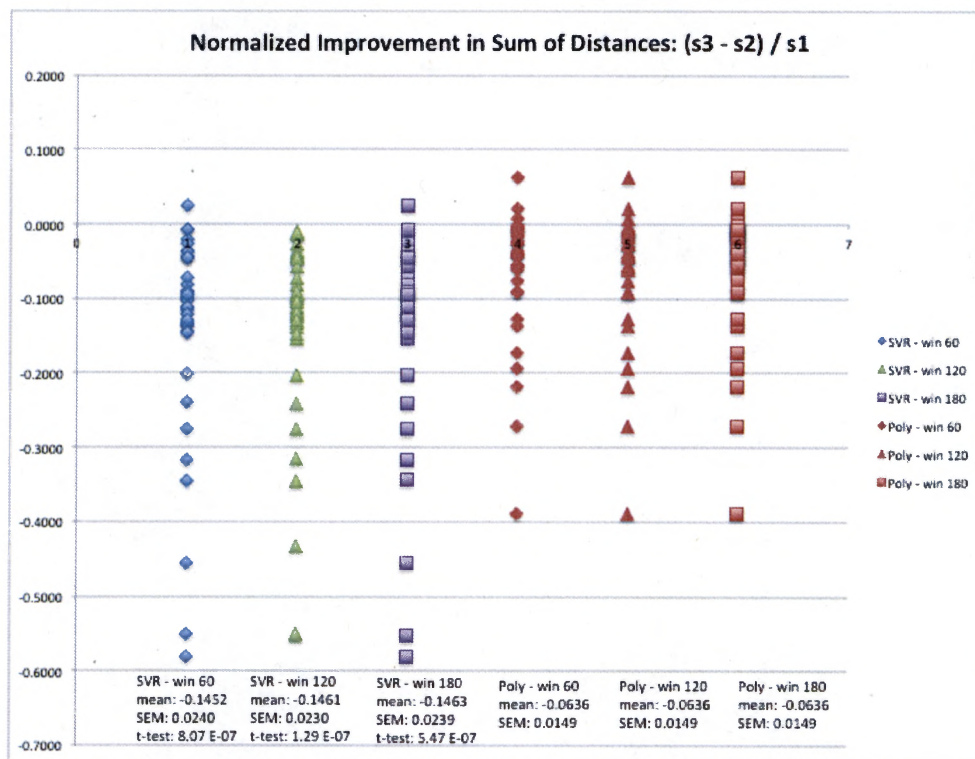


Figure 43: Expt 6 results - sum of distances for PCP's + 5 ICP's. Left three columns are the LS-SVR results, while the right three columns are the polynomial results. Each point is the result for a sub-image pair.

Table 15: Expt 6 results - sum of distances for PCP's + 10 ICP's. Distance between paired PCP's and ICP's decreases more quickly for the LS-SVR transform model.

Expt 6: Sum of Distances in Varying Windows for PCP's + 10 ICP's			
	LS-SVR	Poly	p-value
60x60 window	-0.1398	-0.0645	4.53 E-9
120x120 window	-0.1413	-0.0645	6.44 E-9
180x180 window	-0.1399	-0.0645	2.11 E-9

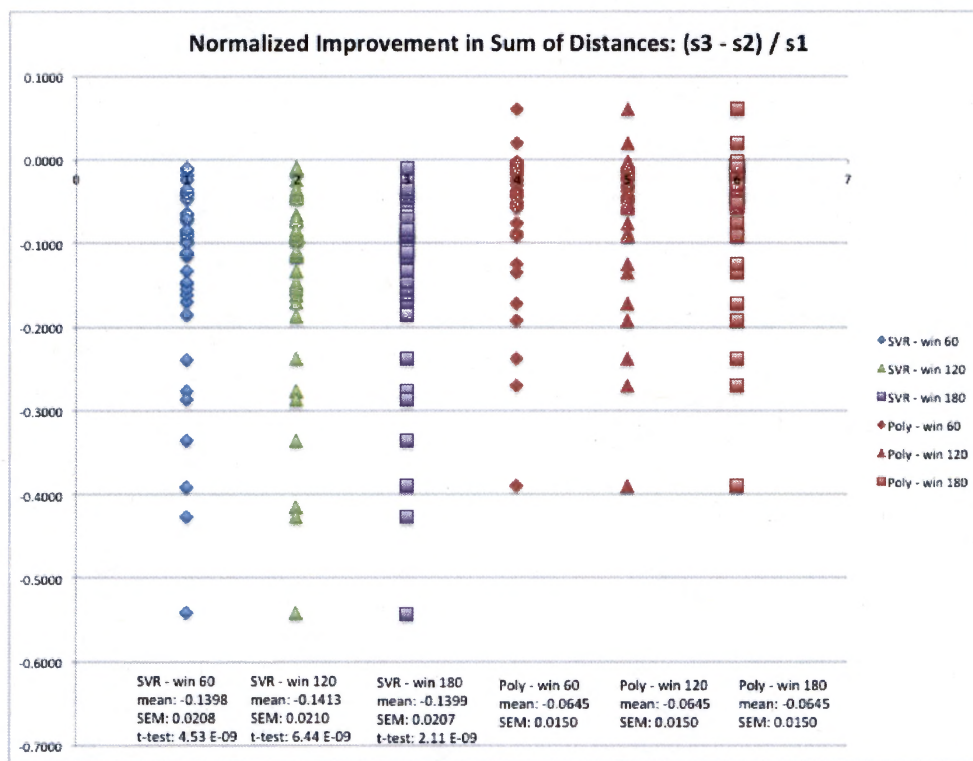


Figure 44: Expt 6 results - sum of distances for PCP's + 10 ICP's. Left three columns are the LS-SVR results, while the right three columns are the polynomial results. Each point is the result for a sub-image pair.

Table 16: Expt 6 results - sum of distances for PCP's + 15 ICP's. Distance between paired PCP's and ICP's decreases more quickly for the LS-SVR transform model.

Expt 6: Sum of Distances in Varying Windows for PCP's + 15 ICP's			
	LS-SVR	Poly	p-value
60x60 window	-0.1317	-0.0631	8.98 E-8
120x120 window	-0.1318	-0.0631	7.39 E-8
180x180 window	-0.1331	-0.0631	3.28 E-8

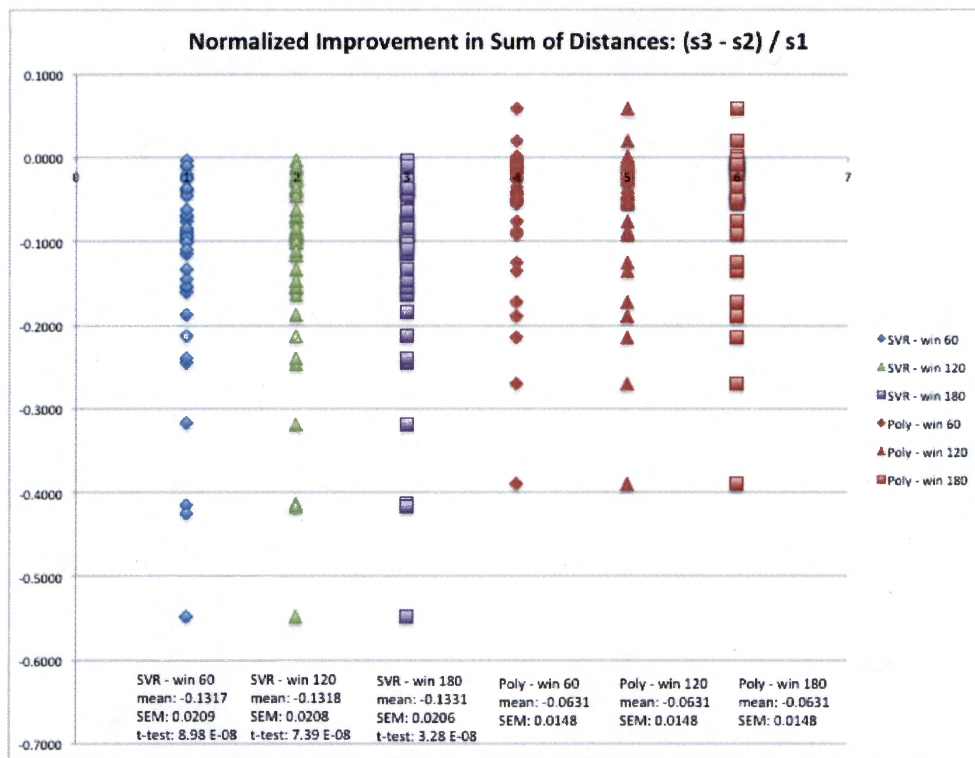


Figure 45: Expt 6 results - sum of distances for PCP's + 15 ICP's. Left three columns are the LS-SVR results, while the right three columns are the polynomial results. Each point is the result for a sub-image pair.

A graphical representation of the SD metric is shown in Figure 43, Figure 44, and Figure 45. The left three columns of points show the LS-SVR results, while the right three columns show the polynomial results. The distribution of the LS-SVR sub-image data is consistent from run-to-run.

The MI metric over the entire image is evaluated for each LS-SVR and polynomial run according to the procedure described in section 4.3.3. In all cases, the registration improved with the LS-SVR model, while the registration deteriorated with the polynomial model. However, the statistical significance varied. Table 17 shows that the difference between the two models is not significant for 5 ICP's. For 10 ICP's and 15 ICP's, Table 18 and Table 19 show the difference is significant at the lower threshold of $5.0 \text{ E-}2$.

A graphical representation of the registration improvement is shown in Figure 46, Figure 47, and Figure 48. The distribution of the LS-SVR sub-image data is consistent from run-to-run for a given number of ICP's. The distribution of the data for a given run becomes tighter with an increasing number of ICP's.

Table 17: Expt 6 results - mutual information over masked image for PCP's + 5 ICP's. MI decreases more quickly for the LS-SVR model, but improvement is not statistically significant.

Expt 6: Mutual Information Over Masked Image for PCP's + 5 ICP's			
	LS-SVR	Poly	p-value
60x60 window	-0.0002	0.0005	1.58 E-2
120x120 window	0.0000	0.0005	6.45 E-2
180x180 window	-0.0001	0.0005	3.37 E-2

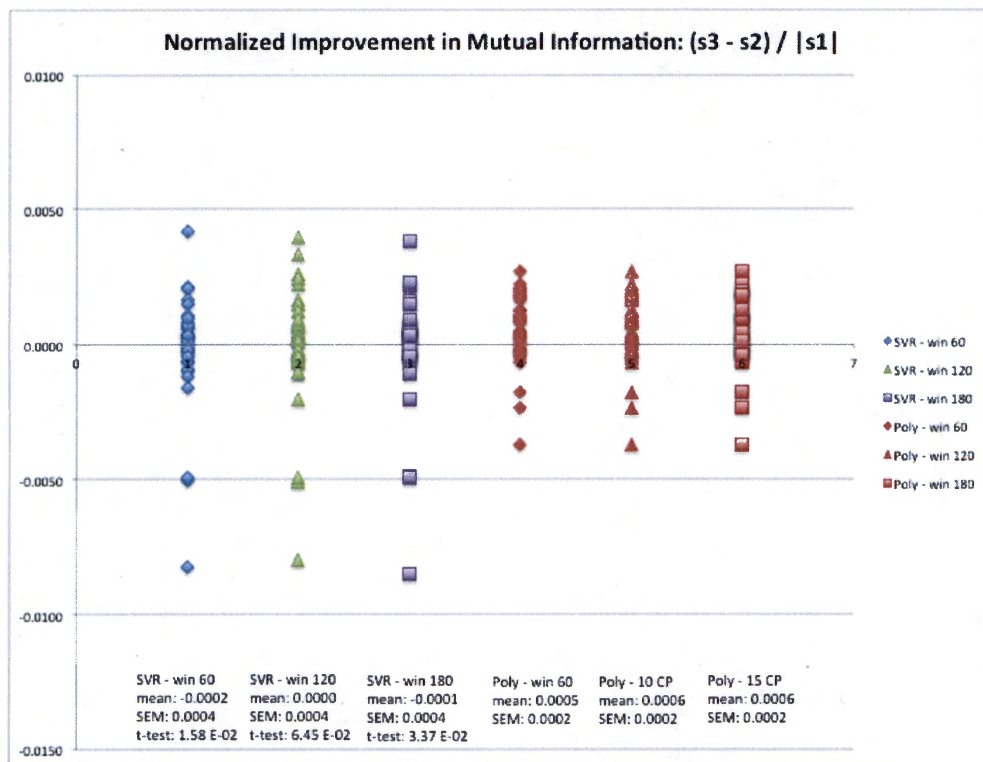


Figure 46: Expt 6 results - mutual information over masked image for PCP's + 5 ICP's. Left three columns are the LS-SVR results, while the right three columns are the polynomial results. Each point is the result for a sub-image pair.

Table 18: Expt 6 Results - mutual information over masked image for PCP's + 10 ICP's. MI decreases more quickly for the LS-SVR model, but improvement is not statistically significant at higher threshold.

Expt 6: Mutual Information Over Masked Image for PCP's + 10 ICP's			
	LS-SVR	Poly	p-value
60x60 window	-0.0003	0.0006	7.30 E-4
120x120 window	-0.0002	0.0006	2.37 E-3
180x180 window	-0.0001	0.0006	7.95 E-3

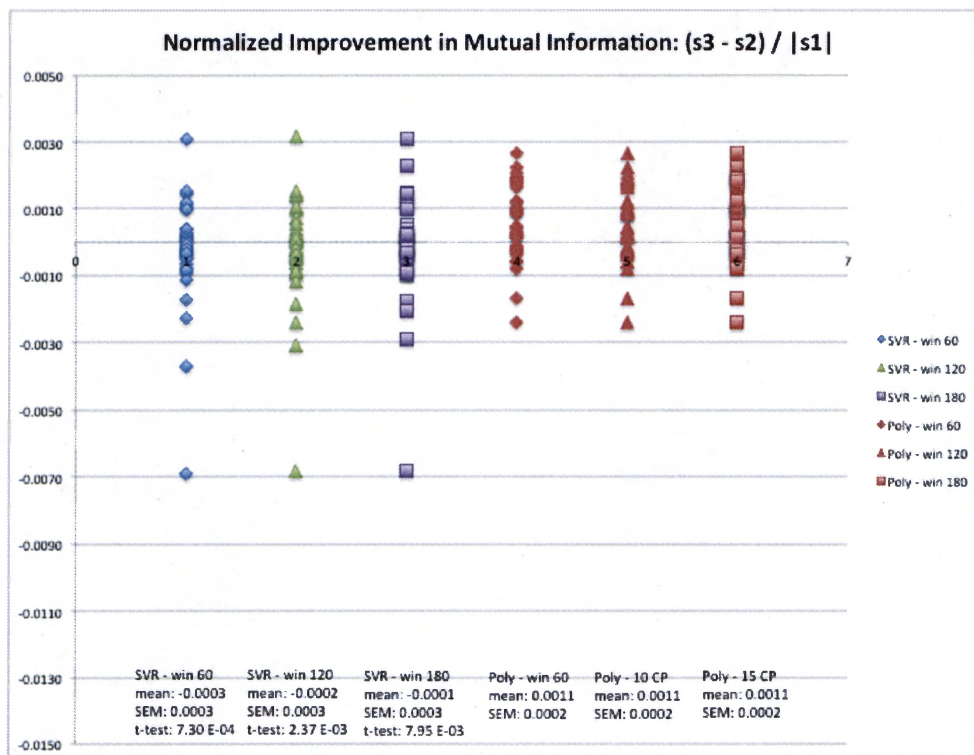


Figure 47: Expt 6 results - mutual information over masked image for PCP's + 10 ICP's. Left three columns are the LS-SVR results, while the right three columns are the polynomial results. Each point is the result for a sub-image pair.

Table 19: Expt 6 results - mutual information over masked image for PCP's + 15 ICP's. MI decreases more quickly for the LS-SVR model, but improvement is not statistically significant at higher threshold.

Expt 6: Mutual Information Over Masked Image for PCP's + 15 ICP's			
	LS-SVR	Poly	p-value
60x60 window	-0.0001	0.0006	2.32 E-3
120x120 window	-0.0001	0.0006	2.55 E-3
180x180 window	-0.0001	0.0006	1.91 E-3

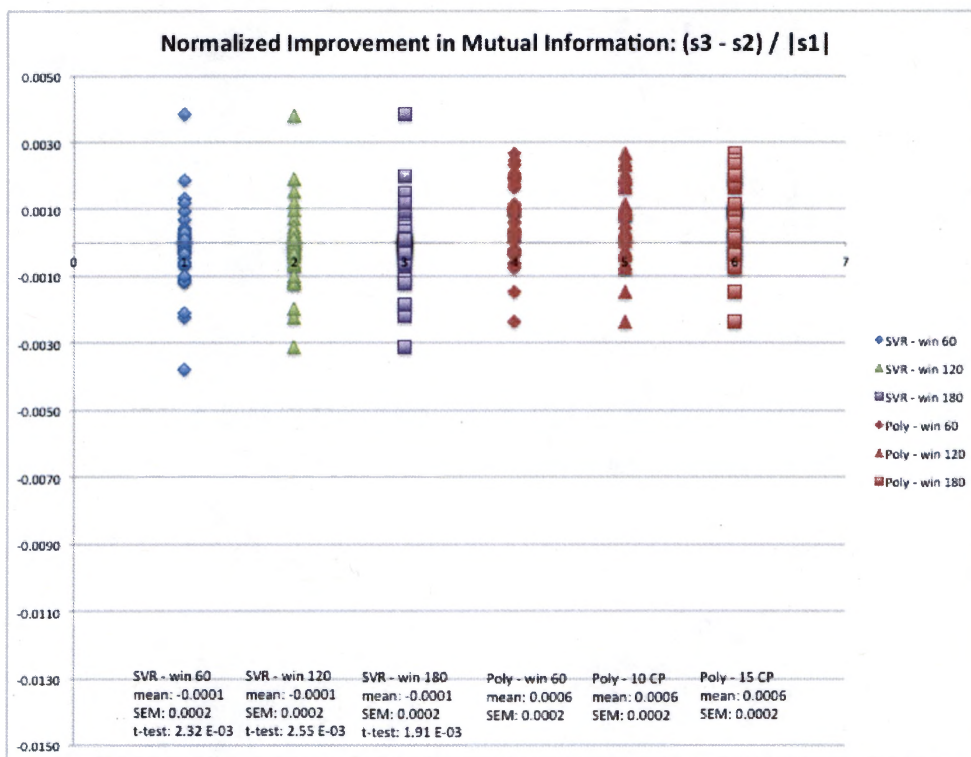


Figure 48: Expt 6 results - mutual information over masked image for PCP's + 15 ICP's. Left three columns are the LS-SVR results, while the right three columns are the polynomial results. Each point is the result for a sub-image pair.

Table 20: Expt 6 results - mutual information in varying windows around 5 ICP's. Window size has no effect on the LS-SVR window MI, while the polynomial window MI improves with larger window size.

Expt 6: Mutual Information in Varying Windows Around 5 ICP's				
	LS-SVR	Poly	LS-SVR - Poly	p-value
60x60 window	0.0013	0.0047	-0.0033	3.40 E-6
120x120 window	0.0015	0.0042	-0.0027	2.74 E-4
180x180 window	0.0013	0.0034	-0.0021	6.53 E-3

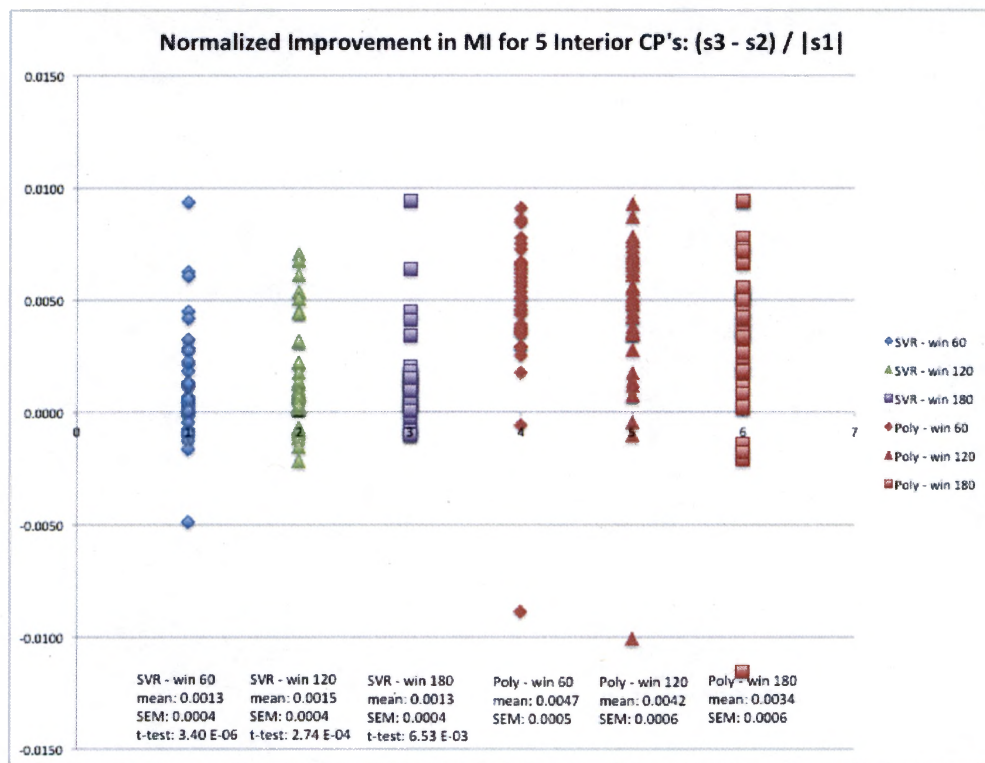


Figure 49: Expt 6 results - mutual information in varying windows around 5 ICP's. Left three columns are the LS-SVR results, while the right three columns are the polynomial results. Each point is the result for a sub-image pair.

Table 21: Expt 6 results - mutual information in varying windows around 10 ICP's. LS-SVR window MI deteriorates with increasing window size, while the polynomial window MI improves with larger window size.

Expt 6: Mutual Information in Varying Windows Around 10 ICP's				
	LS-SVR	Poly	LS-SVR – Poly	p-value
60x60 window	0.0003	0.0052	-0.0048	6.29 E-14
120x120 window	0.0009	0.0046	-0.0037	2.15 E-7
180x180 window	0.0011	0.0034	-0.0023	6.51 E-3

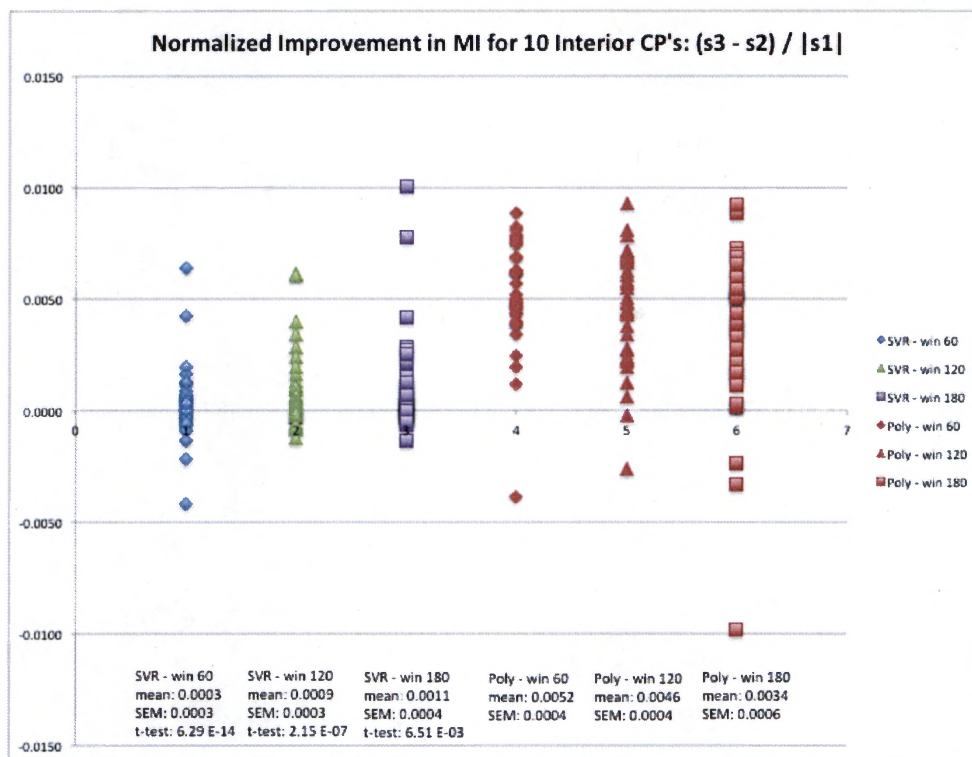


Figure 50: Expt 6 results - mutual information in varying windows around 10 ICP's. Left three columns are the LS-SVR results, while the right three columns are the polynomial results. Each point is the result for a sub-image pair.

Table 22: Expt 6 results - mutual information in varying windows around 15 ICP's. LS-SVR window MI deteriorates with increasing window size, while the polynomial window MI improves with larger window size.

Expt 6: Mutual Information in Windows Varying Around 15 ICP's				
	LS-SVR	Poly	LS-SVR - Poly	p-value
60x60 window	-0.0003	0.0047	-0.0050	2.27 E-12
120x120 window	0.0006	0.0050	-0.0044	4.04 E-9
180x180 window	0.0008	0.0037	-0.0029	8.38 E-4

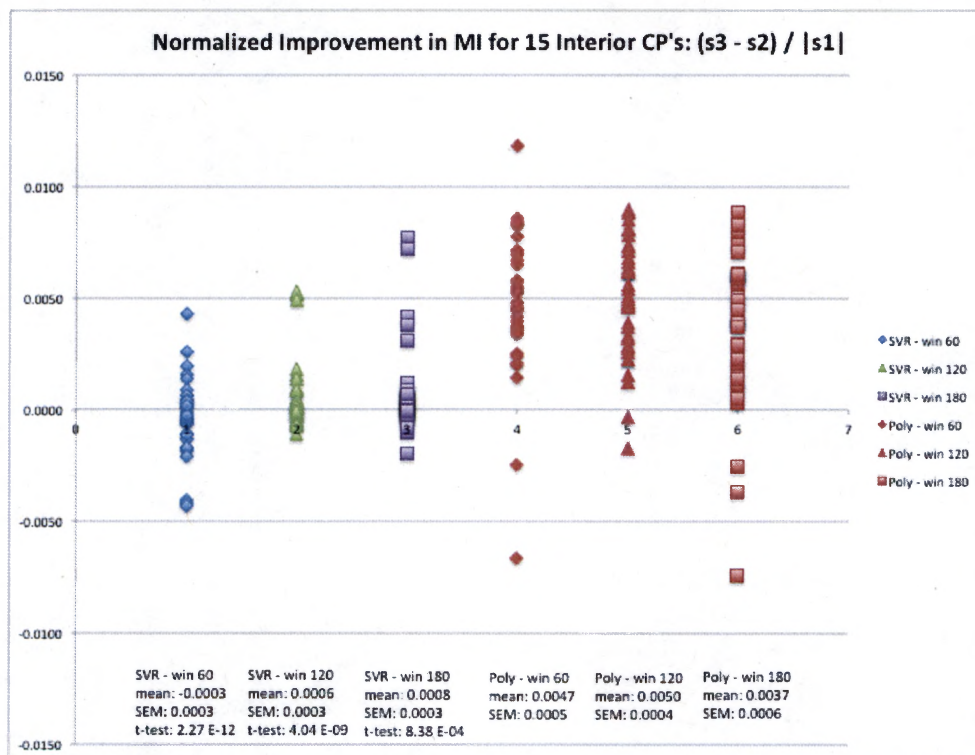


Figure 51: Expt 6 results - mutual information in varying windows around 15 ICP's. Left three columns are the LS-SVR results, while the right three columns are the polynomial results. Each point is the result for a sub-image pair.

The window MI metrics over three different window sizes are evaluated for each LS-SVR and polynomial run according to the procedure described in section 4.3.4. Table 20, Table 21, and Table 22 show that the LS-SVR transform outperforms the polynomial transform irrespective of the window size or number of ICP's. For any number of ICP's, the polynomial window MI improves with larger window size. For five ICP's, the LS-SVR window MI is stable with respect to window size. For ten and fifteen ICP's, the LS-SVR window MI deteriorates with increasing window size.

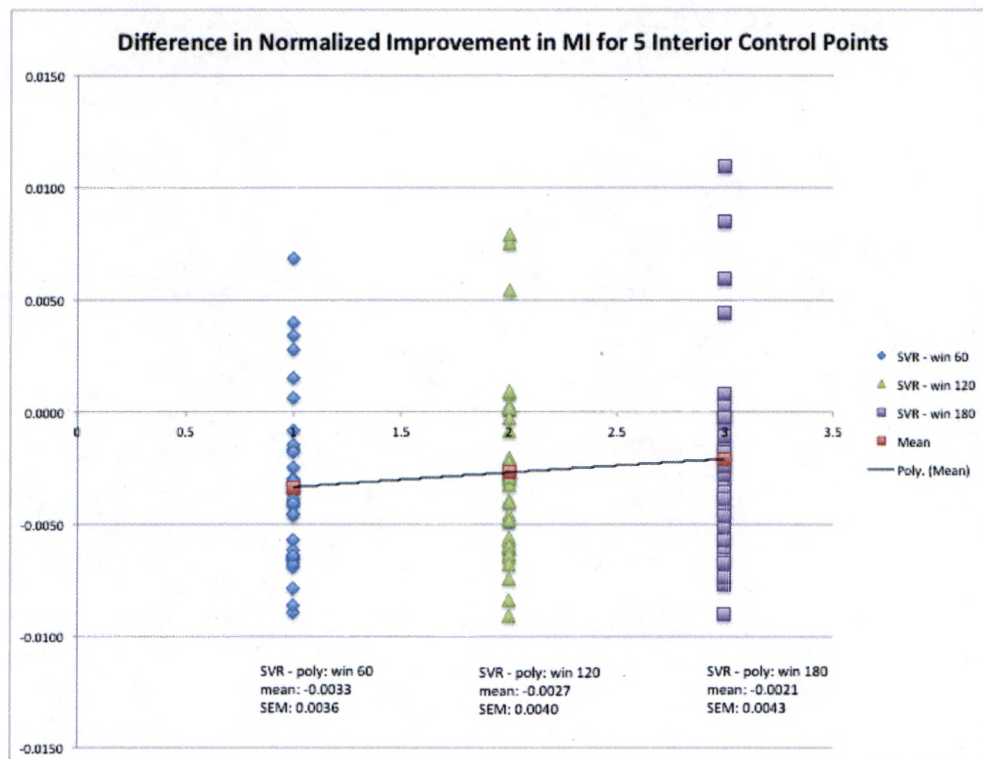


Figure 52: Expt 6 results - MI difference in varying windows around 5 ICP's. The MI difference deteriorates with additional ICP's.

Graphical representations of the window MI are shown in Figure 49, Figure 50, and Figure 51. The distribution of the LS-SVR sub-image data is constant irrespective of the window size or number of ICP's. The difference between the two models can be visualized by subtracting the polynomial result from the LS-SVR result for each sub-image pair as shown in Figure 52, Figure 53, and Figure 54. The difference between the two models grows smaller with increasing window size.

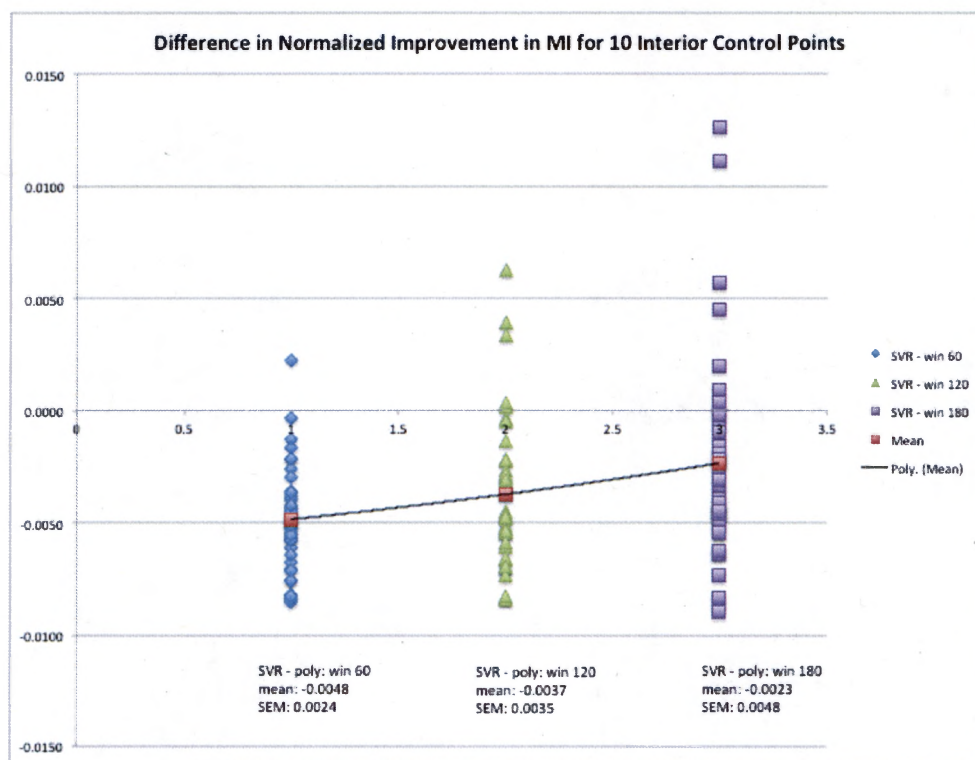


Figure 53: Expt 6 results - MI difference in varying windows around 10 ICP's. The MI difference deteriorates with additional ICP's.

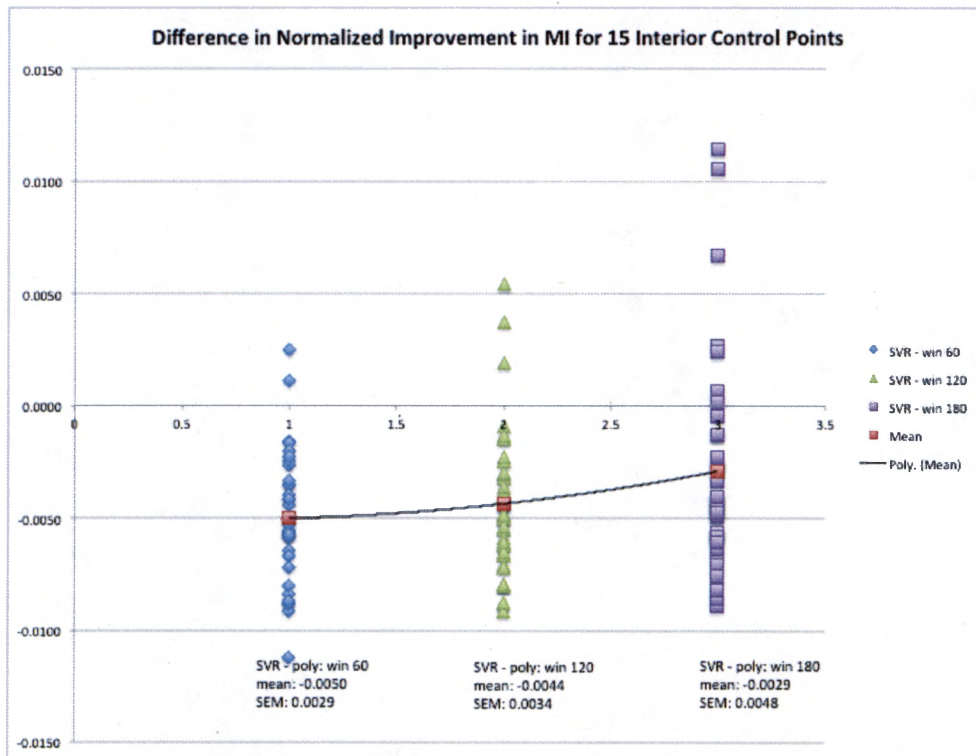


Figure 54: Expt 6 results - MI difference in varying windows around 15 ICP's. The MI difference deteriorates with additional ICP's.

5.6.3 Results – Varying Number of Interior Control Points

In this section, the plots and tables emphasize the effect of different ICP quantities by examining one window size at a time. The SD metric is evaluated for each LS-SVR and polynomial run according to the procedure described in section 4.3.1. Table 23, Table 24, and Table 25 show the distance between paired PCP's and ICP's decreases more quickly when applying the LS-SVR transform model. As the number of ICP's increases, the SD metric becomes worse by increasing in value.

A graphical representation of the SD metric is shown in Figure 55, Figure 56, and Figure 57. The left three columns of points show the LS-SVR results, while the right three columns show the polynomial results. The distribution of the LS-SVR sub-image data is slightly wider for five ICP's.

The MI metric over the entire image is evaluated for each LS-SVR and polynomial run according to the procedure described in section 4.3.3. In all cases, the registration stayed the same or improved slightly with the LS-SVR model, while the registration deteriorated with the polynomial model. Table 26, Table 27, and Table 28 show the difference between the two models is significant at the lower threshold of $5.0 \text{ E-}2$, but not the higher threshold of $1.0 \text{ E-}3$.

A graphical representation of the registration improvement is shown in Figure 58, Figure 59, and Figure 60. The distribution of the LS-SVR sub-image data becomes tighter with an increasing number of ICP's. However, there is virtually no improvement in the overall registration across the dataset.

Table 23: Expt 6 results - sum of distances for PCP's + varying ICP's (60x60 window). Distance between paired PCP's and ICP's increases with additional ICP's.

Expt 6: Sum of Distances for PCP's + Varying ICP's (60x60 window)			
	LS-SVR	Poly	p-value
Perimeter + 5 Interior CP's	-0.1452	-0.0636	8.07 E-7
Perimeter + 10 Interior CP's	-0.1398	-0.0645	4.53 E-9
Perimeter + 15 Interior CP's	-0.1317	-0.0631	8.98 E-8

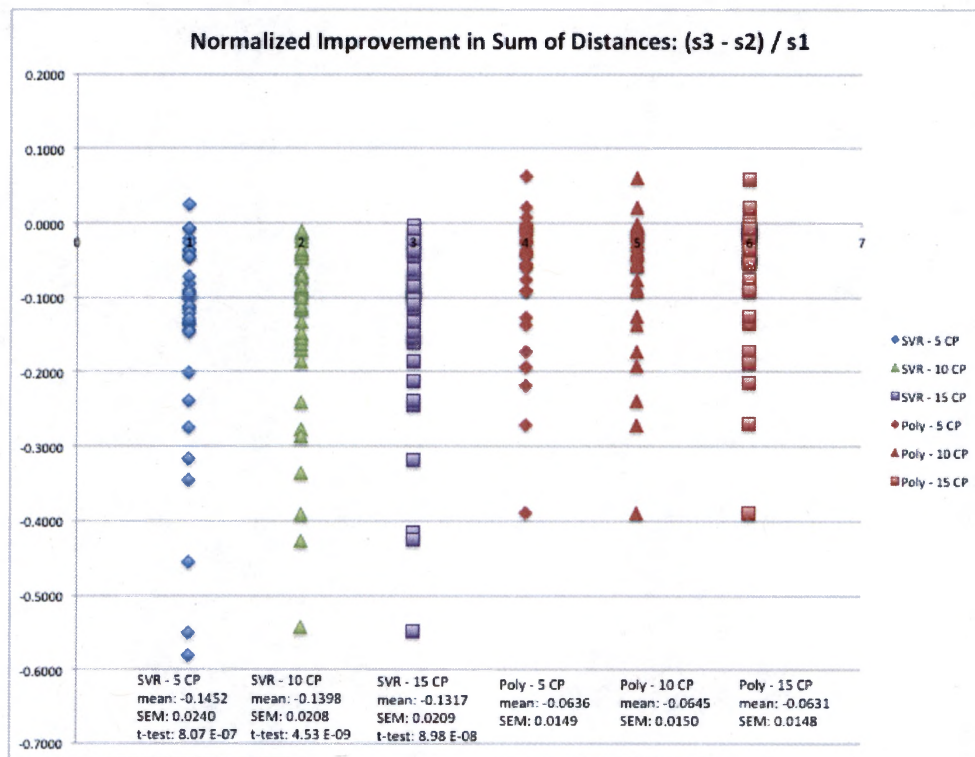


Figure 55: Expt 6 results - sum of distances for PCP's + varying ICP's (60x60 window). Left three columns are the LS-SVR results, while the right three columns are the polynomial results. Each point is the result for a sub-image pair.

Table 24: Expt 6 results - sum of distances for PCP's + varying ICP's (120x120 window). Distance between paired PCP's and ICP's increases with additional ICP's.

Expt 6: Sum of Distances for PCP's + Varying ICP's (120x120 window)			
	SVR	Poly	p-value
Perimeter + 5 Interior CP's	-0.1461	-0.0636	1.29 E-7
Perimeter + 10 Interior CP's	-0.1413	-0.0645	6.44 E-9
Perimeter + 15 Interior CP's	-0.1318	-0.0631	7.39 E-8

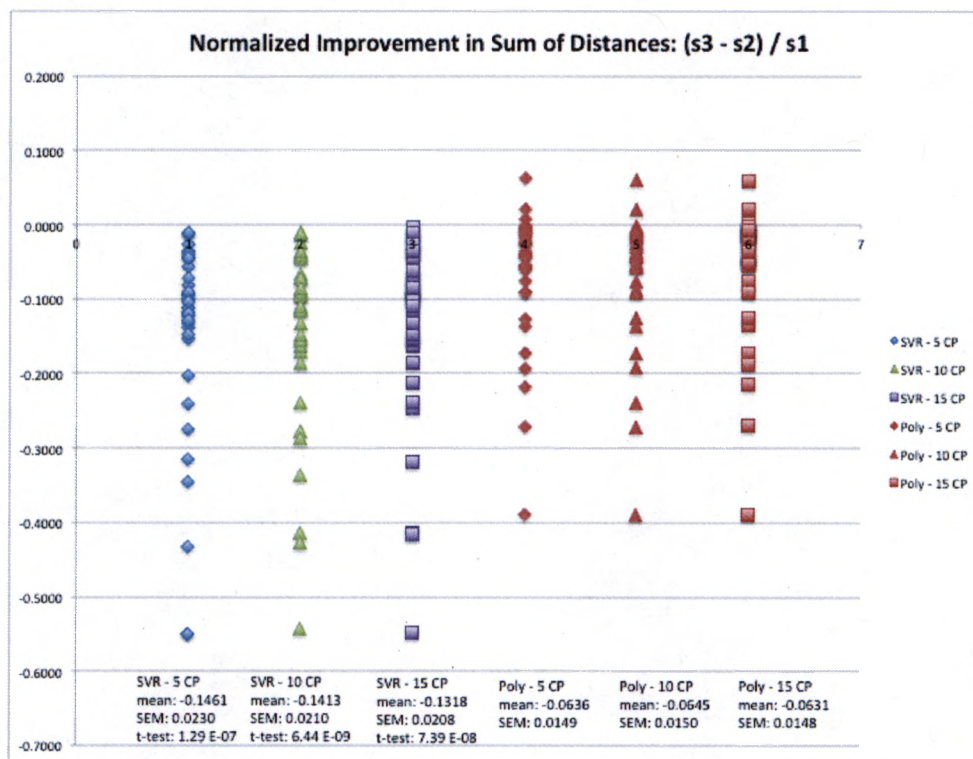


Figure 56: Expt 6 results - sum of distances for PCP's + varying ICP's (120x120 window). Left three columns are the LS-SVR results, while the right three columns are the polynomial results. Each point is the result for a sub-image pair.

Table 25: Expt 6 results - sum of distances for PCP's + varying ICP's (180x180 window). Distance between paired PCP's and ICP's increases with additional ICP's.

Expt 6: Sum of Distances for PCP's + Varying ICP's (180x180 window)			
	SVR	Poly	p-value
Perimeter + 5 Interior CP's	-0.1463	-0.0636	5.47 E-7
Perimeter + 10 Interior CP's	-0.1399	-0.0645	2.11 E-9
Perimeter + 15 Interior CP's	-0.1331	-0.0631	3.28 E-8

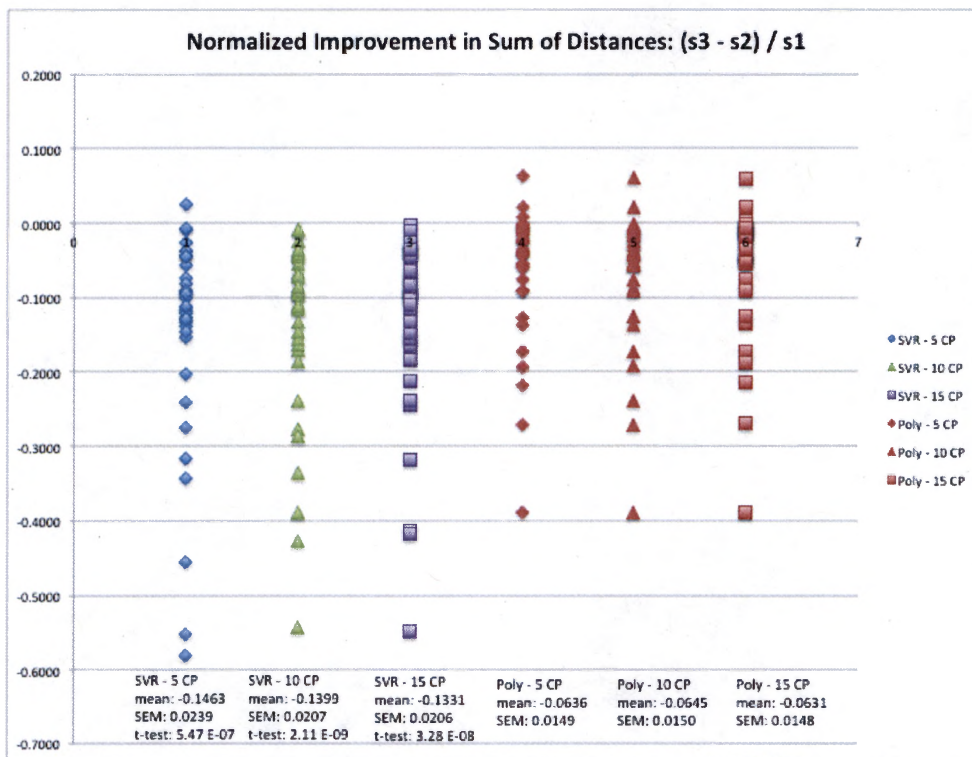


Figure 57: Expt 6 results - sum of distances for PCP's + varying ICP's (180x180 window). Left three columns are the LS-SVR results, while the right three columns are the polynomial results. Each point is the result for a sub-image pair.

Table 26: Expt 6 results - MI over masked image for PCP's + varying ICP's (60x60 window). MI decreases more quickly for the LS-SVR model, but improvement is not statistically significant at higher threshold.

Expt 6: MI Over Masked Image for PCP's + Varying ICP's (60x60 window)			
	SVR	Poly	p-value
Perimeter + 5 Interior CP's	-0.0002	0.0005	1.58 E-2
Perimeter + 10 Interior CP's	-0.0003	0.0006	7.30 E-4
Perimeter + 15 Interior CP's	-0.0001	0.0006	2.32 E-3

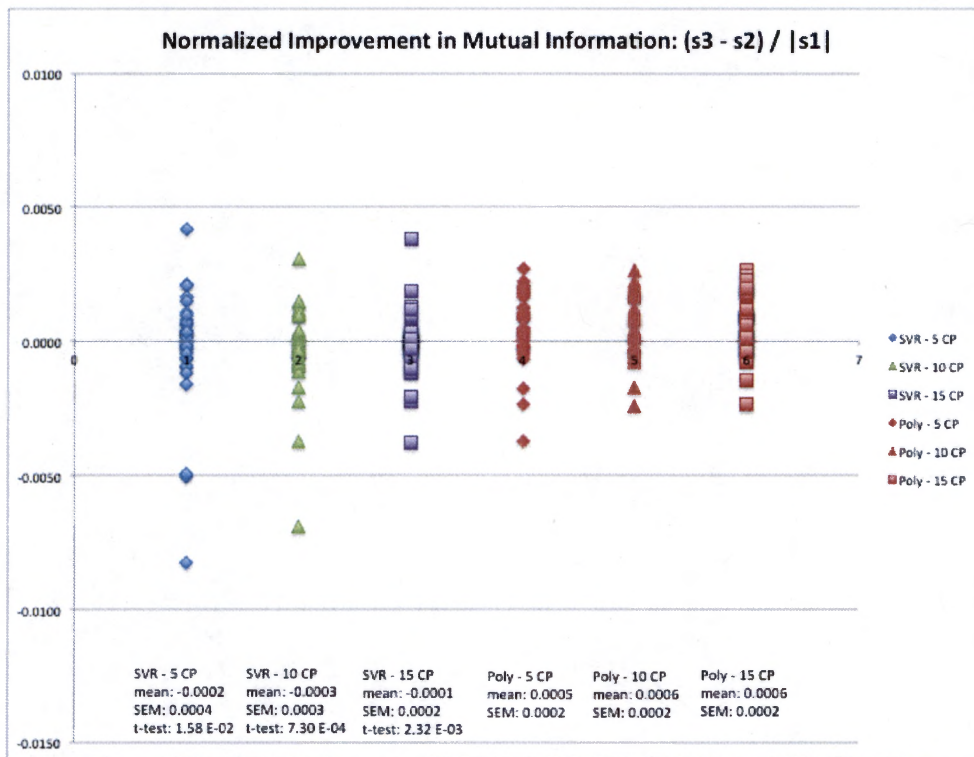


Figure 58: Expt 6 results - MI over masked image for PCP's + varying ICP's (60x60 window). Left three columns are the LS-SVR results, while the right three columns are the polynomial results. Each point is the result for a sub-image pair.

Table 27: Expt 6 results - MI over masked image for PCP's + varying ICP's (120x120 window). MI decreases more quickly for the LS-SVR model, but improvement is not statistically significant at higher threshold.

Expt 6: MI Over Masked Image for PCP's + Varying ICP's (120x120 window)			
	SVR	Poly	p-value
Perimeter + 5 Interior CP's	0.0000	0.0005	6.45 E-2
Perimeter + 10 Interior CP's	-0.0002	0.0006	2.37 E-3
Perimeter + 15 Interior CP's	-0.0001	0.0006	2.55 E-3

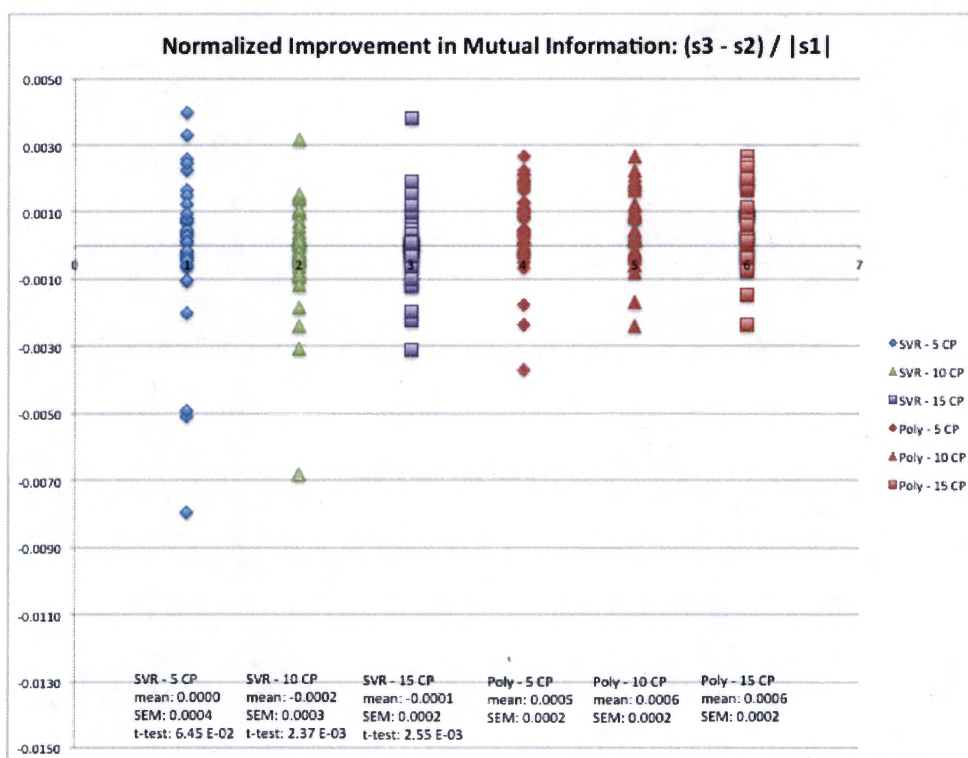


Figure 59: Expt 6 results - MI over masked image for PCP's + varying ICP's (120x120 window). Left three columns are the LS-SVR results, while the right three columns are the polynomial results. Each point is the result for a sub-image pair.

Table 28: Expt 6 results - MI over masked image for PCP's + varying ICP's (180x180 window). MI decreases more quickly for the LS-SVR model, but improvement is not statistically significant at higher threshold.

Expt 6: MI Over Masked Image for PCP's + Varying ICP's (180x180 window)			
	SVR	Poly	p-value
Perimeter + 5 Interior CP's	-0.0001	0.0005	3.37 E-2
Perimeter + 10 Interior CP's	-0.0001	0.0006	7.59 E-3
Perimeter + 15 Interior CP's	-0.0001	0.0006	1.91 E-3

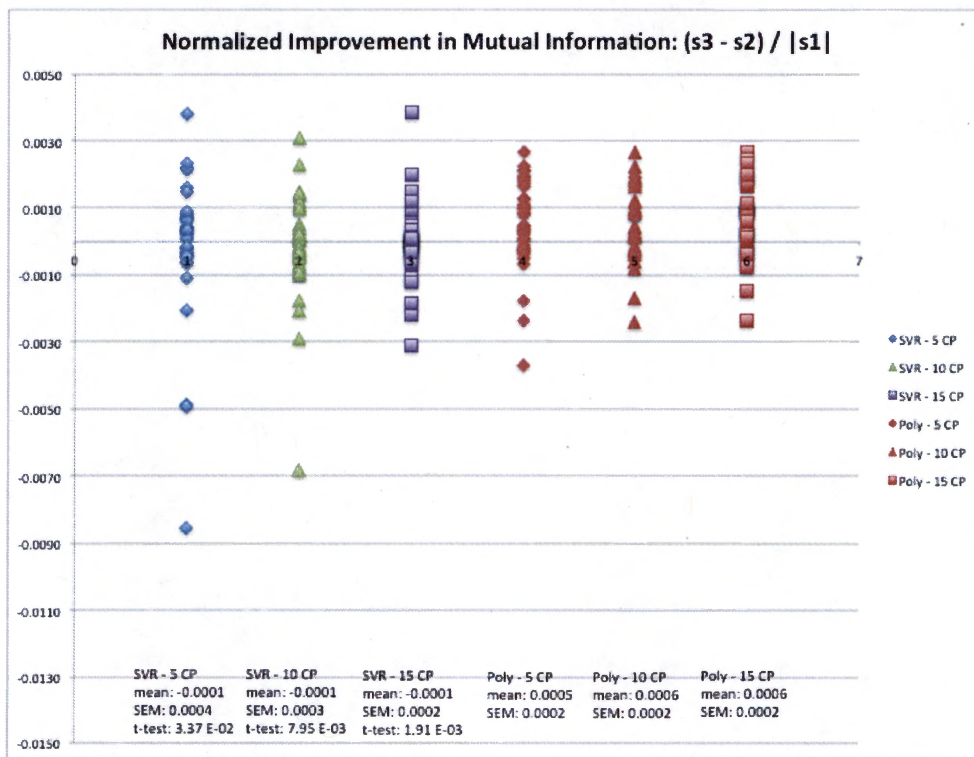


Figure 60: Expt 6 results - MI over masked image for PCP's + varying ICP's (180x180 window). Left three columns are the LS-SVR results, while the right three columns are the polynomial results. Each point is the result for a sub-image pair.

Table 29: Expt 6 results - mutual information in 60x60 windows around varying ICP's. LS-SVR window MI improves with increasing number of ICP's.

Expt 6: Mutual Information in 60x60 Windows Around Varying ICP's				
	SVR	Poly	SVR - Poly	p-value
Perimeter + 5 Interior CP's	0.0013	0.0047	-0.0033	3.40 E-6
Perimeter + 10 Interior CP's	0.0003	0.0052	-0.0048	6.29 E-14
Perimeter + 15 Interior CP's	-0.0003	0.0047	-0.0050	2.27 E-12

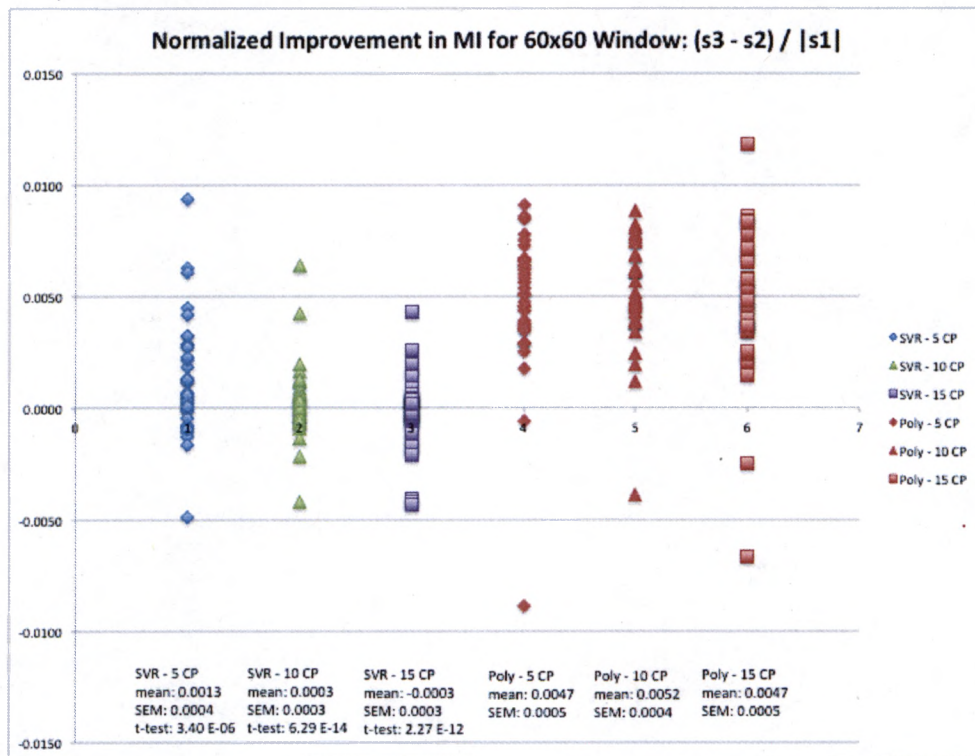


Figure 61: Expt 6 results - MI in 60x60 windows around varying ICP's. Left three columns are the LS-SVR results, while the right three columns are the polynomial results. Each point is the result for a sub-image pair.

Table 30: Expt 6 results - mutual information in 120x120 windows around varying ICP's. LS-SVR window MI improves with increasing number of ICP's.

Expt 6: Mutual Information in 120x120 Windows Varying ICP's				
	SVR	Poly	SVR - Poly	p-value
Perimeter + 5 Interior CP's	0.0015	0.0042	-0.0027	2.74 E-4
Perimeter + 10 Interior CP's	0.0009	0.0046	-0.0037	2.15 E-7
Perimeter + 15 Interior CP's	0.0006	0.0050	-0.0044	4.04 E-9

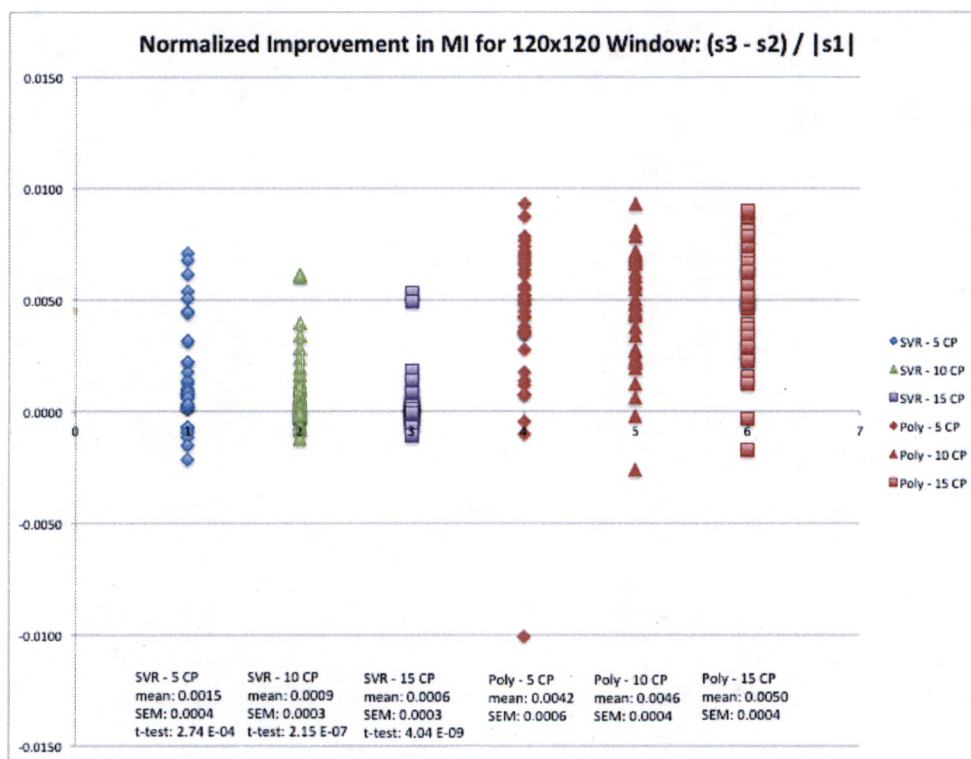


Figure 62: Expt 6 results - MI in 120x120 windows around varying ICP's. Left three columns are the LS-SVR results, while the right three columns are the polynomial results. Each point is the result for a sub-image pair.

Table 31: Expt 6 results - mutual information in 180x180 windows around varying ICP's. LS-SVR window MI improves with increasing number of ICP's.

Expt 6: Mutual Information in 180x180 Windows Around Varying ICP's				
	SVR	Poly	SVR - Poly	p-value
Perimeter + 5 Interior CP's	0.0013	0.0034	-0.0021	6.53 E-3
Perimeter + 10 Interior CP's	0.0011	0.0034	-0.0023	6.51 E-3
Perimeter + 15 Interior CP's	0.0008	0.0037	-0.0029	8.38 E-4

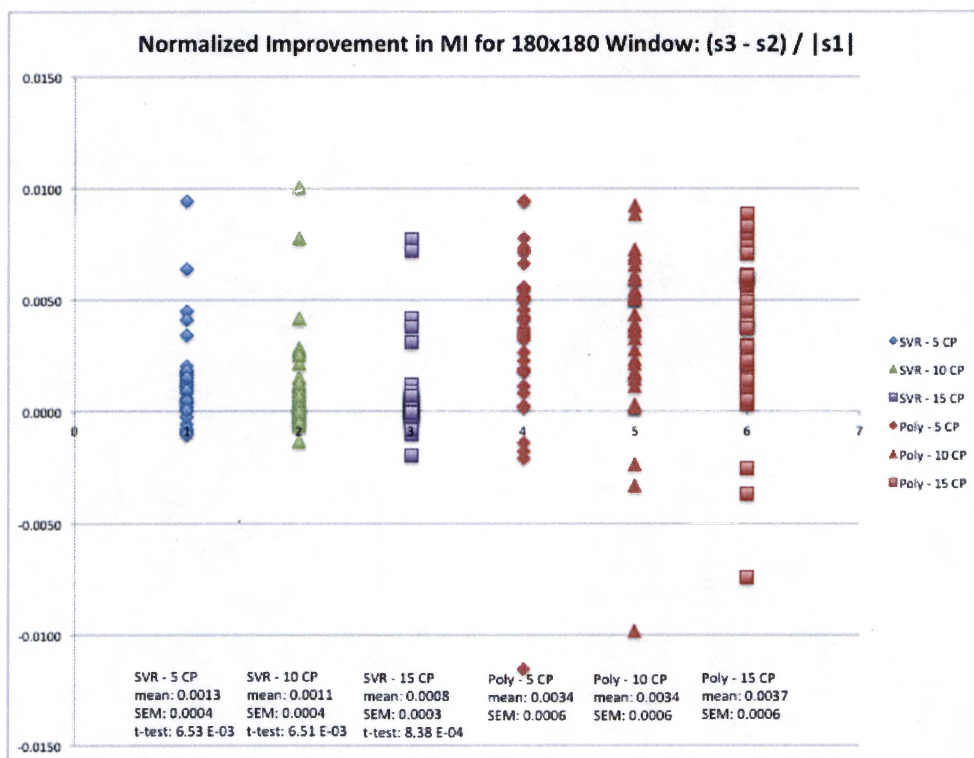


Figure 63: Expt 6 results - MI in 180x180 windows around varying ICP's. Left three columns are the LS-SVR results, while the right three columns are the polynomial results. Each point is the result for a sub-image pair.

The window MI metrics for three different numbers of ICP's are evaluated for each LS-SVR and polynomial run according to the procedure described in section 4.3.4. Table 29, Table 30, and Table 31 show that the polynomial window MI stays about the same or gets slightly worse with increasing number of ICP's. In contrast, the LS-SVR window MI improves with increasing number of ICP's.

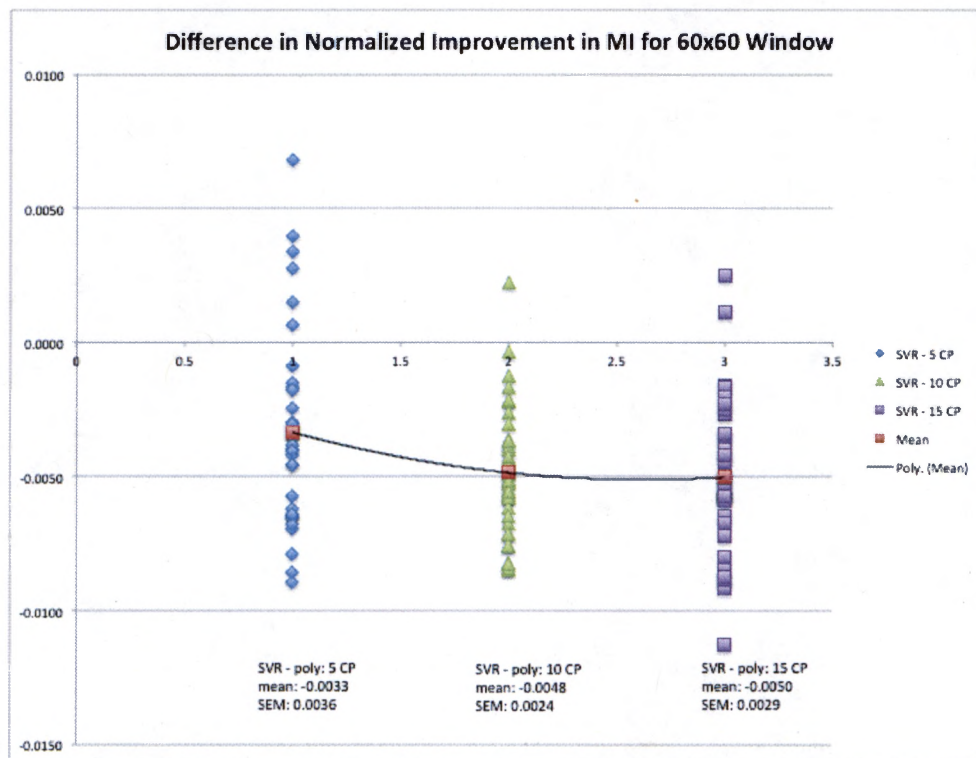


Figure 64: Expt 6 results – MI difference in 60x60 windows around varying ICP's. The MI difference improves with additional ICP's.

Graphical representations of the window MI are shown in Figure 61, Figure 62, and Figure 63. The difference between the two models can be visualized by subtracting the polynomial result from the LS-SVR result for each sub-image pair as shown in Figure 64, Figure 65, and Figure 66. The difference between the two models grows larger with an increasing number of ICP's.

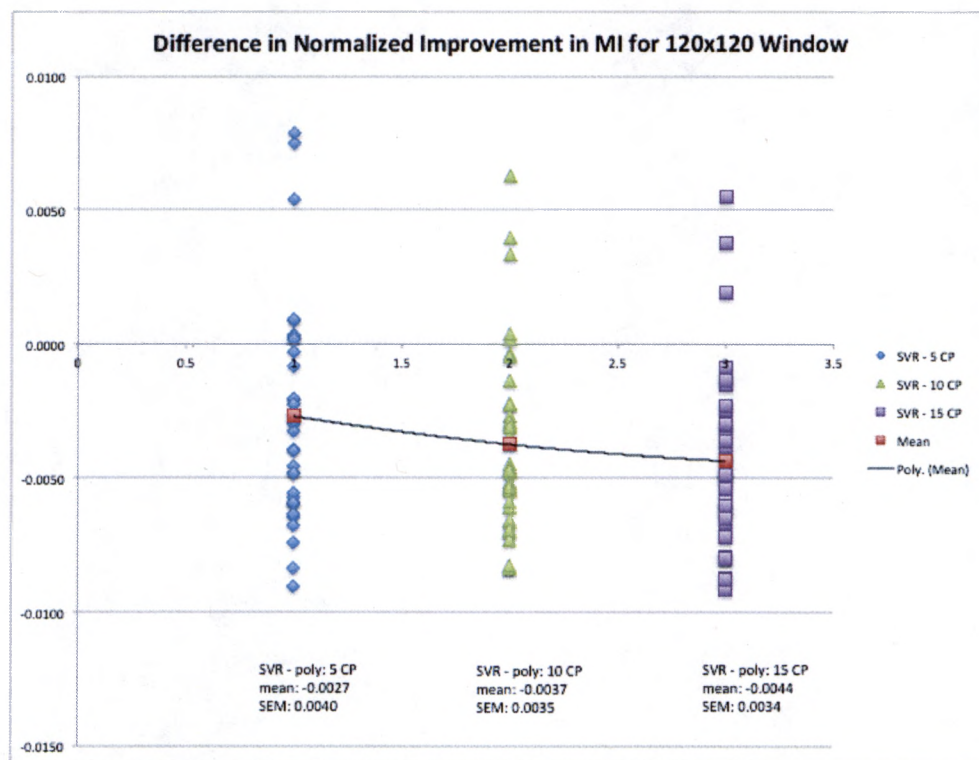


Figure 65: Expt 6 results – MI difference in 120x120 windows around varying ICP's. The MI difference improves with additional ICP's.

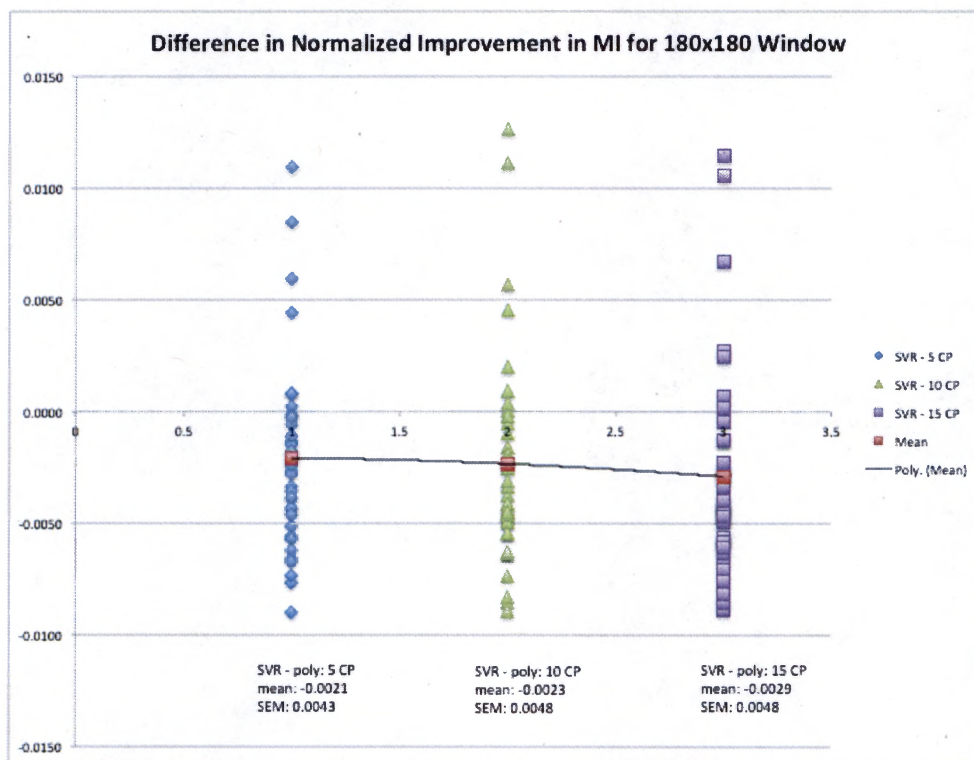


Figure 66: Expt 6 results – MI difference in 180x180 windows around varying ICP's. The MI difference improves with additional ICP's.

5.6.4 Discussion

This experiment quantifies the effect of the LS-SVR transform in the neighborhood around each ICP. The transform is expected to be most accurate near the control point with decreasing accuracy and influence when moving away from the control point. The area of accurate transform will shed light on the number of ICP's required to improve the non-linear registration.

The SD metric, M_{SD} , essentially remains the same regardless of the window size. This makes sense, because the window size has no impact on this metric. The runs for each window size act as a repeatability test for this metric. M_{SD} becomes less negative as the number of ICP's is increased. This trend suggests that the model overfits the PCP's. As the number of ICP's increases, the registration accuracy over the entire image improves at the expense of the PCP registration accuracy.

The MI over the entire image, M_{MI_img} , is another metric that does not change with window size. The runs for each window size act as a repeatability test for this metric, so it may be possible to pool these results to improve the p-values. The negative value of M_{MI_img} signifies improving registration accuracy. It does not appreciably change with the number of ICP's. As mentioned in section 5.5.3, the large perimeter area is believed to have a negative M_{MI} , which drowns out the positive M_{MI} of the small areas near the ICP's.

The window MI, M_{MI_win} , becomes more positive with increasing window size, which signifies decreasing accuracy. The effect is illustrated in Figure 67. The x-axis depicts the ICP in the center with tick marks showing the width of the three window sizes. The inverted, dashed parabola represents the influence of the model. The model has the most influence near the control point. The blue parabola represents the accuracy of the model. When the blue parabola is below the zero of the y-axis, the MI is negative, which means the registration is improving. The model is more accurate near the control point. The colored area represents the window MI. When the green area exceeds the red area,

M_{MI_win} is negative valued, which signifies improving registration accuracy. Conversely, when the red area exceeds the green area, the M_{MI_win} is positive valued, which signifies deteriorating registration accuracy. Moving from left to right in Figure 67, the red area increases as the window size increases.

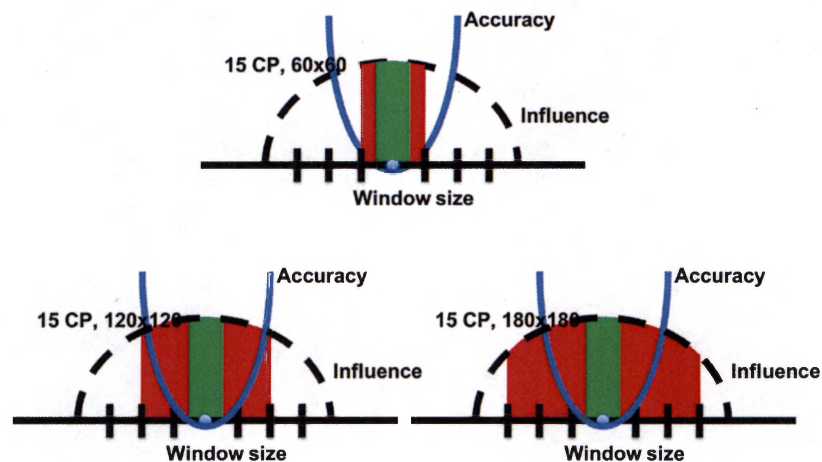


Figure 67: Mechanism for change in window MI as function of window size for a fixed number of ICP's. The drawings from top to left to right are the 60x60, 120x120 and 180x180 windows. Green marks where the window MI is negative. Red marks where the window MI is positive. The dashed line simulates the decay of the model influence based on the RBF kernel. The solid line simulates the model accuracy.

The window MI, M_{MI_win} , becomes more negative with increasing numbers of ICP's, which signifies increasing accuracy. The effect is illustrated in Figure 68. The blue parabola represents the accuracy of the model. When the blue parabola is below the zero of the y-axis, the MI is negative, which means the registration is improving. As the number of ICP's increases, the blue parabola is shifted downward. This shift increases the amount of green area relative to the red area at any window size. When the green area exceeds the red area, M_{MI_win} is negative valued, which signifies improving

registration accuracy. Conversely, when the red area exceeds the green area, M_{MI_win} is positive valued, which signifies deteriorating registration accuracy. Moving from left to right in Figure 68, the green area increases as the number of ICP's increases.

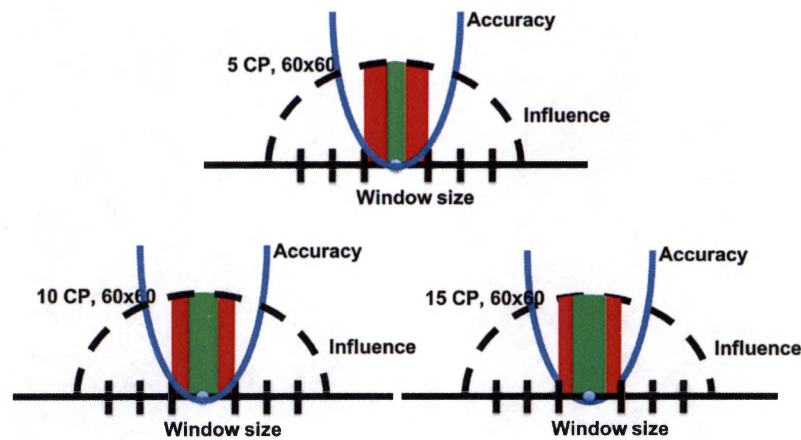


Figure 68: Mechanism for change in window MI as function of number of ICP's for a fixed window size. The drawings from top to left to right are 5, 10 and 15 ICP's. Green marks where the window MI is negative. Red marks where the window MI is positive. The dashed line simulates the decay of the model influence based on the RBF kernel. The solid line simulates the model accuracy.

The relative difference in M_{MI_win} (LS-SVR – Poly) becomes more positive with increasing window size. This trend is present for all three quantities of ICP's. In contrast, the relative difference in M_{MI_win} becomes more negative with increasing ICP's at all three window sizes. This trend suggests that continuing to add ICP's will improve the performance of the LS-SVR transform.

6 CONCLUSION

6.1 Summary of Results

The results of this study demonstrated that least-squares support vector regression, a machine learning technique, performs non-linear registration of histological images better than a second order polynomial transform when perimeter control points are augmented with a sufficient number of interior control points. The improvement in both local and global registration is statistically significant at a threshold of 5.00×10^{-2} .

6.2 Future Work

There are a variety of approaches to expand this study. The simplest approach is to substitute full-size images for the sub-images. The additional perimeter from the larger tissue area will result in more PCP's relative to ICP's, which should weight the model more heavily toward the perimeter. The ICP's will also be more sparsely distributed. Both of these reasons should in deterioration of the MI over the image and the window MI. One benefit from the increased tissue area is the presence of more matching features with which to manually generate additional ICP's.

The approach of adding more ICP's is supported by the results from section 5.6.3. However, it is difficult to manually locate enough matching features to create a sufficient number of ICP's. Automatic generation of ICP's requires enhancing the feature detection beyond the Harris corner detector. It may be possible to use deep learning methods to train a feature detector. A different approach is to automatically generate ICP's from the

mid-point coordinates between any two manually chosen ICP's. These matched pairs are artificial in the sense that the tissue at these coordinates probably does not have any distinguishing feature with which to match.

Different stain combinations are another area for investigation. The counterstain can behave differently as described in section 3.1, resulting in feature variation. Different tissue types can also be expected to have different quantities of available features. The quantity and distribution of features will impact the ability of the LS-SVR transform to register images.

Another avenue of investigation is the impact of non-consecutive tissue samples. In section 1.2, successive slices are anatomically different. This difference gets worse as the samples are located farther apart in the block of tissue. It may not be possible to match control points. However, the lack of control points for constraint leads to a bad transformation as shown in section 5.2.2.2. The LS-SVR algorithm used in this study needs a better method of regularization to prevent large distortions, and a method of avoiding transformation in areas where part of the tissue is present in one of the two images. One possibility is to convert the non-linear transform in stage 3 from the current open-loop, single-shot method to a closed-loop, multi-pass optimization that has a limited transformation step size.

Another approach is to compare the LS-SVR transform with alternatives to the polynomial transform. A preliminary attempt was made to replace the polynomial transform with a bspline transform by accessing the ITK libraries through a Matlab

interface.[27] Comparison with the demon registration algorithm can also be performed through the same interface.

Finally, LS-SVR is just one of the machine learning techniques that has been applied to image registration. The framework developed in this investigation can be applied to study other techniques such random forests, neural networks, and evolutionary algorithms.[15] [12] [7]

7 REFERENCE LIST

- [1] Auer, M., Regitnig, P., & Holzapfel, G. A. (2005). An automatic nonrigid registration for stained histological sections. *Image Processing, IEEE Transactions on*, 14(4), 475-486.
- [2] Bağci, U., & Bai, L. (2008). Registration of standardized histological images in feature space. In *Proc. of SPIE Vol (Vol. 6914, pp. 69142V-1)*
- [3] Borovec, J., Kybic, J., Bušta, M., Ortiz-de-Solórzano, C., & Munoz-Barrutia, A. (2013, April). Registration of multiple stained histological sections. In *Biomedical Imaging (ISBI), 2013 IEEE 10th International Symposium on (pp. 1034-1037)*. IEEE.
- [4] Braumann, U. D., Kuska, J. P., Einkenkel, J., Horn, L. C., Loffler, M., & Hockel, M. (2005). Three-dimensional reconstruction and quantification of cervical carcinoma invasion fronts from histological serial sections. *Medical Imaging, IEEE Transactions on*, 24(10), 1286-1307.
- [5] Collignon, A., Maes, F., Delaere, D., Vandermeulen, D., Suetens, P., & Marchal, G. (1995, June). Automated multi-modality image registration based on information theory. In *Information processing in medical imaging (Vol. 3, No. 6, pp. 263-274)*.
- [6] Cooper, L., Sertel, O., Kong, J., Lozanski, G., Huang, K., & Gurcan, M. (2009). Feature-based registration of histopathology images with different stains: An application for computerized follicular lymphoma prognosis. *Computer methods and programs in biomedicine*, 96(3), 182-192.
- [7] Damas, S., Cerdón, O., & Santamaría, J. (2011). Medical image registration using evolutionary computation: An experimental survey. *IEEE Computational Intelligence Magazine*, 6(4), 26-42.
- [8] De Brabanter, K., Karsmakers, P., Ojeda, F., Alzate, C., De Brabanter, J., Pelckmans, K., ... & Suykens, J. A. (2011). *LS-SVMLab Toolbox User's Guide: version 1.8*. Katholieke Universiteit Leuven.

- [9] Fischler, M. A., & Bolles, R. C. (1981). Random sample consensus: a paradigm for model fitting with applications to image analysis and automated cartography. *Communications of the ACM*, 24(6), 381-395.
- [10] Fitzpatrick, J. M., Hill, D. L., & Maurer Jr, C. R. (2000). Image registration. *Handbook of Medical Imaging*, 2, 447-513.
- [11] Gouveia, A. I. R., Metz, C., Freire, L., & Klein, S. (2012, September). Comparative evaluation of regression methods for 3D-2D image registration. In *International Conference on Artificial Neural Networks* (pp. 238-245). Springer, Berlin, Heidelberg.
- [12] Jiang, J., Trundle, P., & Ren, J. (2010). Medical image analysis with artificial neural networks. *Computerized Medical Imaging and Graphics*, 34(8), 617-631.
- [13] Jorge, A., Gudla, P., Nandy, K., & Lockett, S. J. Solid tumor image registration by hierarchical decomposition assisted automatic landmarks detection.
- [14] Ju, T., Warren, J., Carson, J., Bello, M., Kakadiaris, I., Chiu, W., ... & Eichele, G. (2006). 3D volume reconstruction of a mouse brain from histological sections using warp filtering. *Journal of Neuroscience methods*, 156(1), 84-100.
- [15] Konukoglu, E., Criminisi, A., Pathak, S., Robertson, D., White, S., Haynor, D., & Siddiqui, K. (2011, March). Robust linear registration of CT images using random regression forests. In *Medical Imaging 2011: Image Processing* (Vol. 7962, p. 79621X). International Society for Optics and Photonics.
- [16] Kovesi, P. (2009). *MATLAB and Octave Functions for Computer Vision and Image Processing*. Retrieved on Mar 31, 2013 from <http://www.peterkovesi.com/matlabfns/>
- [17] Kroon, P. (2011). *B-spline Grid, Image and Point based Registration*. Retrieved on Mar 31, 2013 from <https://www.mathworks.com/matlabcentral/fileexchange/20057-b-spline-grid--image-and-point-based-registration>

- [18] Lester, H., & Arridge, S. R. (1999). A survey of hierarchical non-linear medical image registration. *Pattern recognition*, 32(1), 129-149.
- [19] Maes, F., Collignon, A., Vandermeulen, D., Marchal, G., & Suetens, P. (1997). Multimodality image registration by maximization of mutual information. *IEEE transactions on medical imaging*, 16(2), 187-198.
- [20] Magub, S. (2016). *Immunohistochemistry: Getting the Stain You Want*. Retrieved on Jun 4, 2017 from <http://bitesizebio.com/7619/immunohistochemistry-getting-the-stain-you-want/>
- [21] Maintz, J., & Viergever, M. (1998). A survey of medical image registration. *Medical Image Analysis*, 2(1), 1-36.
- [22] Mani, V. R. S., & Arivazhagan, S. (2013). Survey of medical image registration. *Journal of Biomedical Engineering and Technology*, 1(2), 8-25.
- [23] McDonald, J. H. (2014). *Handbook of biological statistics* (3rd ed., pp. 180-185). Baltimore, MD: Sparky House Publishing.
- [24] Morris, R. (2006). *Procrustes Analysis*. Retrieved on July 2, 2017 from https://en.wikipedia.org/wiki/Procrustes_analysis
- [25] Mosaliganti, K., Pan, T., Sharp, R., Ridgway, R., Iyengar, S., Gulacy, A., ... & Saltz, J. (2006, March). Registration and 3d visualization of large microscopy images. In *Proc. of SPIE Vol* (Vol. 6144, pp. 61442V-1).
- [26] Murphy, K. P. (2012). *Machine learning: A probabilistic perspective*. Cambridge, MA: MIT Press.
- [27] Ng., L. (2004) *Overview: ITK Registration Methods*. Retrieved on Feb 12, 2012 from <http://www.itk.org/CourseWare/Training/RegistrationMethodsOverview.pdf>
- [28] Oliveira, F. P., & Tavares, J. M. R. (2014). Medical image registration: a review. *Computer methods in biomechanics and biomedical engineering*, 17(2), 73-93.

- [29] Ourselin, S., Roche, A., Subsol, G., Pennec, X., & Ayache, N. (2000). Reconstructing a 3D structure from serial histological sections. *Image and vision computing*, 19(1), 25-31.
- [30] Peng, D., Liu, J., Tian, J., & Zheng, S. (2006). Transformation model estimation of image registration via least square support vector machines. *Pattern Recognition Letters*, 27(12), 1397-1404.
- [31] Pinoli, J. C. (2014). *Mathematical foundations of image processing and analysis* (Vol. 1). John Wiley & Sons.
- [32] Pitiot, A., & Guimond, A. (2008). Geometrical regularization of displacement fields for histological image registration. *Medical Image Analysis*, 12(1), 16-25.
- [33] Pluim, J. P., Maintz, J. A., & Viergever, M. A. (2003). Mutual-information-based registration of medical images: a survey. *IEEE transactions on medical imaging*, 22(8), 986-1004.
- [34] Pradhan, D., Monaco, S. E., Parwani, A. V., Ahmed, I., Duboy, J., & Pantanowitz, L. (2016). Evaluation of panoramic digital images using Panoptiq for frozen section diagnosis. *Journal of pathology informatics*, 7.
- [35] Prince, S. J. (2012). *Computer vision: models, learning, and inference*. Cambridge University Press.
- [36] Qi, W., Gu, L., & Zhao, Q. (2008, August). Effective 2D-3D medical image registration using Support Vector Machine. In *Engineering in Medicine and Biology Society, 2008. EMBS 2008. 30th Annual International Conference of the IEEE* (pp. 5386-5389). IEEE.
- [37] Russakoff, D. B., Tomasi, C., Rohlfing, T., & Maurer Jr, C. R. (2004, May). Image similarity using mutual information of regions. In *European Conference on Computer Vision* (pp. 596-607). Springer Berlin Heidelberg.
- [38] Santamaría, J., Cordón, O., & Damas, S. (2011). A comparative study of state-of-the-art evolutionary image registration methods for 3D modeling. *Computer Vision and Image Understanding*, 115(9), 1340-1354.

- [39] Smola, A. J., & Schölkopf, B. (2004). A tutorial on support vector regression. *Statistics and computing*, 14(3), 199-222.
- [40] Sotiras, A., Davatzikos, C., & Paragios, N. (2013). Deformable medical image registration: A survey. *IEEE transactions on medical imaging*, 32(7), 1153-1190.
- [41] Studholme, C., Hill, D. L., & Hawkes, D. J. (1999). An overlap invariant entropy measure of 3D medical image alignment. *Pattern recognition*, 32(1), 71-86.
- [42] Tabsombat, S., & Sugino, N. (2013, January). CT/US image registration using LS-SVM. In *Intelligent Systems Modelling & Simulation (ISMS), 2013 4th International Conference on* (pp. 258-263). IEEE.
- [43] Van den Elsen, P. A., Pol, E. J., & Viergever, M. A. (1993). Medical image matching-a review with classification. *IEEE Engineering in Medicine and Biology Magazine*, 12(1), 26-39.
- [44] Viola, P., & Wells III, W. M. (1997). Alignment by maximization of mutual information. *International journal of computer vision*, 24(2), 137-154.
- [45] Wang, H., & Hu, D. (2005, October). Comparison of SVM and LS-SVM for regression. In *Neural Networks and Brain, 2005. ICNN&B'05. International Conference on* (Vol. 1, pp. 279-283). IEEE.
- [46] Zhang, Z., Zhang, S., Zhang, C. X., & Chen, Y. Z. (2006, January). Multi-modality medical image registration using support vector machines. In *Engineering in Medicine and Biology Society, 2005. IEEE-EMBS 2005. 27th Annual International Conference of the* (pp. 6293-6296). IEEE.
- [47] Zitova, B., Flusser, J., & Sroubek, F. (2005). Image registration: a survey and recent advances. In *IEEE ICIP*.

8 APPENDIX

8.1 Process Flow to Create Image

The following list describes the steps to prepare and scan a slide.

- 1) The mouse is taken down, and the tissue is extracted in the necropsy lab.
- 2) The tissue is shipped to the histology lab, where it is embedded in paraffin to form a block.
- 3) Store the block until slicing.
 - a) The elapsed time between neighboring slices in a block may be as long as a couple of years. This aging can influence the stain's reaction with the tissue, which affects the color/intensity of the image.
- 4) Slice a 5 micron thick sample from the block.
 - a) Typically, a sequence is comprised of consecutive slices. However, sometimes a slice is imaged, the next few slices are thrown away, and another slice is imaged.
- 5) Mount the sample on a glass slide.
- 6) Stain the tissue with one or more stains.
- 7) Cap the sample with a glass cover.
- 8) Transport the slides to the microscopy group, which scans the entire slide and stores the resulting image in a repository connected to the laboratory information management system (LIMS).

8.2 Whole Image Identification Numbers

Several candidate data sets were considered for this study. The "MJ_MECA_*" series was selected, because it offered the largest number of serial sections over the most mice. For each animal, five serial sections were generated at 5 micron intervals. The sections were stained in the following order: HE, CD3, CD8, Meca32, GR1. The images are listed by their slide identification numbers.

Table 32: Slide identification numbers for each image in the MJ_MECA_* series. Each slide created in a given year is assigned a unique alphanumeric code, so they can be retrieved from the slide archive.

HE	CD3	CD8	MECA	GRI	Mouse
140A-PL13	18UD-PL13	18VA-PL13	18W6-PL13	18X1-PL13	16274
140J-PL13	18UM-PL13	18VJ-PL13	18WF-PL13	18XA-PL13	18136
140K-PL13	18UN-PL13	18VK-PL13	18WG-PL13	18XB-PL13	18138
140L-PL13	18UO-PL13	18VL-PL13	18WH-PL13	18XC-PL13	18139
140M-PL13	18UP-PL13	18VM-PL13	18WI-PL13	18XD-PL13	18089
140N-PL13	18UQ-PL13	18VN-PL13	18WJ-PL13	18XE-PL13	18092
140O-PL13	18UR-PL13	18VO-PL13	18WK-PL13	18XF-PL13	18099
140P-PL13	18US-PL13	18VP-PL13	18WL-PL13	18XG-PL13	18110
140Q-PL13	18UT-PL13	18VQ-PL13	18WM-PL13	18XH-PL13	18209
140R-PL13	18UU-PL13	18VR-PL13	18WN-PL13	18XI-PL13	18224
140S-PL13	18UV-PL13	18VS-PL13	18WO-PL13	18XJ-PL13	18235
140B-PL13	18UE-PL13	18VB-PL13	18W7-PL13	18X2-PL13	16970
140T-PL13	18UW-PL13	18VT-PL13	18WP-PL13	18XK-PL13	18237
140U-PL13	18UX-PL13	18VU-PL13	18WQ-PL13	18XL-PL13	18122
140V-PL13	18UY-PL13	18VV-PL13	18WR-PL13	18XM-PL13	18124
140W-PL13	18UZ-PL13	18VW-PL13	18WS-PL13	18XN-PL13	18194
140X-PL13	18V0-PL13	18VX-PL13	18WT-PL13	18XO-PL13	18216
140Y-PL13	18V1-PL13	18VY-PL13	18WU-PL13	18XP-PL13	18147
140Z-PL13	18V2-PL13	18VZ-PL13	18WV-PL13	18XQ-PL13	18163
1410-PL13	18V3-PL13	18W0-PL13	18WW-PL13	18XR-PL13	18164
140C-PL13	18UF-PL13	18VC-PL13	18W8-PL13	18X3-PL13	16971
140D-PL13	18UG-PL13	18VD-PL13	18W9-PL13	18X4-PL13	16973
140E-PL13	18UH-PL13	18VE-PL13	18WA-PL13	18X5-PL13	18113
140F-PL13	18UI-PL13	18VF-PL13	18WB-PL13	18X6-PL13	18114
140G-PL13	18UJ-PL13	18VG-PL13	18WC-PL13	18X7-PL13	16440
140H-PL13	18UK-PL13	18VH-PL13	18WD-PL13	18X8-PL13	16932
140I-PL13	18UL-PL13	18VI-PL13	18WE-PL13	18X9-PL13	18134

8.3 Sub-Image Identification Numbers

Each sub-image in the dataset for this study can be uniquely identified by a combination of slide identification number concatenated with a sub-image number.

Table 33: Number of sub-images per image pair.

MECA	GRI	Number of Sub-images	MECA	GRI	Number of Sub-images
18W6-PL13	18X1-PL13	1	18WR-PL13	18XM-PL13	2
18WF-PL13	18XA-PL13	1	18WT-PL13	18XO-PL13	1
18WG-PL13	18XB-PL13	1	18WU-PL13	18XP-PL13	1
18WH-PL13	18XC-PL13	1	18WV-PL13	18XQ-PL13	1
18WI-PL13	18XD-PL13	1	18WV-PL13	18XQ-PL13	2
18WJ-PL13	18XE-PL13	1	18WW-PL13	18XR-PL13	1
18WL-PL13	18XG-PL13	1	18W8-PL13	18X3-PL13	1
18WL-PL13	18XG-PL13	2	18W9-PL13	18X4-PL13	1
18WM-PL13	18XH-PL13	1	18W9-PL13	18X4-PL13	2
18WN-PL13	18XI-PL13	1	18WA-PL13	18X5-PL13	1
18WN-PL13	18XI-PL13	2	18WA-PL13	18X5-PL13	2
18WO-PL13	18XJ-PL13	1	18WB-PL13	18X6-PL13	1
18W7-PL13	18X2-PL13	1	18WC-PL13	18X7-PL13	1
18WP-PL13	18XK-PL13	1	18WD-PL13	18X8-PL13	1
18WQ-PL13	18XL-PL13	1	18WD-PL13	18X8-PL13	2
18WQ-PL13	18XL-PL13	2	18WE-PL13	18X9-PL13	1
18WQ-PL13	18XL-PL13	3	18WE-PL13	18X9-PL13	2
18WR-PL13	18XM-PL13	1	18WE-PL13	18X9-PL13	3

8.4 Sub-Image Masking Algorithm

Matlab code for isolating the largest piece tissue in a sub-image.

```
% find subregion with largest area
sep_mask = im2bw(t_im, tlevel);
sep_mask = bwareaopen(sep_mask, 10000);
sep_mask = imdilate(sep_mask, d9);
sep_mask = bwmorph(sep_mask, 'skel', 30);
sep_mask = bwmorph(sep_mask, 'diag');

ss_mask3 = ss_mask3 & ~sep_mask;

%ss_mask controls loading of subregions of tissue
ss_out_im = bwlabel(ss_mask3);
stats = regionprops(ss_out_im, 'Area');

[maxArea, regionnum] = max([stats.Area]);
regionmask = (ss_out_im == regionnum);
ss_mask3 = im2bw(ss_out_im.*(double(regionmask)));
ss_mask3 = imclose(ss_mask3, d3);           % fix seams from sep_mask
```

8.5 Tissue Segmentation Algorithm

Matlab code for segmenting tissue from the background.

```
%% create mask for BLANK image
tlevel = (b_im_thresh /255);
tempmont_mask = ~im2bw(b_im, tlevel);

% density filter to remove non-tumor areas
ss_mask3 = tempmont_mask;
ss_mask3 = imopen(ss_mask3, d2);
ss_mask3 = imclose(ss_mask3, d3);

ss_mask3 = imclose(ss_mask3, d9);
ss_mask3 = imopen(ss_mask3, d9);

ss_mask3 = ~(bwareaopen(~ss_mask3, 1000)); % closes small holes in tissue
ss_mask3 = bwareaopen(ss_mask3, 1000); % removes small pieces of tissue

ss_mask3 = ~(bwareaopen(~ss_mask3, 20000)); % closes small holes in tissue
```